AN ABSTRACT OF THE THESIS OF

Jeanette M. Roberts for the degree of Doctor of Philosophy in Physics
presented on April 13, 1995. Title: Critical Scaling of Thin-film YBaCuO and NdCeCuO Resistivity-current Isotherms: Implications for Vortex Phase Transitions and Universality.

Redacted for Privacy

Abstract approved: _____

Janet Tate

In contrast to conventional theories of vortex motion, it was recently proposed that there does exist a truly superconducting mixed state called the vortex glass phase. This model predicts that a superconductor with point defects will undergo a phase transition from a vortex liquid to a vortex glass at a temperature T_g. This transition is expected to be second-order, and as a consequence critical scaling applies; the resistivity-current isotherms should scale with universal critical exponents and scaling functions. Several experiments have supported this picture.

This thesis is the investigation of the vortex glass model at magnetic fields lower than those previously reported, and is the first consistent comparison of $YBa_2Cu_3O_{7-\delta}$ and $Nd_{1.85}Ce_{0.15}CuO_{4-y}$ thin films. DC resistivity-current isotherms for both superconductors were measured and scaled. The high-field data for both films are the same and are consistent with the vortex glass model. However, the critical exponents and universal functions change as the field is decreased, indicating a fundamental change in the transition.

Critical Scaling of Thin-film YBaCuO and NdCeCuO Resistivity-current Isotherms: Implications for Vortex Phase Transitions and Universality

by

Jeanette M. Roberts

A THESIS

submitted to

Oregon State University

in partial fulfillment of
the requirements for the
degree of
Doctor of Philosophy

Completed April 13, 1995
Commencement June 1995

Doctor of Philosophy thesis of Jeanette M. Roberts presented on April 13, 1995

APPROVED:

Redacted for Privacy

Major Professor, representing Physics

Redacted for Privacy

Chair of Department of Physics

Redacted for Privacy

Dean of Graduate School

I understand that my thesis will become part of the permanent collection of Oregon State University libraries. My signature below authorizes release of my thesis to any reader upon request.

Redacted for Privacy

Jeanette M. Roberts, Author

ACKNOWLEDGMENTS

Dr. Janet Tate for supporting my pursuit of the anomalous low-field data. I am lucky to have Janet as an advisor; I have learned a lot from her, and value her friendship. I thank Janet for placing trust and confidence in me.

The most difficult person to thank is my friend and colleague Brandon Brown. I wouldn't know where to begin or stop the list of things for which I am indebted. I must certainly mention that much of the data in this thesis was acquired and analyzed by Brandon. More important is his contribution to the perfection of the scaling analysis technique, his dedication to the project on all days and at all hours, and his part in writing the PRB articles. And, of course, the contacts.

Dennis Tom for his help in taking data and evaporating contacts (even on Superbowl Sunday), for being the best local computer expert (including saving our hard disk memory), as well as making the lab a more fun place to work. Not to mention the drawing.

Joel Dille for contributing fresh enthusiasm to the thin-film evaporation project.

Goran Karapetrov for his lab expertise and always having an interesting paper on hand.

Dr. Allen Wasserman for being an inspirational instructor, and making the halls of Weniger a more friendly place to be.

Dr. Bill Warren for taking an active role in my studies including providing helpful comments on my thesis, critiquing my presentation skills, and advising me about resume writing.

Dr. Corinne Manogue for her support, frank advice, and ready smile.

Dr. Dave Griffiths and Dr. Dave McIntyre for being last minute committee members.

Bianca Hermann for laying much of the foundation on which this project stood.

Lisa Dundon for her unwavering friendship, and making my first year in grad school more pleasant than Hades.

Nick and Nettie for making my days interesting and fun, and for accepting when I had to work long, unusual hours.

Hank for his assistance and support.

I express my gratitude to and admiration of Grace Warren.

TABLE OF CONTENTS

TABLE OF CONTENTS (CONTINUED)

LIST OF FIGURES

LIST OF FIGURES (CONTINUED)

LIST OF TABLES

GLOSSARY OF TERMS, ACRONYMS AND SYMBOLS

a_o intervortex spacing, $a_o = \sqrt{\frac{\Phi_o}{B}}$; § 1.1

BG Bose glass; § 1.6, 1.7

c_{ii} elastic moduli; c_{11} is the bulk, c_{44} is the tilt, and c_{66} is the shear; § 2.7

CC collective creep; § 2.7

dynamic disorder disorder owing to thermal (or quantum) fluctuations; § 1.5

$F_{\pm}$ universal functions; § 2.1, 2.3, 3.7

FF flux flow; § 1.4, 3.7

FFH Fisher, Fisher and Huse (1991); the canonical paper describing the vortex glass theory

flux quantum $\Phi_o = \frac{h}{2e} = 2.07 \times 10^{-15}\ \mathrm{T \cdot m^2}$; § 1.1

γ the anisotropy, $\gamma \equiv \left(\frac{M_z}{m_{ab}}\right)^{1/2} = \frac{\xi_{ab}}{\xi_z} = \frac{\lambda_z}{\lambda_{ab}}$; § 1.2, 1.5

G_i Ginzburg number; § 1.5

Ginzburg-Landau regime mean-field regime

H_c thermodynamic critical field; § 1.1

H_{c1} lower critical field; § 1.1

H_{c2} upper critical field, $H_{c2} = \frac{\phi_o}{2\pi\xi^2}$; § 1.1

HTS high transition temperature superconductors; § 1.2

J_c critical current; § 1.4

GLOSSARY OF TERMS, ACRONYMS AND SYMBOLS (CONTINUED)

J_{sc} scaled current density, $J_{sc} = \frac{J}{J_o T}\left|1-\frac{T}{T_g}\right|^{-2\nu}$; § 3.7

κ Ginzburg-Landau parameter, $\kappa = \frac{\lambda}{\xi}$; § 1.1

l interlayer spacing

L_c distance over which vortex positions are correlated in the longitudinal ($\|B$) direction; § 1.4, 2.7

λ penetration depth; distance which the magnetic field penetrates a superconductor; § 1.1

Larkin-Ovchinnikov lengths L_c and R_c; describe positional correlations; § 2.7

Lindemann criterion $\langle u \rangle^{\frac{1}{2}} \approx ca$, $c \approx 0.1-0.3$; used to estimate the vortex melting temperature; § 1.5

LTS low transition temperature superconductors; § 1.1

ν static critical exponent; § 2.1, 2.2

non-activated phase slip dissipation which is not thermally activated

non-activated vortex motion vortex motion which is not thermally activated (such as in the flux flow regime)

ODLRO off-diagonal long-range order; correlation in the phase ϕ of the superconducting order parameter $\Psi = |\Psi| e^{i\phi}$

order parameter in superconductors, the wave function, $\Psi = |\Psi| e^{i\phi}$, with a magnitude $|\Psi|$ and phase ϕ; § 1.1

phase slip dissipation

quenched disorder static disorder; disorder owing to impurities; § 1.4

GLOSSARY OF TERMS, ACRONYMS AND SYMBOLS (CONTINUED)

ρ_{FF} flux-flow resistivity; § 1.4

ρ_{SC} scaled resistivity, $\rho_{SC} = \frac{\rho}{\rho_o}\left|1-\frac{T}{T_g}\right|^{\nu(z-1)}$; § 3.7

ρ_{TAFF} TAFF (thermally assisted flux-flow) resistivity; § 1.4

R_c The distance over which vortex positions are correlated in the transverse ($\perp B$) direction; § 1.4, 2.7

static disorder disorder owing to impurities; § 1.4

T_c superconducting transition temperature; in this thesis defined as the temperature at which either (a) ρ is half the normal state value, or (b) $\rho < 10^{-3}$ μΩcm

T_g vortex glass transition temperature

TAFF thermally assisted flux flow; § 1.4

U_0 pinning potential; § 1.4

u vortex displacements; § 1.5, 2.7

V_c correlation volume; volume in which the positions of vortices are correlated; § 2.7

VG vortex glass

ξ coherence length; the radius of the vortex core; § 1.1

ξ correlation length in critical scaling theory; § 2.2

ξ_{VG} vortex glass correlation length

z dynamic critical exponent; § 2.1, 2.2

CHAPTER 1
INTRODUCTION

Magnetic vortices (quantized bundles of magnetic flux) are peculiar to type-II superconductors and offer novel, interesting phenomena to be explored. The mechanisms that govern vortex movement are not completely understood, which is technologically important because moving vortices destroy superconductivity. Here, true superconductivity is defined by the vanishing of ohmic resistivity. In applications it would be beneficial if superconductors were truly superconducting, at least in the limit of zero applied current. Conventional theory for vortex motion predicts that a type-II superconductor, in a penetrating magnetic field, will always have some resistance; the resistance may fall below the detection limit, but will never be zero. This model of flux creep (§ 1.4) was able to explain the behavior of low transition temperature type-II superconductors (LTS). However, this model does not explain the experimental resistivity-current density ($\rho - J$) data of high temperature superconductors (HTS). A further quandary concerning the magnetic behavior of these materials results from the existence of an irreversibility line (IL) in the magnetic field-temperature ($H - T$) phase diagram. Below this line (low T) the magnetization is irreversible; the zero field cooled and field cooled magnetizations are different. Above the IL, the magnetization is reversible. The more recent theories of vortex glass and collective creep attempt to describe the vortex system and the $\rho - J$ data of HTS.

1.1 Superconductivity

Superconductivity has been defined using several criteria, including the behavior of a material in a magnetic field and the vanishing of resistance at a transition temperature T_c. A powerful phenomenological description of superconductors was presented by Ginzburg and Landau (GL) in 1950. This model assumes that a superconductor can be described by a complex order parameter $\Psi = |\Psi| e^{i\phi}$. The free energy is expanded in a power series of ψ, and the values of the coefficients of expansion can be limited based on physical principles.

A microscopic theory of superconductivity was presented in 1957 by Bardeen, Cooper, and Schrieffer (Tinkham, 1975). The BCS theory assumes that superconductivity arises owing to interactions between electrons and phonons. (A phonon is the quantum of an elastic wave in a solid.) Because of the electron-phonon interaction, electrons feel a positive attraction and become bound in pairs (Cooper pairs) which travel through the material without dissipation. In 1959 Gor'kov showed that the GL theory is a limiting case of the BCS theory; the order parameter ψ is the wavefunction of the of the center-of-mass motion of the Cooper pairs. Therefore, a superconductor can be defined by the existence of a many-particle condensate wavefunction $\Psi = |\Psi| e^{i\phi}$ which has phase coherence over macroscopic distances (Tinkham, 1975).

Superconductors can be divided into two classes based on the relative sizes of two material-dependent lengths. The penetration depth λ and the coherence length ξ quantify the spatial variation of the magnetic field and

the wave function respectively. The ratio of these lengths is called the Ginzburg-Landau parameter $\kappa = \frac{\lambda}{\xi}$. A superconductor is type-I if $\kappa < \frac{1}{\sqrt{2}}$ and type-II if $\kappa > \frac{1}{\sqrt{2}}$. Type-I superconductors are in the Meissner state when the applied field is less than the thermodynamic critical field H_c; the field is expelled by the superconductor, which is accomplished by having supercurrents (currents consisting of superelectrons, ones bound in Cooper pairs) flow within λ of the surface. These supercurrents create a field which exactly cancels the applied field, resulting in a net field of zero inside the sample. Type-I superconductors are normal (not superconducting) in fields greater than H_c.

Abrikosov (1957) showed that defect-free, type-II superconductors have two superconducting phases. The Meissner phase occurs when the applied magnetic field is less than the lower critical field H_{c1}, as it does in type-I superconductors. However, at H_{c1} the magnetic field enters the sample in quantized bundles of magnetic flux called vortices, (or vortex lines, flux lines, flux tubes, fluxons, or fluxoids). Each vortex contains one quantum of magnetic flux $\Phi_o = \frac{h}{2e} = 2.07 \times 10^{-15}\ \mathrm{T \cdot m^2}$, where h= Planck's constant and e is the charge of an electron. The vortex lines are essentially parallel to the applied field, and (in a simple model) consist of a normal core surrounded by circling supercurrents, as depicted in Fig. 1.1.

The whirlpool-like vortex nature of these currents gives vortices their name. The magnitude $|\Psi|$ of the superconducting order parameter $\Psi = |\Psi| e^{i\phi}$ is zero at the center of the vortex core, and the phase ϕ changes by 2π upon circling a vortex. The radius of the vortex core (which is normal) is $\sim \xi$; $|\Psi|$ is

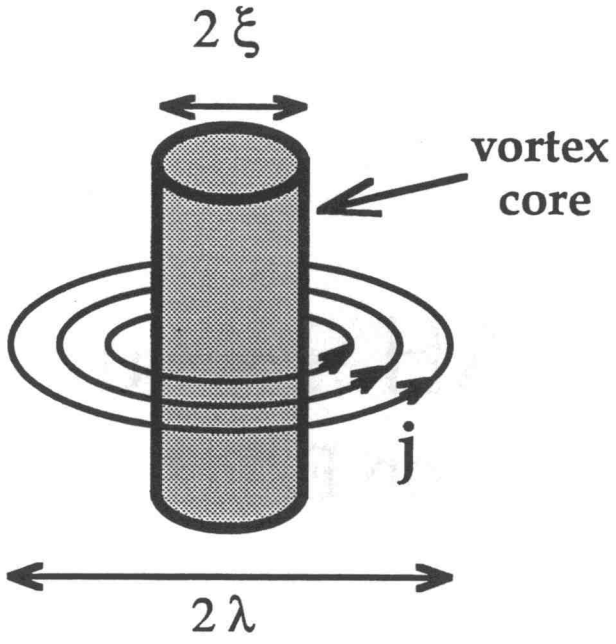

Figure 1.1. Schematic representation of a vortex. The order parameter is significantly suppressed in the vortex core which has a radius of ~ξ, the coherence length. Supercurrents flow around the core out to a radius of ~λ, the penetration depth.

significantly suppressed over a distance of about 2ξ. The magnetic field extends from the center of the core $\sim\lambda$; vortex currents occur out to about 2λ. The whirling current around each vortex creates a magnetic field, which shields the bulk of the superconductor from the field entering the vortex core. Abrikosov showed that, in this mixed state, vortices arrange themselves in a regular triangular pattern called the vortex lattice. The average intervortex spacing is denoted by a_o, which can be estimated as follows.

The number N of vortices penetrating an area A is

$$N = \frac{\text{total flux through } A}{\text{flux per vortex}} = \frac{BA}{\phi_o} \qquad 1.1$$

where B is the applied field. For a square lattice of vortices, a unit cell contains $\frac{1}{4}4=1$ vortex, and has an area $A=a_o^2$. Therefore, $1=\frac{Ba_o}{\phi_o}$ or, $a_o=\sqrt{\frac{\Phi_o}{B}}$ [for a triangular lattice the exact result is $a_o=1.075\sqrt{\frac{\Phi_o}{B}}$ (Tinkham, 1975)]; as the field is decreased, a_o increases.

At a high field $B=H_{c2}$ vortices become closer than 2ξ ($a_o=2\xi$), causing their cores to overlap and destroying superconductivity since the current can no longer find a superconducting path. The field at which this occurs is called the upper critical field and is given by (Clem, 1990)

$$H_{c2}=\frac{\phi_o}{2\pi\xi_{ab}^2}, \qquad 1.2$$

(which differs by a factor of $\frac{1}{2\pi}$ from the result one would obtain by combining the above equations, owing to oversimplifications in the preceding argument).

1.2 High Transition Temperature Superconductors

High-T_c superconductors (HTS) differ from conventional low-T_c superconductors (LTS) in several ways. They generally have much higher transition temperatures (T_c~20-134 K) than LTS (T_c<20 K). HTS are extreme type-II, with large Ginzburg-Landau parameters (κ~100). They are copper-oxides with a perovskite crystal structure, as shown in Fig. 1.2 for $Nd_{1.85}Ce_{0.15}CuO_{4-y}$ and $YBa_2Cu_3O_{7-\delta}$. Superconductivity occurs in the Cu-O planes which makes these materials highly anisotropic. The in-plane (in the ab plane) coherence length and penetration depth are ξ_{ab} and λ_{ab},

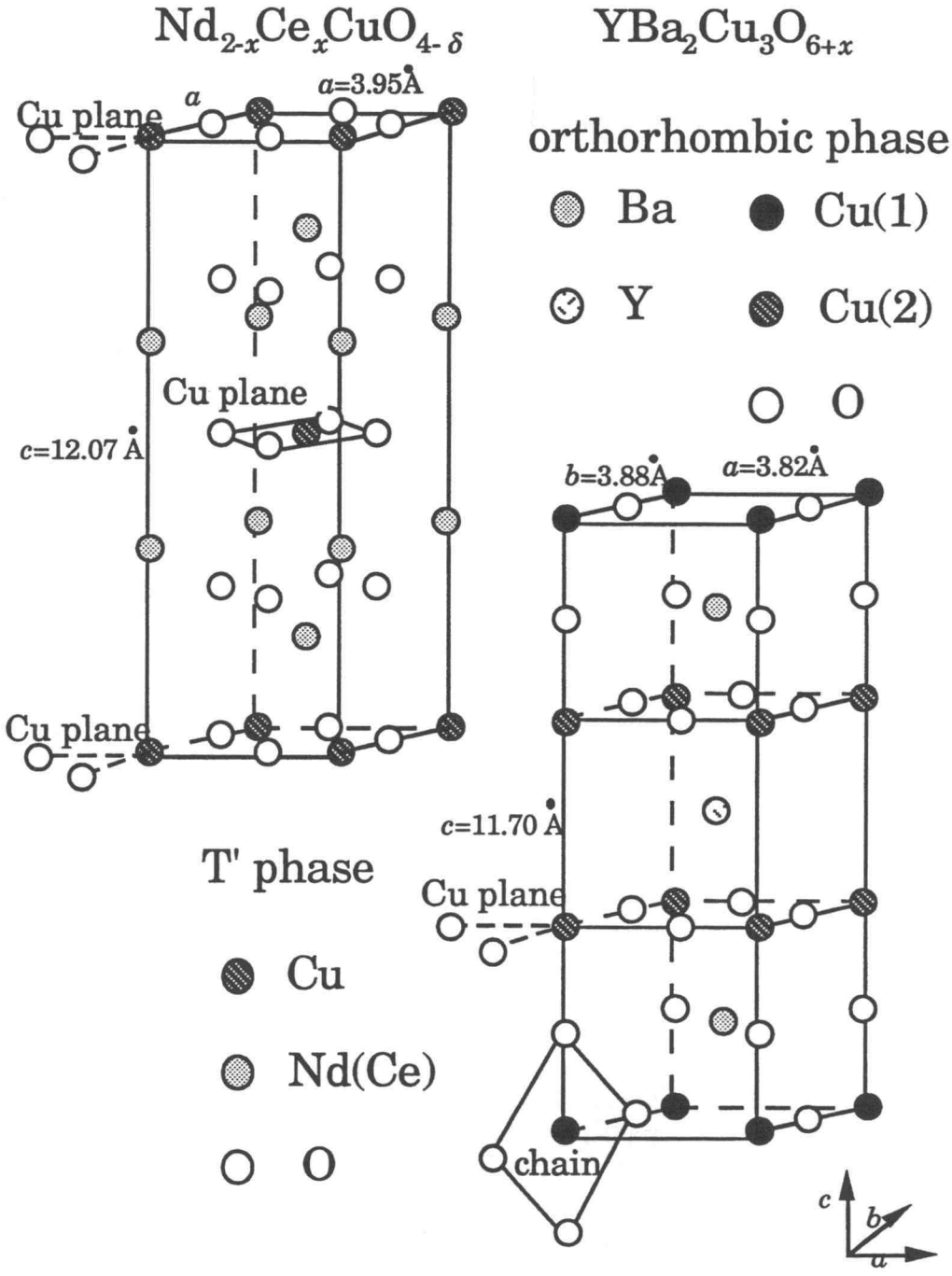

Figure 1.2 Crystal structure of NdCeCuO and YBaCuO.

respectively. Similarly, the out-of-plane (along the c direction) values are denoted ξ_z and λ_z. The anisotropy γ is $\gamma \equiv \left(\frac{M_z}{m_{ab}}\right)^{1/2} = \frac{\xi_{ab}}{\xi_z} = \frac{\lambda_z}{\lambda_{ab}}$ where m_{ab} and M_z are the effective mass in the ab and c directions, respectively. Table 1.1 lists some values of these parameters.

1.3 Dissipation in Superconductors

A primary source of dissipation (resistance) in superconductors is the movement of vortices, because moving vortices create an electric field $\mathbf{E}$ according to $\mathbf{E} \propto \mathbf{B} \times \mathbf{v}$. If there is an electric field and current is flowing, then there is resistivity ρ since $\mathbf{J} = \frac{1}{\rho}\mathbf{E}$. One impetus for vortex movement is the presence of an applied current (which is necessary in most applications of superconductors) since current causes a Lorentz force density $\mathbf{J} \times \mathbf{B}$ to be exerted on the flux lines. Thus, in a defect-free superconductor, the vortex lattice phase is not a truly superconducting state. The experimental observation however, is that the resistance does vanish at some temperature. This is due to vortices becoming pinned by imperfections in the superconductor.

1.4 Pinning and Flux Creep

If a superconductor has imperfections (such as vacancies, impurities, interstitials, twin boundaries, etc.) vortices tend to get pinned at the defects, which both impedes their movement and disrupts the uniform lattice arrangement; Larkin and Ovchinnikov (1979) showed that, in the presence of static (quenched) disorder, there is no long-range correlation of vortex

positions (even for weak pinning), beyond the Larkin-Ovchinnikov correlation length (R_c). On length scales shorter than this, the vortices are arranged in a lattice, but regular lattice structure is destroyed on longer length scales. The flux-creep model [pioneered by Anderson and Kim (Anderson, 1962; Anderson and Kim, 1964)] considered the problem of a single vortex (or a bundle of size R_c) moving independently in a random pinning potential. The vortex bundles jump over potential barriers, of height U_0, via thermal activation; the solution to this problem gives a resistivity

$$\rho(J, T) = 2\frac{J_c}{J}\rho_c \exp(-\frac{U_o}{k_B T})\sinh\left(\frac{J}{J_c}\frac{U_o}{k_B T}\right) \qquad 1.3$$

where $J_c(B)$ is the critical current density at $T = 0$ and $\rho_c(B, T)$ is the resistivity at $J = J_c$ (Brandt, 1993).

At a large current J_c (the critical current or depinning current) the Lorentz force becomes much greater than the pinning force. When this occurs, the vortices are not impeded by the pinning potential and vortex movement is slowed only by a viscous drag force; this is known as flux-flow (FF). The constant FF resistivity in this regime

$$\rho(J) = \rho_{FF} \qquad 1.4$$

may be obtained from Eq. 1.3, for the limit of $J >> J_c$, or from models such as the one developed by Bardeen and Stephen (Bardeen and Stephen, 1965; Tinkham, 1975).

The resistivity in Eq. 1.3 is not zero, even in the limit of zero applied current; to see this, consider $J << J_c$, then $\frac{J}{J_c}\frac{U_o}{k_B T}$ is small and

$\sinh\left(\frac{J}{J_c}\frac{U_o}{k_BT}\right) \approx \frac{J}{J_c}\frac{U_o}{k_BT}$. In this regime, called thermally assisted flux flow (TAFF), Eq. 1.3 becomes

$$\rho(J) = 2\rho_c \frac{U_o}{k_BT}\exp(-\frac{U_o}{k_BT}) = \rho_{TAFF} \qquad 1.5$$

which is a constant for constant T. The point is moot for low-T_C superconductors because $\frac{U_0}{k_BT}$~100 so ρ_{TAFF} becomes too small to measure. However, in high-T_C superconductors, $\frac{U_o}{k_BT}$~10 (Kes *et al.*, 1989).

In the intermediate current regime, $(J \approx J_c)$, and if $U_o >> k_BT$, then a current dependent resistivity is expected from Eq. 1.3. To obtain this result, the sinh function is expanded (recall $2\sinh x = e^x - e^{-x}$) yielding

$$\rho(J, T) = \rho_c \frac{J_c}{J}\left\{\exp\left[\frac{U_o}{k_BT}\left(\frac{J}{J_c}-1\right)\right] - \exp\left[-\frac{U_o}{k_BT}\left(\frac{J}{J_c}+1\right)\right]\right\}. \qquad 1.6$$

If $U_o >> k_BT$ and $J \approx J_c$, then the second exponential approaches zero, and Eq. 1.6 becomes

$$\rho(J, T) = \rho_c \frac{J_c}{J}\exp\left[-\frac{U_o}{k_BT}\left(1-\frac{J}{J_c}\right)\right]. \qquad 1.7$$

This can be generalized to

$$\rho(J, T) = \rho_c \frac{J_c}{J}\exp\left[-\frac{U(J)}{k_BT}\right] \qquad 1.8$$

where the function $U(J)$ depends on the model of dissipation; the Anderson-Kim model is then a specific case of Eq. 1.8 with

$$U(J) = U_o\left(1 - \frac{J}{J_c}\right). \qquad 1.9$$

With no applied current, the activation energy $U(J)$ is just the pinning energy U_o, which is the same form as the result obtained in Eq. 1.5.

1.5 Thermal Disorder

In addition to the static disorder introduced by impurities, HTS are also subject to dynamic disorder owing to thermal fluctuations. [It has been suggested (Brandt, 1993) that quantum fluctuations may be the primary source of dynamic disorder in YBCO above ~4T.] Thermal fluctuations are more important in HTS than LTS because of the higher T_c, shorter ξ (vortices form at higher fields, since $H_{c2} = \frac{\phi_o}{2\pi\xi_{ab}^2}$), larger γ (reducing the interaction between vortices in different planes), and longer λ, than found in LTS; typical values for these parameters appear in Table 1.1.

The importance of thermal fluctuations are quantified by the Ginzburg number G_i (Blatter *et al.*, 1994)

$$G_i \sim \left(\frac{T_c k_B}{H_c^2 \gamma \xi_{ab}^3}\right)^2 \qquad 1.10$$

where $T_c k_B$ is the thermal energy, $H_c = \frac{H_{c2}}{\kappa\sqrt{2}}$ is the thermodynamic critical field (Tinkham, 1975), $\gamma \equiv \left(\frac{M_z}{m_\perp}\right)^{1/2} = \frac{\xi_{ab}}{\xi_z} = \frac{\lambda_z}{\lambda_{ab}}$ is the anisotropy, and $\kappa = \frac{\lambda}{\xi}$ is the Ginzburg-Landau parameter. The Ginzburg number is about 10^{-2} in YBCO, 10^{-4} in NCCO, and 10^{-12} in LTS. This makes it possible to see the effects of thermal fluctuations in HTS.

Thermal fluctuations cause vortices to move about (much like molecules in a fluid) resulting in a finite linear resistance. In this vortex liquid state there is no long-range correlation of the vortex positions, although there are short-range correlations. Instead of a true phase transition, H_{c2} marks a smooth crossover from the normal state to the vortex liquid state. This crossover region is dominated by thermal fluctuations, and has a width given approximately by $\tau_T \approx T_c G_i$ in a weak field; the width varies with field as (Blatter *et al.*, 1994)

Table 1.1. Material characteristics of YBCO and NCCO.

	LTS	YBCO	NCCO
$\lambda(0)$ (nm)	~10	140[φ]	130[ν]
$\xi_{ab}(0)$ (nm)	~10[α]	1-1.5[ε, μ]	7-8[δ, ι, ν]
H_{c2} (T) $H\|\|c$		100[ε, μ]	2.7[η]
γ	1	5-7[ε]	20-25[ι, κ]
G_i	10^{-12}[β]	10^{-2}[β]	10^{-4}

[β]Blatter, *et al.*, 1994
[α]Brandt, 1993
[δ]Dalichaouch *et al.*, 1990
[ε]Dolan *et al.*, 1989
[η]Hermann, 1992
[ι]Hidaka and Szuki, 1989
[φ]Mao *et al.*, 1995.
[κ]O and Markert, 1993
[μ]Welp *et al.*, 1989
[ν]Wu *et al.*, 1993

$$\tau_T \approx T_c G_i^{1/3} \left[\frac{H_{c2}(T)}{H_{c2}(0)} \right]^{\frac{2}{3}} \qquad 1.11$$

In systems with little disorder (such as untwinned single crystals) a vortex lattice may, at some temperature, melt into a vortex liquid; this is generally expected to be a first order transition. The melting temperature (in the absence of pinning) is often estimated using the Lindemann criterion (Lindemann, 1910). In this approximation the lattice is assumed to melt when the size of the vortex displacements u becomes comparable to the intervortex spacing,

$$\left\langle u^2 \right\rangle^{\frac{1}{2}} \approx c a_0. \qquad 1.12$$

where c is the Lindemann number. For conventional liquids c=0.1–0.2; Monte Carlo simulations for the melting of a model vortex lattice found c=0.2–0.3 (Ryu *et al.*, 1992). It is expected that the width of the melting region τ_m differs from τ_T by a numerical factor (Feigel'man *et al.*, 1993),

$$\frac{\tau_m}{\tau_T} \approx 3\text{–}7 \qquad 1.13$$

Apparently, Feigel'man *et al.* assume that the melting transition is second order.

1.6 Vortex Glass, Bose Glass and Collective Creep

More recent theories for flux motion in HTS (for $J < J_c$) consider vortices in superconductors as objects which have length, in contrast to the flux creep model. One theory, collective creep (Feigel'man, *et al.*, 1989; Natterman, 1990; Fischer and Natterman, 1991) approaches the problem by considering vortices

as elastic objects. Another theory is the vortex glass (VG) model of Fisher, Fisher, and Huse (FFH) (Fisher, Fisher, and Huse, 1991; Fisher, 1989; Huse, Fisher and Fisher, 1992). (For review articles on the vortex glass theory, see Bishop, Gammel, and Huse, 1993; Bishop, 1992; Fisher, 1993; Blatter *et al.*, 1994.) FFH suggest that the low temperature state is a different phase of vortex matter, and that there should exist a second-order phase transition between the vortex liquid state and the vortex glass state. Both models predict the same functional form for the low-temperature $\rho - J$ isotherms,

$$\rho \propto \exp\left[-\left(\frac{J_o}{J}\right)^{\mu}\right] \qquad 1.14$$

but have different predictions for the value of μ (see § 2.6 and 2.7).

Another model which proposes a vortex phase transition was presented by Nelson, and Vinokur (Nelson and Vinokur, 1992; Hwa, Nelson and Vinokur, 1993), who considered superconductors with line defects (such as weak-link grain boundaries), in contrast to point defects (such as vacancies, interstitials, or microscopic grain boundaries), and predicted that such a system will undergo a phase transition from a liquid state to a Bose glass (BG) state. Although it is not certain whether the BG and VG transitions belong to different universality classes, the two models have different predictions for the angular dependence of the transition temperature.

One way to distinguish between a true phase transition (with time and length scales which diverge at criticality) and a gradual slowing down with long-range (but finite) correlations, is to search for evidence of a phase

transition via the critical scaling of $\rho - J$ isotherms. A phase transition would be characterized by universal static τ and dynamic z critical exponents.

1.7 Experimental Evidence for a Vortex Glass Phase Transition

The first experimental evidence lending support to the VG idea was obtained by Koch *et al.* (1989), who performed a critical scaling analysis of the $\rho - J$ characteristics of $YBa_2Cu_3O_{7-\delta}$ (YBCO) thin films. This was followed by experiments on both ceramic (Worthington *et al.*, 1991) and single crystal (Gammel, Schneemeyer, and Bishop, 1991) YBCO. Similar experiments have been performed using $Bi_2Sr_2Ca_1Cu_2O_{8+\delta}$ (Bi2212) (Safar *et al.*, 1992), $Bi_2Sr_2Ca_2Cu_3O_{10}$ (Bi2223) (Li *et al.*, 1994; Yamasaki *et al.*, 1994), $Nd_{1.85}Ce_{0.15}CuO_{4-y}$ (NCCO) films (Yeh *et al.*, 1992), and amorphous Mo_3Si films (Yeh *et al.*, 1993a). Gammel, Schneemeyer, and Bishop (1991) lowered the measured voltage regime by several orders of magnitude using a SQUID picovoltmeter; they observed no deviation from the behavior predicted by Eq. 1.14 (even at the lowest voltages) for isotherms below the transition. Olsson *et al.* (1991) studied the ac response of the resistivity in the region above T_g and found that the data are consistent with the VG model. Size effects were examined in YBCO films by Dekker *et al.* (1992) and by Ando, Kubota, and Tanaka (1992). Dekker *et al.* analyzed the effects of decreasing film thickness and found confirming evidence that the lower critical dimension d_l of the vortex glass transitions lies between 2 and 3, as predicted by FFH. Ando, Kubota, and Tanaka examined the effect of having very narrow bridges.

To investigate the possible existence of a Bose glass transition, angle-resolved studies have been performed on YBCO thin films by Wöltgens *et al.* (1993) and by Silver, de Lozanne, and Thompson (1993). Wöltgens *et al.* confirm the existence of a vortex glass transition in YBCO, but not the Bose glass transition. However, Silver, de Lozanne, and Thompson found evidence for a BG state when the magnetic field is applied nearly parallel to the *c*-axis of the film, but a VG state for fields applied at angles greater than a critical angle.

Several unsettled issues remain concerning the existence and the nature of the purported vortex phase transition. Most notable is whether the observed scaling relation is indicative of a true phase transition, or is merely a convenient parameterization. If a phase transition occurs, then one expects universal critical exponents and scaling functions. Universality seems to be established in YBCO films at high magnetic fields; the exponents converge to $z \sim 5.7$, $\nu \sim 1.7$ (as demonstrated in Table 1.2), which is consistent with the predictions of the vortex glass model. The exponents for YBCO single crystals seem to be different from those of films ($z \sim 3.5$, $1 < \nu < 3$). This may signal that crystals belong to a different universality class than films (Kötzler *et al.*, 1994a), rather than pointing to a lack of universality of the transition. Curiously, previous work on NCCO films (Yeh *et al.*, 1992) did not yield exponents consistent with YBCO films, but instead are closer to those of YBCO crystals. Furthermore, work done on Bi2223 gives exponents which match neither YBCO film nor YBCO crystal data. These results suggest that more experiments are necessary to establish the existence of universality, which motivates this work on NCCO and YBCO films, and our investigation of the anomalous low-field results. Concurrently with this work, Chang, Lue, and

Chou (1994) found z=7, ν=0.75 for an YBCO film in ambient field, (similar to what we find at low field), but these authors did not present any data taken in an applied field.

Another open question is the nature of the low-temperature phase. If the VG or the CC model correctly describes the method of dissipation below T_g, then Eq. 1.14 should fit the low T data. While very good fits to the data are obtained (both here and in the literature), several odd features result-- such as a current dependence of the exponent μ. The extraction of μ from this data is discussed.

Understanding the role of defects, dimensionality, and anisotropy in determining the phase diagram and low-temperature properties of HTS continues to be an interesting challenge.

Table 1.2. Overview of critical exponents reported in the literature.

System	ν	z	$2\nu_0$	field (T)	thickness (μm)	width (μm)	Reference
YBCO film							
$\rho(J)$ H‖c	1.7	4.8(2)		0.5-4	0.4	8	Koch 1989
$\rho(J)$ H‖c	1.9	4.8		2	0.3		Dekker 1992
$\rho(J)$ H‖c $\rho(J)$ H⊥c	1.0 - 1.2 1.0 - 1.2	4.8 6.0		4 - 6	0.28	10	Silver 1993
$\rho(J)$ H‖c	1.2(6) - 0.7(2)	5.6 (1.0) - 9.7(7)	*	1 - 3		5.6 - 0.54	Ando 1992
$\rho(J)$ H‖c	1.4(1) 1.1(1)	6.1(2) 8.3(3)	1.5 -	0.01 - 5 0 - 0.015		50	This work
$\sigma(\omega)$ H‖c	1.1(4)	5.2(6)		0.55			Olsson 1991
$\rho(J)$ H‖c	1.6(2)	4.9(2)	1.5	0.5-6	0.1	42	Xenikos 1993
$\rho(J)$	1.8(1)	5.0(1)		0.25-5	0.4	70	Deak 1993
$\rho(J)$ H‖c, H⊥c	1.70(2)	5.8(1)		5	0.35	20	Wöltgens 1993
$\sigma(\omega)$ H‖c	1.7(2)	5.5(5)	1.5(2)	0.4-4	0.25	radius =1500	Kötzler 1994b
$\rho(J)$	0.75	7		0	0.2	100	Chang 1994
YBCO crystal							
$\sigma(\omega)$ H‖c $\sigma(\omega)$ H⊥c	3.1(3) 1.6(3)	3.1(3) 6.3(3)		0.4-12			Kötzler 1994a
$\rho(J)$ H‖c, H⊥c	0.65(5)	3.0(2)	1.33	0.1-7	20		Yeh 1993a
monocrystal $\rho(J)$ H‖c	2(1)	4.3 (1.5)	1.33	1.5 - 6	100	2000	Gammel 1991
polycrystal $\rho(J)$ H‖c	1.1(2)	4.6(2)		0.05 - 1.5	300	1500	Worthington 1991
polycrystal $\rho(J)$ H‖c	1.4(2)	3.0(2)		50 mT- 8 mT	2000	2000	Tiernan 1992
NCCO							
film $\rho(J)$ H‖c	1.6(2) 1.0(1)	5.1(3) 7.3(1)	1.3 1.3	0.1 - 1 .001-.03	180	200	This work
film $\rho(J)$ H‖c $\rho(J)$ H⊥c	2.1 2.7	3.0 2.5	1.2 1.6	0-0.63	180		Yeh 1992
Bi2223							
film H‖c $\rho(J)$	12.2	0.69		0.5-4	0.06-0.1	20-50	Yamasaki 1994
tape H‖c $\rho(J)$	8.5(1.5)	1.25(15)	2.5	0.4-1.2	60	5000	Li 1994

* see Appendix C

CHAPTER 2
THEORY

2.1 General

FFH propose that even though long-range positional order of the vortex lattice is destroyed in the presence of random pinning, a form of long-range order remains for temperatures below the vortex glass transition temperature T_g. They suggest that, below T_g, the vortices become fixed at sample-specific locations determined by vortex interactions with each other and with pinning sites. Because the vortices are immobile in this state, there exists a non-trivial long-range order in the phase ϕ of the superconducting order parameter Ψ. Since the vortices are immobile, once the gauge invariant phase has been set at one point in the system, the phase at any point is determined. The pattern of the long-range order is random, reflecting the random positions of the vortices. Although the phase is random in space, in the vortex glass state (below T_g) it is frozen in time, analogous to spin orientations in a spin glass. (The phase coherence described above is also referred to as off-diagonal long-range order, ODLRO.) Above T_g, the vortices are thought to be in a vortex liquid state with short-range correlations, but no long-range order of any kind; the vortices move freely and there is no superconductivity.

The vortex glass model envisions that dissipation occurs via thermal nucleation and subsequent growth of vortex loops. A wavy vortex line may be thought as a combination of a straight vortex line and vortex loops, as shown in Fig. 2.1.

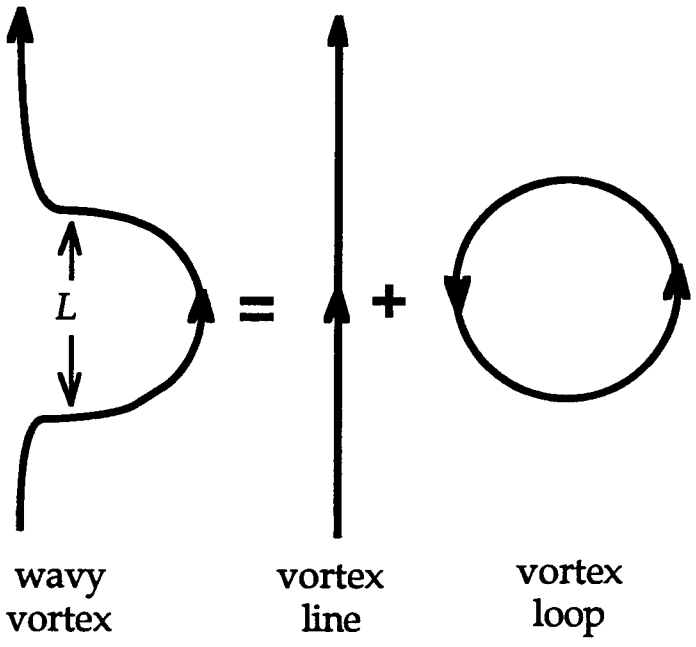

Figure 2.1. A deformed vortex line. A vortex line with wiggles may be considered the superposition of a straight vortex line and vortex loops. The size of the vortex loop excitation is characterized by L.

For temperatures greater than T_g, the thermally-nucleated loops are large enough that they grow to infinity, resulting in dissipation. For temperatures below T_g, the loops collapse and there is no dissipation. (Dissipation is often referred to as phase-slip.)

The transition from vortex liquid to vortex glass is expected to be second-order (owing to impurities) and as a consequence critical scaling applies within the critical regime; the transition should be characterized by length ξ_{VG} and time τ scales which diverge at the vortex glass transition temperature T_g as

$$\xi_{VG} \propto \left|1-\frac{T}{T_g}\right|^{-\nu} \quad \text{and} \quad \tau \propto \xi_{VG}^{z} \tag{2.1}$$

where ν and z are the static and dynamic critical exponents respectively. FFH propose that the relevant length scale is the vortex glass correlation length ξ_{VG} which is the length over which the phase is correlated; the appropriate time scale τ is vortex glass correlation time, which is essentially the time it takes a fluctuation the size of ξ_{VG} to relax (Huse, Fisher, and Fisher, 1992). A dimensional argument leads to the ansatz the resistivity ρ versus current density J isotherms will scale according to

$$\rho(J) \propto \xi_{VG}^{d-2-z} F_{\pm}\left(\frac{J\xi_{VG}^{d-1}\phi_o}{k_B T}\right) \tag{2.2}$$

where the $F_{\pm}$ are universal scaling functions and d is the dimensionality (§ 2.3). This expression is valid for any second-order normal-to-superconducting phase transition. Assuming a dimensionality of three, Eq. 2.2 may be written as

$$\rho(J) \propto \xi_{VG}^{1-z} F_{\pm}\left(\frac{J\xi_{VG}^{2}\phi_o}{k_B T}\right). \tag{2.3}$$

For finite J and T, the resistivity should be finite. Therefore, ξ_{VG} must cancel in the above equation at T_g, since ξ_{VG} diverges at the transition. For this to occur $F_{\pm} \sim \xi_{VG}^{z-1}$ at T_g or, equivalently,

$$F_{\pm}\left(\frac{J\xi_{VG}^{2}\phi_o}{k_B T_g}\right) \sim \left(\frac{J\xi_{VG}^{2}\phi_o}{k_B T_g}\right)^{\frac{(z-1)}{2}} \sim \left(\frac{J\phi_o}{k_B T_g}\right)^{\frac{(z-1)}{2}} \xi_{VG}^{z-1}. \tag{2.4}$$

Substituting this back into Eq. 2.3 we find that ρ has a power law dependence on J at T_g,

$$\rho(J) \sim J^{\frac{(z-1)}{2}}. \qquad 2.5$$

Defining a characteristic current scale J_{nl} as

$$J_{nl} = \frac{k_B T}{\phi_o \xi_{VG}^2} \qquad 2.6$$

Eq. 2.3 may be written as

$$\rho(J) \propto \xi_{VG}^{1-z} F_{\pm}\left(\frac{J}{J_{nl}}\right). \qquad 2.7$$

Vortex glass theory predicts that, above T_g, F_+ should describe a vortex liquid, which is anticipated to have a current-independent resistivity ρ_{lin} at low current densities. Therefore, F_+ should approach a constant as $\frac{J}{J_{nl}} \to 0$ and Eq. 2.7 becomes

$$\rho(T > T_g,\ \frac{J}{J_{nl}} \to 0) = \rho_{lin} \propto \xi_{VG}^{1-z}. \qquad 2.8$$

Using $\xi_{VG} \propto \left|1 - \frac{T}{T_g}\right|^{-\nu}$ (Eq. 2.1) the above equation may be written as

$$\rho_{lin} = \rho_o \left|1 - \frac{T}{T_g}\right|^{\nu(z-1)}. \qquad 2.9$$

Eq. 2.7 may now be written in the succinct form

$$\frac{\rho}{\rho_{lin}} = F_{\pm}\left(\frac{J}{J_{nl}}\right). \qquad 2.10$$

To elaborate on the above ideas, issues related to second-order phase transitions and critical scaling will be outlined in § 2.2. Then, a plausibility argument leading to the scaling equation (Eq. 2.2) will be presented in § 2.3. In

§ 2.4-2.6, the vortex glass theory will be developed more fully. The collective creep model will be sketched in § 2.7.

2.2 Second Order Phase Transitions and Critical Scaling

Transitions occur owing to interparticle interactions (e.g. in a fluid) or to quantum correlations (e.g. in ^{4}He) (Uzunov, 1993; Yeomans, 1992). (The latter are referred to as pseudo-interactions.) Interactions can lead to cooperative behavior, resulting in ordering, but thermal fluctuations interfere with this cooperation. Different phases usually arise from the dominance of either interactions or thermal fluctuations. The order in a system is quantified by the order parameter φ, usually defined such that it is zero in the disordered state and positive in the ordered state. The order parameter can be scalar (density in a fluid), vector (magnetization in a ferromagnetic) or complex (a wavefunction in superfluid ^{4}He).

A transition is first order if the first derivative of the thermodynamic potential is discontinuous, but is second order if the first derivative is continuous but the second derivative is discontinuous. In a second-order transition the phases become indistinguishable at the transition; this thermodynamic state is called the critical state and the behavior occurring near this point is called critical behavior.

A gradual increase in correlations characterizes second-order phase transitions. The distance over which correlations occur is given by the correlation length ξ, which becomes infinite at the transition temperature, T_t

$$\xi \approx \left| 1 - \frac{T}{T_t} \right|^{-\nu} . \qquad 2.11$$

(This correlation length ξ should not be confused with the superconducting coherence length presented in § 1.1.) For example, consider a magnetic system where the spins are aligned in the ordered phase but random in the disordered phase. At high temperatures, the system is completely disordered. As T_t is approached, small regions begin to form in which the spins are aligned, as exemplified in Fig. 2.2. The maximum size of these regions is The

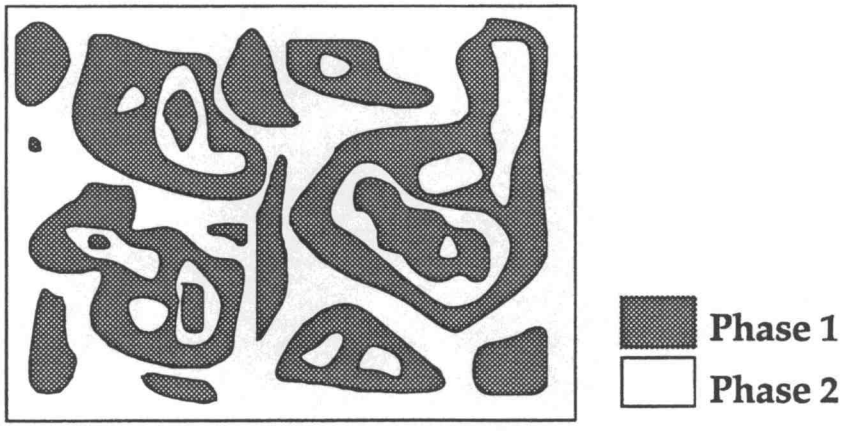

Figure 2.2. Critical fluctuations. As criticality is approached, fluctuations occur on all length scales up to ξ. Each fluctuating region contains smaller regions of fluctuations.

maximum size of these regions is characterized by ξ. The regions are not uniform, but contain smaller fluctuating regions, and even smaller fluctuating regions occur within these. Thus, there are correlated regions of all sizes up to ξ. Just below T_t, most of the system is ordered with regions (all sizes up to ξ) which are disordered. (The system is not completely ordered except at T=0.)

The order parameter φ can be written as the sum of its equilibrium value $\bar{\varphi}$ and a fluctuating part $\delta\varphi$,

$$\varphi = \bar{\varphi} + \delta\varphi. \tag{2.12}$$

The equilibrium value $\bar{\varphi}$ is the statistical average of φ,

$$\bar{\varphi} = \langle\varphi\rangle. \tag{2.13}$$

The average of the fluctuations is zero

$$\langle\delta\varphi\rangle = 0 \tag{2.14}$$

but the fluctuations exhibit strong correlation properties so that the correlation functions $\langle\delta\varphi^m\rangle$, (m=2,3...) can be large. The instability of the phases near T_t is due to large fluctuation correlations. Of particular interest is the pair (two-point) correlation function $G(R)$ which quantifies the correlation between two points separated by a distance R,

$$G(R) = \langle\delta\varphi(x)\delta\varphi(x+R)\rangle. \tag{2.15}$$

Away from criticality, G(R) decreases exponentially with distance,

$$G(R) \sim R^{-\frac{(d-1)}{2}} e^{-\frac{R}{\xi}} \tag{2.16}$$

for $R > \xi$, $0 \neq 1 - \frac{T}{T_t} << 1$, and $d > 2$. At criticality, $\xi \to \infty$ and Eq. 2.16 is no longer valid; instead, the correlation function decreases with distance as a power law,

$$\mathrm{G(R)} \sim \frac{1}{R^{d-2+\eta}} \tag{2.17}$$

where η is a critical exponent (Yeomans, 1992).

In the VG theory, the order parameter is the superconducting wavefunction ψ and the gauge invariant correlation function is (Fisher, Fisher, and Huse, 1991)

$$G_{VG}(r)=\overline{\left|\left\langle \psi^{*}(r')\exp\left[\frac{i2e}{\hbar c}\int_{r'}^{r'+r}\mathbf{A}\cdot d\mathbf{l}\right]\psi(r+r')\right\rangle\right|^{2}} \qquad 2.18$$

where $\langle\ \rangle$ denotes a thermal average and the overbar indicates a spatial average over r.

The order parameter is time-independent only if the system is in thermal equilibrium; the time it takes the system to return to equilibrium after a disturbance is given by the relaxation time τ. Time dependent (dynamic) critical phenomena are important in understanding transport properties such as thermal and electrical conductivity and sound propagation (Hohenberg and Halperin, 1977). In analogy with the static case, the order parameter is represented as

$$\varphi(x,t)=\overline{\varphi}(x)+\delta\varphi(x,t) \qquad 2.19$$

and we define

$$G(t-t')=\langle\delta\varphi(t)\delta\varphi(t')\rangle. \qquad 2.20$$

When the size of the fluctuating regions become large, the time required for ordering (or disordering) becomes long. Thus, the relaxation time becomes long near T_t,

$$\tau\propto\xi^{z}. \qquad 2.21$$

The scaling ansatz Eqs. 2.21 and 2.11 are supported by renormalization group ideas and calculations (Fisher, 1987).

The scaling hypothesis was pioneered by Kandoff (1971) using a block-spin approach, and developed into the revolutionary renormalization approach of Wilson, who received the Nobel prize in 1982 (Yeomans, 1992). Near the transition, ξ is larger than all other relevant lengths in the problem and can be regarded as the only important length. Finite-range effects (such as the details of the interaction potential) should not be essential to the critical behavior. Since at the transition fluctuations occur on all length scales, the properties of the system are unaltered by a change in scale. Kandoff imagined breaking the system into blocks of length La, where a is the interparticle spacing (as exemplified in Fig. 2.3) and $a < La << \xi$. The enlargement of the block size from aL to aL' ($aL < aL' << \xi$) removes the short-range ($\leq aL'$) effects of the interparticle interactions. As ξ increases, the size of the interacting units is increased (rescaled). Individual spins are replaced by the average spin of each block; instead of focusing on interacting spins, interactions between blocks of spins are considered. As ξ grows, so does the block size, in such a way that the thermodynamic functions are rescaled but do not change form.

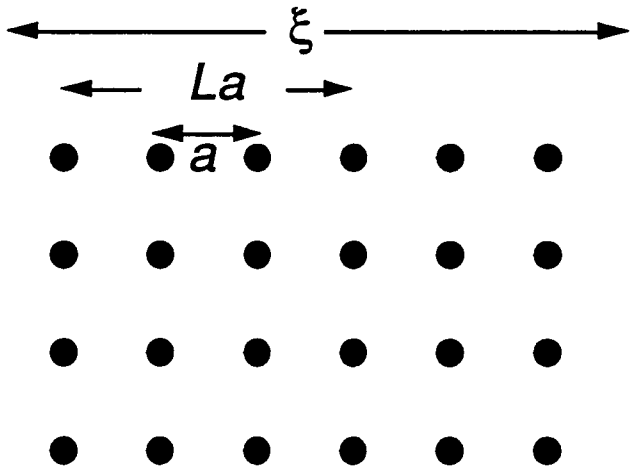

Figure 2.3. Kandoff's block spin approach. Shown is an array of sites with spacing a. The lattice is divided into cells of length La on each side, such that $a<La<\xi$.

Implementing the scaling hypothesis is made easier using dimensional analysis (Ma, 1976; Barenblatt, 1987; Kandoff, 1971). A scale transformation which changes a length interval Δx to $\Delta x'$ is,

$$\Delta x \rightarrow \Delta x' = s^{-1}\Delta x. \qquad 2.22$$

A scale transformation with s=3 triples the unit of length. The scale dimension (or simply dimension) of Δx is -1. If a scale transformation changes A to A' according to

$$A \rightarrow A' = s^{-\lambda}A \qquad 2.23$$

then the scale dimension of A is λ. The scale dimension of $(\Delta x)^2$ is -2 and that of volume is $-d$.

2.3 Justification of the Scaling Equation

Wolf, Gubser, and Imry (1979) presented the first scaling equations for a superconducting transition that the author is aware of. [The scaling expression of Wolf, Gubser, and Imry can be written in the form used here and by FFH (Chang, Lue, and Chou, 1994).] Following Blatter *et al.* (1994), a dimensional argument leading to the scaling equation (Eq. 2.2) is as follows. The vector potential scales as inverse length. Since

$$E \propto \frac{\partial A}{\partial t} \tag{2.24}$$

the electric field E should scale as

$$\xi^{-1}\tau^{-1} = \xi^{-z-1}, \tag{2.25}$$

so the appropriate scaling combination for the electric field is

$$E\xi^{z+1}. \tag{2.26}$$

The total free energy is not changed under a scale transformation, so it has scale dimensions of zero (Ma, 1976). Therefore, the free energy density f scales as d. According to FFH (1991),

$$J = \frac{\partial f}{\partial \mathbf{A}} \tag{2.27}$$

so that J should scale as

$$\xi\xi^{-d} = \xi^{1-d}. \tag{2.28}$$

This gives the scaling combination for J as

$$J\xi^{d-1}. \tag{2.29}$$

Evidently, the appropriate scaling relation is (Barenblatt, 1987; Blatter *et al.*, 1994)

$$(scaled\ E) \propto (scaled\ J) F_{\pm}[scaled\ J] \qquad 2.30$$

or,

$$E\xi_{VG}^{z+1} \propto J\xi_{VG}^{d-1} F_{\pm}\left(J\xi_{VG}^{d-1}\right) \qquad 2.31$$

which may be written as,

$$E \propto J\xi_{VG}^{d-1-z-1} F_{\pm}\left(J\xi_{VG}^{d-1}\right) \qquad 2.32$$

or,

$$\rho \propto \xi_{VG}^{d-2-z} F_{\pm}\left(J\xi_{VG}^{d-1}\right), \qquad 2.33$$

which is essentially Eq. 2.2. The existence of a scaling relation provides evidence for a phase transition, but does not give a physical description of the ordered phase or the dissipative mechanism at low temperatures.

2.4 Dissipation via the Nucleation and Growth of Vortex Loops

Even with no field applied there is a finite probability that a vortex loop will nucleate. The energy of a vortex loop of radius R, in the absence of currents, is given by the elastic energy

$$U_E \sim 2\pi R\varepsilon_1, \qquad 2.34$$

where ε_1 is the energy per unit length of the vortex, or the line tension. There is a corresponding inward elastic force on the vortex loop since $\mathbf{F}_E = -\nabla U_E$, so

$$F_E \sim 2\pi\varepsilon_1. \tag{2.35}$$

This elastic force causes the thermally nucleated vortex loops to collapse.

However, if a current is flowing in the superconductor, there will also be an outward Lorentz force on the vortex loops. The energy gained by having a vortex loop in a region of uniform current density J can be estimated as follows. The Lorentz force on a magnetic loop (actually a donut-shaped tube) is given by

$$\mathbf{F}_J = \int (\mathbf{J} \times \mathbf{B}) dV. \tag{2.36}$$

Assuming $J \perp B$, $B \sim$ constant in the flux tube and zero otherwise,

$$F_J = JBV. \tag{2.37}$$

The volume V of the vortex tube is given approximately as the cross-sectional area of the tube a multiplied by the average circumference of the tube $2\pi R$. The magnetic flux in a vortex tube is equal to $\phi_o = Ba$. Therefore,

$$V = a2\pi R = \frac{2\pi R\phi_o}{B}. \tag{2.38}$$

Substituting this into Eq. 2.37 gives the outward Lorentz force F_J on the flux tube,

$$F_J = 2\pi\phi_o JR, \tag{2.39}$$

The energy gained by creating a loop is given by

$$\begin{aligned} U_J &= -\int_0^R \mathbf{F}_J \cdot d\mathbf{l} \\ &= -\phi_o \pi J R^2 \end{aligned} \tag{2.40}$$

The total free energy of a vortex loop is given by summing the elastic (Eq. 2.35) and Lorentz (Eq. 2.40) energies,

$$U \sim 2\pi R\varepsilon_1 - \phi_o \pi J R^2. \qquad 2.41$$

When the Lorentz force is greater than the elastic force we expect the thermally activated vortex loops to grow and dissipation to occur.

The critical radius R_c at which a thermally nucleated vortex will grow, due to the Lorentz force of the current, is found by minimizing U with respect to R giving,

$$R_c \sim \frac{\varepsilon_1}{J\phi_o}. \qquad 2.42$$

The free energy barrier is then given by $U(R_c) = \frac{\pi \varepsilon_1^{\,2}}{J\phi_o}$. The Boltzman probability of nucleating a vortex loop with a radius equal to R_c is

$$\exp -\left[U(R_c)/k_B T\right] = \exp -\left[\frac{\pi \varepsilon_1^{\,2}}{J\phi_o k_B T}\right]. \qquad 2.43$$

Defining a characteristic "thermal current density" J_T (set by the temperature) as,

$$J_T = \frac{\pi \varepsilon_1^{\,2}}{\phi_o k_B T} \qquad 2.44$$

Eq. 2.43 may be written as,

$$\exp -\left[\frac{J_T}{J}\right]. \qquad 2.45$$

Vortices moving with a velocity v create an electric field E which is proportional to v. According to Fisher (1993), the velocity is given by a

characteristic distance multiplied by a rate, where the rate is proportional to the Boltzman factor multiplied by the current, so

$$E \approx v \approx J \exp\left(-\frac{J_T}{J}\right). \qquad 2.46$$

Some authors (e.g., Fisher, Fisher, and Huse, 1991) do not include this last factor of J in the calculation resulting in

$$E \approx v \approx \exp\left(-\frac{J_T}{J}\right). \qquad 2.47$$

Eqs. 2.46 and 2.47 are approximately equal since (for isotherms below T_g) the current range over which E (or ρ) increases is small, and J~constant. Eq. 2.46 yields a resistivity of

$$\rho(J) \approx \exp\left(-\frac{J_T}{J}\right) \qquad 2.48$$

This is the expression FFH write for the resistivity in zero applied field, e.g. dissipation in the Meissner state. When there is an applied field, Fisher (1989) and FFH anticipate a length dependence of the free-energy barrier.

2.5 Length Dependence of the Free Energy Barrier

Flux creep treats vortices as point objects moving across a potential landscape (see § 1.4). However, vortices are extended objects, provided the anisotropy is sufficiently small that the superconducting layers are strongly coupled. Therefore, the energy barrier for vortex movement or loop nucleation may depend on length. Fisher (1989) and FFH propose that the

free energy F_L of a vortex loop excitation (see Fig. 2.1) will grow with the length L of the excitation as

$$F_L \approx \mathrm{Y} L^{\theta}. \tag{2.49}$$

where Y is the stiffness coefficient and θ is the stiffness exponent. (To provide some motivation for Eq. 2.49, it is useful to consider an Ising system; see Appendix A.) If $\theta > 0$ then excitations are energetically costly and unlikely to occur, but if $\theta < 0$ then excitations are cheap and occur readily. When the system is at the lower critical dimension, $\theta = 0$. Thus an ordered state can exist only if θ is positive. The free energy barrier B_L to create a vortex loop excitation will grow at least as fast as the loop energies,

$$B_L \sim \Delta L^{\psi} \tag{2.50}$$

where $\psi \geq \theta$. This ansatz was used by Fisher (1987) and Fisher and Huse (1988) to describe the properties of the ordered phase of spin glasses. The Lorentz energy $-\phi_o \pi J R^2$ (Eq. 2.40) is generalized to $\phi_o J \mathcal{A}$ where $\mathcal{A}$ is the effective projected area of the excitation normal to J. It is assumed that $\mathcal{A}$ scales with length as $\mathcal{A} \sim L^{\kappa}$, with $\kappa \leq d-1$ (for a loop $\kappa = 2$) so that the Lorentz energy scales as

$$\phi_o J L^{\kappa} \tag{2.51}$$

Setting this equal to the excitation energy $\mathrm{Y} L^{\theta}$, we find that a current J creates a vortex excitation with a characteristic size

$$L \sim \left(\frac{\mathrm{Y}}{\phi_o J} \right)^{\frac{1}{\kappa - \theta}}. \tag{2.52}$$

Therefore, the free energy barrier should scale with current as

$$B_L \sim \Delta\left(\frac{Y}{\phi_o J}\right)^{\frac{\psi}{\kappa-\theta}}. \qquad 2.53$$

Following the arguments leading to Eq. 2.48, the resistivity is (Fisher, 1993),

$$\begin{aligned}\rho(J) &\propto \exp\left(\frac{B_L}{k_B T}\right) \\ &\approx \exp\left(\frac{\Delta}{k_B T}\left(\frac{Y}{J}\right)^{\frac{\psi}{\kappa-\theta}}\right).\end{aligned} \qquad 2.54$$

With $\mu = \frac{\psi}{\kappa-\theta}$, we write this as (c.f. Eq. 1.14)

$$\rho(J) \propto \exp\left[-\left(\frac{J_o}{J}\right)^{\mu}\right] \qquad 2.55$$

2.6 Universality and the Predicted Values of the Critical Exponents

The critical exponents for a system should depend only on the universality class to which it belongs (Yeomans, 1992; Binney *et al.*, 1992). For models with short-range interactions, the static universality class should vary with the spatial dimensionality d and the symmetry index n of the order parameter, but not on the detailed interactions in the system. The symmetry index is the number of components in the order parameter (Uzumov, 1993). In a fluid (φ=density) n=1. In a ferromagnet (φ=magnetization) $1<n<3$ depending on the type of magnetic ordering. In a system with complex structure, n can be larger than 3. Above the upper critical dimension d_u of the system, the exponents lock into d-independent values, given by mean-

field theory. There are additional factors which determine the dynamic universality class, such as the conservation laws and the equation of motion for the order parameter (Hohenberg and Halperin, 1977). The vortex glass transition is assumed to belong to the same universality class as magnetic spin glasses (Fisher, Fisher, and Huse, 1991). (For a review of spin glasses see Binder and Young, 1986.)

Several numerical calculations have been performed which attempt to estimate the critical exponents. Most of these assume that the vortex glass state is adequately described by the Hamiltonian for the gauge glass model,

$$H = -\sum_{\langle ij \rangle} J_{ij} \cos(\phi_i - \phi_j - A_{ij}) \qquad 2.56$$

where ϕ_i is the phase of ψ at the ith lattice site, J_{ij} is the Josephson interaction between sites i and j (usually taken to be a positive constant $J_{ij}=J_o$), and A_{ij} is the vector potential between to grains,

$$A_{ij} = \frac{2\pi}{\phi_o} \int_i^j A(\bar{r}) dl \qquad 2.57$$

In the gauge glass model A_{ij} is a random number between 0 and 2π. (In the XY spin glass model A_{ij} is chosen randomly to be either 0 or π, in the XY ferromagnet $A_{ij}=0$, and in the XY antiferromagnet $A_{ij}=\pi$.) The gauge glass model was presented by Ebner and Stroud (1985) to describe samples with superconducting grains weakly coupled via either the proximity effect or Josephson tunneling. It is hoped that this Hamiltonian (Eq. 2.57) includes the correct symmetry of the order parameter, randomness, and frustration. Current and voltage are often introduced into the problem via the Josephson current-phase relation

$$J_{ij} = J_c \sin\left(\phi_i - \phi_j - A_{ij}\right) \qquad 2.58$$

and the Josephson voltage-phase relation

$$V_{ij} = \frac{\phi_o}{2\pi}\frac{d}{dt}\left(\phi_i - \phi_j\right) \qquad 2.59$$

where J_c is the Josephson critical current.

In developing a mean-field model for the VG transition (valid in dimensions greater than or equal to d_u=6) Dorsey, Huang, and Fisher (1992) extracted the values $z = 4$ and $\nu = 0.5$, the same result as obtained for Ising spin glasses. This model used the Ginzburg-Landau Hamiltonian, model A dynamics (which assumes a nonconserved order parameter; see Hohenberg and Halperin, 1977), and introduced quenched disorder by defining a random T_C; the work closely paralleled calculations for spin glasses. It is expected that both z and ν increase with decreasing dimensionality, but in 3D z may not increase as much as it does in the Ising model, $z_{Ising} = 6 \pm 1$ (Fisher, Fisher, and Huse, 1991). A first order expansion in $\varepsilon = 6 - d$ about $d = 6$ for the gauge glass model (Houghton and Moore, 1988) yields the result $\nu = \frac{1}{2} + \frac{5\varepsilon}{24}$; for $d = 3$ ($\varepsilon = 3$) this corresponds to $\nu \sim 1.1$ (though one might question the extension of the expansion to $d = 3$, since $\varepsilon = 3$ is not small). Using finite-temperature Monte-Carlo simulations of the size-dependence of the domain wall energy, Reger *et al.* (1991) determined $\nu = 1.3 \pm 0.4$, $z = 4.7 \pm 0.7$ for the gauge glass model. Thus, it is expected that $z \approx 4 - 7$ and $\nu \approx 1 - 2$ for the VG phase transition.

FFH predict that $0 < \mu < 1$. Moore and Murphy (1994) performed a real-space renormalization-group calculation using the gauge glass model; they found $\psi = \theta \approx 0.26$ and argued that $\kappa = d - 1$, resulting in $\mu \approx 0.15$.

Numerical calculations indicate that the lower critical dimension $d_l \leq 3$. Using domain-wall renormalization group calculations, Reger *et al.* (1991) found $\theta \cong 0$ for a 3D gauge glass, suggesting that d_l to be just less than or equal to 3. Cieplak *et al.* (1992) used a Migdal-Kandoff renormalization-group scheme for the gauge glass and found $\theta = 0.26$, so $d_l < 3$.

2.7 Collective Creep

Collective creep (CC) (Feigel'man *et al.*, 1989; Natterman, 1990; Fischer and Natterman, 1991) combines collective pinning theory (Larkin and Ovchinnikov, 1979) with the ideas of Anderson and Kim (Anderson, 1962; Anderson and Kim, 1964). Like the VG model, CC also envisions that dissipation occurs via the nucleation and growth of vortex loops. However, the two theories make different assumptions about the relative sizes of the characteristic loop radius R and the extent of vortex positional correlation. The distances over which vortex positions are correlated are called the Larkin-Ovchinnikov lengths: L_c for the longitudinal direction ($\| B$), and R_c for the transverse direction ($\perp B$). The VG model assumes there is a phase coherence which extends to distances longer than the positional order R_c, and thus considers lengths $R >> R_c$. The CC model assumes weak pinning, resulting in large positional correlations lengths. In this limit, the typical loop size is smaller than the positional correlation length $R \leq R_c$ and the vortex system can be described by elastic-medium theory; the distortions of

the flux line lattice u (due to pinning, the Lorentz force, and thermal fluctuations) from a perfect, static lattice, are described by elastic continuum model, so vortices are treated as rubber bands. The free energy associated with the distortion is

$$F = \int d^3r \left[\frac{(c_{11} - c_{66})}{2} (\nabla \cdot \mathbf{u})^2 + \frac{c_{66}}{2} (\nabla_\perp \mathbf{u})^2 + \frac{c_{44}}{2} \left(\frac{\partial \mathbf{u}}{\partial z} \right)^2 + U_o \right] \qquad 2.60$$

where the c_{ii} are elastic moduli; c_{11} is the bulk, c_{44} is the tilt, and c_{66} is the shear (Brandt, 1993). The pinning potential $U_o(\mathbf{u}, \mathbf{r})$ describes the lattice interactions with defects. The compressibility $(\nabla \cdot \mathbf{u})^2$ is often neglected.

Central to the CC model is the idea (from collective pinning theory) that there is a correlation volume V_c within which the positions of vortices are correlated. The correlation volume depends on the relative sizes of L_c and the interlayer spacing l, as shown in Fig. 2.4.

If the positional correlation is longer than the interlayer spacing $L_c > l$ then the system is considered 3D, and if $L_c < l$ then the system is 2D. The correlation volume in the 3D limit is simply $V_c = L_c R_c^2$. In the 2D limit $V_c = l R_c^2$.

The CC model predicts the same low-temperature form for $\rho(J)$ as does the VG model, namely (c.f. Eqs 1.14, 2.55)

$$\rho(J) \propto \exp\left[-\left(\frac{J_o}{J} \right)^{\mu} \right]. \qquad 2.61$$

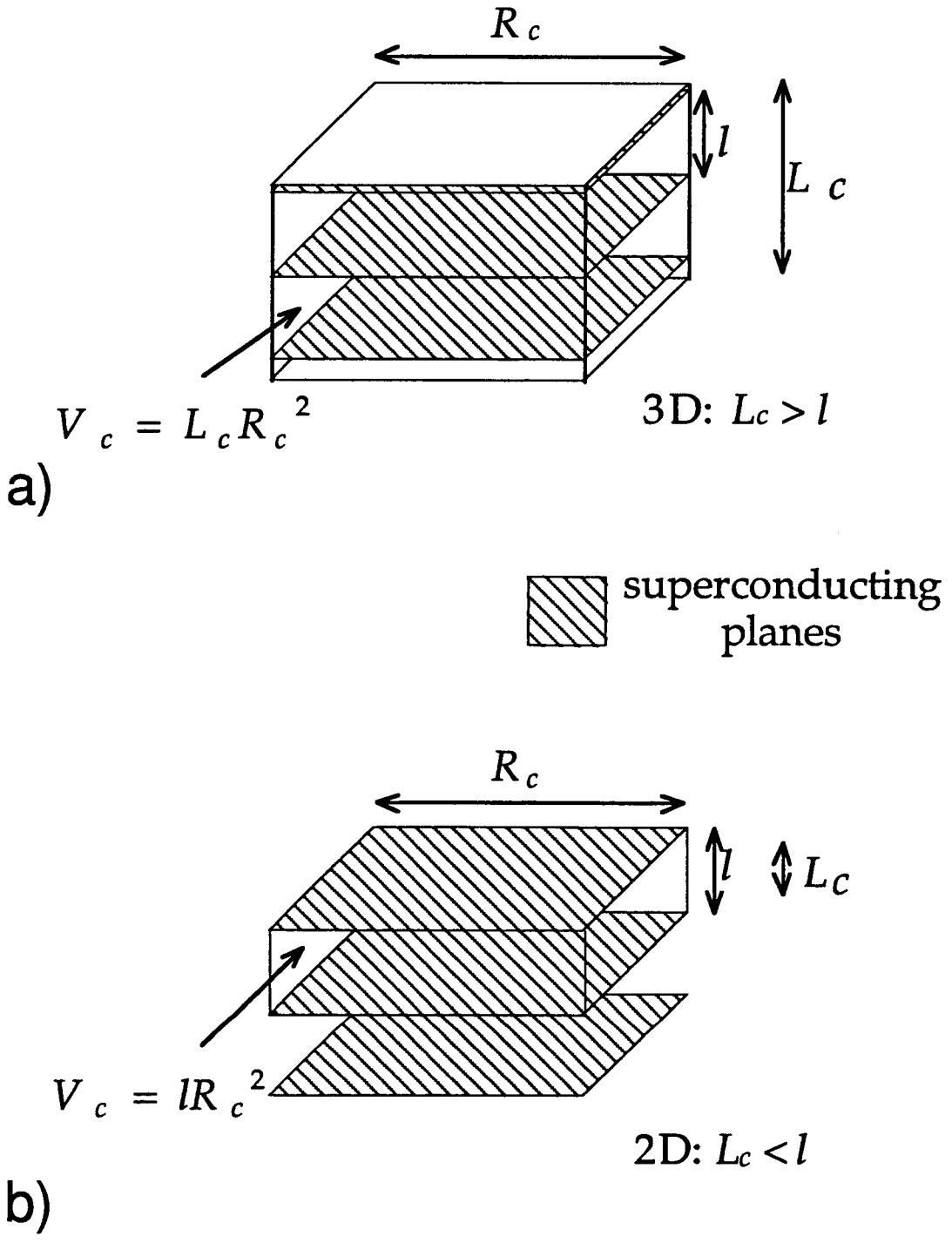

Figure 2.4. Correlation volume V_C for 2D and 3D structures. (a) 3D, when the longitudinal positional correlation is greater than the interlayer spacing $L_c > l$, and (b) 2D, when $L_c < l$.

The predicted value for μ depends both on the dimensionality of the system and on the size of V_c relative to the penetration depth λ. The correlation volume is considered large if $R_c > \lambda$, and small if $R_c < \lambda$; if the correlation length is less than the intervortex spacing $(R_c < a_0)$, single vortex pinning occurs. For 3D the predictions are $\mu = \frac{1}{7} \approx 0.14$ (single vortex pinning), $\mu = \frac{3}{2} \approx 1.5$ (small V_c), and $\mu = \frac{7}{9} \approx 0.78$ (large V_c). For 2D the predictions are $\mu = \frac{9}{8} \approx 1.12$ (small V_c), and $\mu = \frac{1}{2} \approx 0.5$ (large V_c). Recall that the VG prediction is $0 < \mu < 1$.

CHAPTER 3
EXPERIMENT

3.1 YBaCuO and NdCeCuO General Properties

Comparing the $\rho - J$ characteristics of NCCO and YBCO gives insight into the relative importance of T_c and thermal fluctuations in HTS vortex dynamics. In many ways, NCCO is an anomaly within the family of copper-oxide HTS; it has a modest T_c near 20 K which reduces the importance of thermal fluctuations. NCCO is also more anisotropic than YBCO and has a longer coherence length. A comparison of their characteristics appears in Table 1.1.

These materials have strikingly different magnetoresistance characteristics, which is evident in the contrast between their resistivity-temperature curves, shown in Fig. 3.1 (Hermann, 1992; Tate and Hermann, 1992). In YBCO the $\rho - T$ curves exhibit dramatic fan-shaped broadening with increasing magnetic field. The broadening is not as pronounced in NCCO where there is an almost parallel shift of the $\rho - T$ curves with decreasing field. Thus, critical scaling of NCCO and YBCO $\rho - J$ characteristics helps isolate the primary factors which govern vortex dynamics.

3.2 Thin Film Samples

The thin film YBCO sample was provided by P. Berberich and H. Kinder at the Technical University of Munich (Berberich *et al.*, 1988). The NCCO

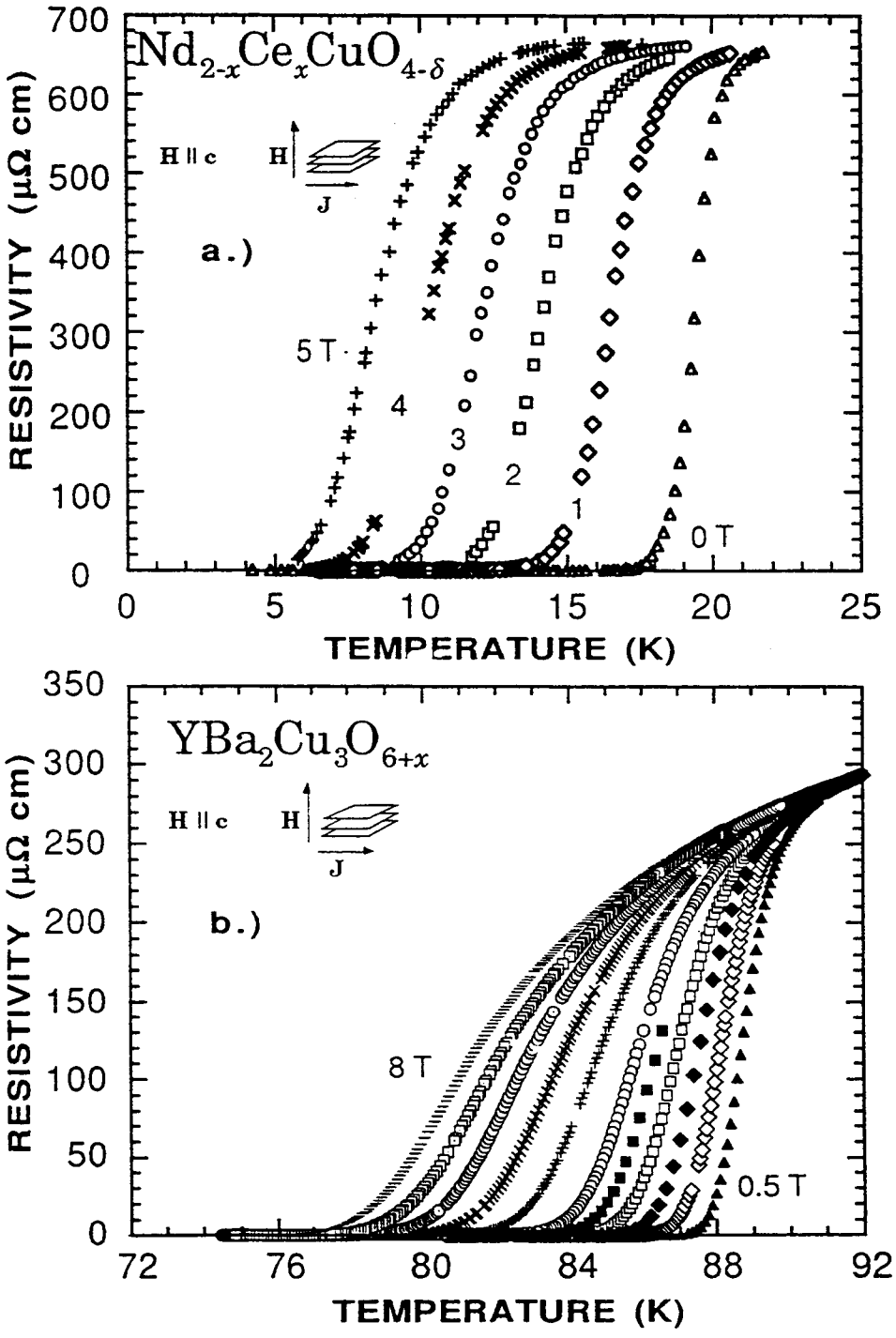

Figure 3.1. Typical magnetoresistance characteristics of HTS. (a) For an NCCO film and (b) for an YBCO film with H ‖ *c*. (From Hermann, 1992.)

sample is courtesy of S. N. Mao and X. X. Xi at the University of Maryland (Mao *et al.*, 1992). The dimensions and characteristics of the films are listed in Table 3.1.

Table 3.1. Characteristics of the thin-film samples.

material	film name	thickness (nm)	width (μm)	length (mm)	T_C (K)	ΔT_c (K)	ρ_n μΩcm	substrate
YBCO	27.08.91	160	50	0.05	86.4	2	480	MgO
NCCO	NX542	180	200	1.23	18.6	1.4	148	YSZ

All films are *c*-axis oriented, that is, with the *c* axis of the film parallel to the normal of the substrate surface. Each film was made into microbridge using wet-etching photolithography. Fig. 3.2 is a schematic drawing of the microbridges.

The YBCO film was made by thermally evaporating the constituent materials onto a MgO substrate in an oxygen atmosphere. The NCCO film was made by pulsed laser deposition onto a Y-stabilized ZrO_2 (YSZ) substrate in a nitrous oxide atmosphere.

The transition temperatures in Table 3.1 are defined by the temperature where $\rho < 10^{-3}$ μΩcm at ambient field, with a width $\Delta T_c = T_{onset}$-T_C. (T_{onset} marks the onset of the superconducting transition.) The resistivity at T_{onset} is denoted ρ_n. The $\rho - T$ plot for the NCCO film is displayed in Fig. 3.3.

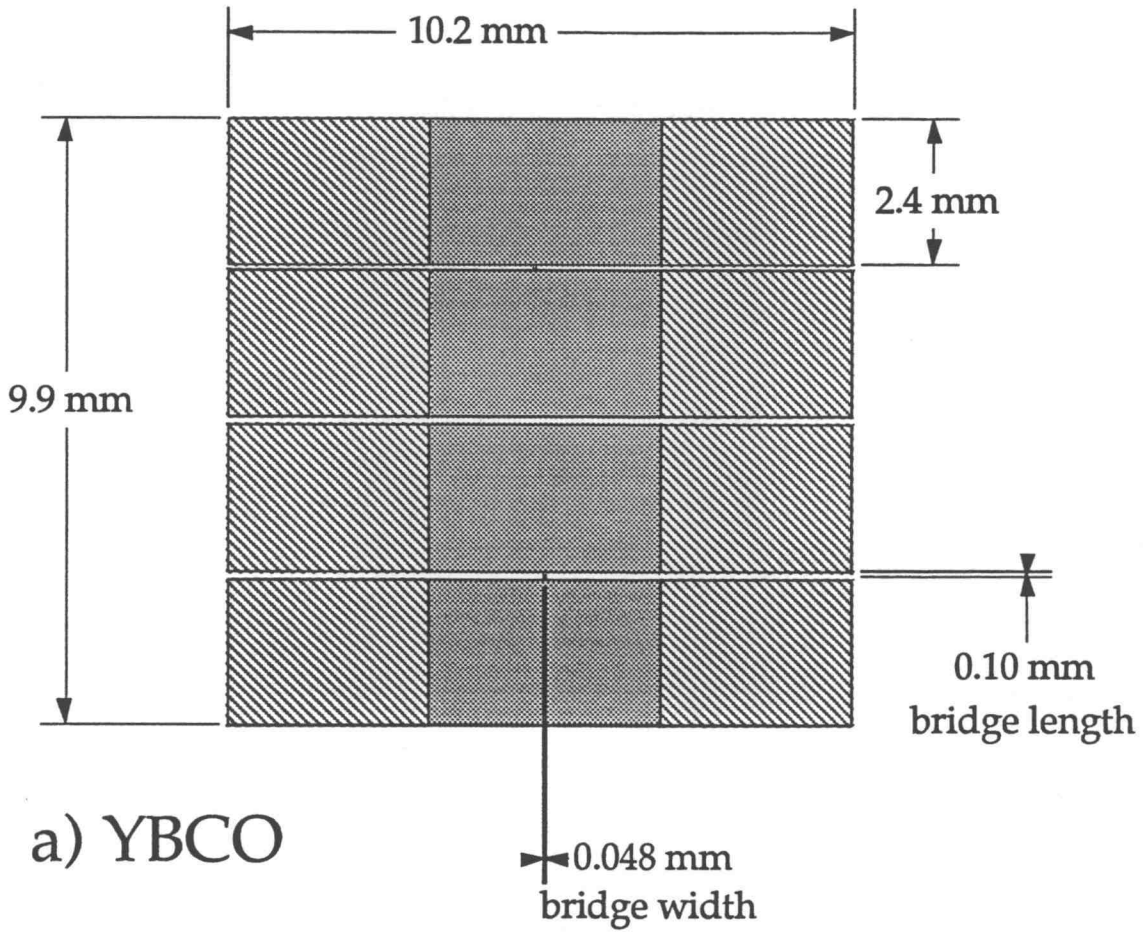

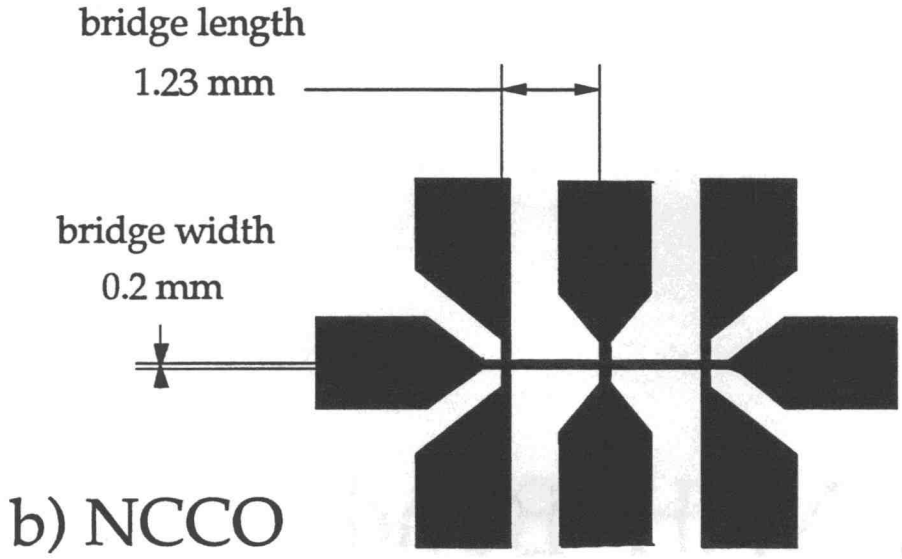

Figure 3.2. Dimensions of the thin-film samples.

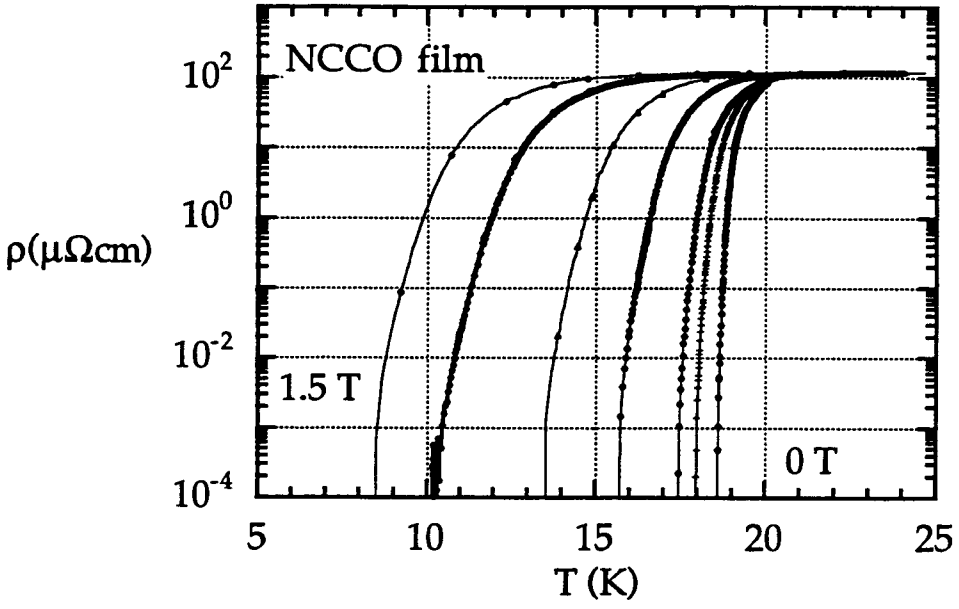

Figure 3.3. ρ-T curves for the NCCO film used in this experiment. The data are for fields ($H \parallel c$) of (left to right) 1.5 T, 1 T, 0.5 T, 0.25 T, 0.1 T, 0.05 T, and 0T.

3.3 The Standard Four-Point Configuration

Electrical contact was made to the films in a four-point configuration in order to eliminate the contact and lead resistance from the resistance measurement. In this method, the two current leads and the two voltage leads all have different contact points. Because of this, no current flows through the two voltage contacts or lead wires (provided a voltmeter with sufficiently high impedance is used). Consequently, there is no voltage drop over these; the only voltage drop is across the thin film. Therefore, a high contact resistance should cause difficulties only because of heating effects. In

practice, however, a high contact resistance can result in peculiar voltage readings, which can thwart our ability to get meaningful data at low voltages. Because of this, it is important to have low contact resistance.

The contact resistance was determined by measuring the film resistance in both two-terminal and four-terminal configurations. The two-terminal measurement includes the resistances of the film, the lead wires, and two contacts. The four-terminal measurement includes only the film resistance. Subtracting these two numbers and estimating the lead resistance yields a value for the contact resistance. The contact resistance was also estimated by measuring the two-terminal resistance of the film at temperatures well below T_c.

3.4 Sample Holder

The sample holder for each film consisted of Cu-clad PC (printed circuit) board, mounted onto a Cu block. The Cu block contained both a carbon-glass and a Pt resistance thermometer. Contact pads were photolithographically etched out of the Cu on the PC board, and a layer of Au was electroplated onto these (see Appendix B). The film was set in a pocket which was milled out of the PC board, and was held in place with screws and Silly Putty[1]. Thermal grease was applied between the sample and the Cu block[2]. Electrical contact from the sample holder to the top of the variable temperature insert was achieved using Cu wire and Au connector pins[3]. The pins were attached to

1 Silly Putty, Binney and Smith Inc., Easton, PA 18044.
2 Cry-Con grease, Lakeshore, Westerville, OH 43081.
3 R30/C socket pin, Vectorbord, Vector Electronic Company, Sylmar, CA.

both the wire and the sample holder using low-thermal-noise solder[4]. Contact from the sample holder to the film was made using thin (about 0.05 mm) Au wire. The method of attaching this wire was different for the two materials.

3.5 Contact To The Film

3.5.1 YBaCuO

Electrical contact to the YBCO sample was made using a Au ultrasonic bonding technique[5]. The film had Au pads, which had been evaporated onto the film at the Technical University of Munich. Au wire was attached both to these pads and to the Au pads of the sample holder using ultrasonic bonding, resulting in a contact resistance of about 40 Ω per contact.

3.5.2 NdCeCuO

Making electrical contact to the NCCO samples was less straightforward, perhaps owing to the presence of a high-resistance oxide layer on the surface. The technique that proved to be most successful is based on a method used by Kussmaul (1992). It differs from the YBCO contact method in that the Au wire was not bonded, but attached to the sample holder using BiPb solder, and attached to the film using Ag paint in the following manner. The film was etched in a dilute (1:10) solution of glacial acetic acid and deionized water for

4 IND #255 solder, 0.030" diameter, The Indium Corporation of America, Utica, NY 13502.
5 Martin Wybourne and John Wu, University of Oregon, Eugene, OR.

10 minutes in an ultrasonic cleaner. The acid was cleaned off with methanol for a few minutes (again in the ultrasonic cleaner). The film was then expediently placed onto a mask and then into an evaporator where about 200 nm of Au was evaporated onto the film. The Au was annealed in air for 20 minutes at 190 °C inside of a hotplate oven (a disk of ceramic placed on a hotplate and covered with a glass beaker). The Au wires were then encouraged to sit on the Au pads, and Ag paint was applied[6]. The paint was allowed to dry for at least 12 hours in air, often with a light bulb shining on it (60 °C) for an hour or two. The resulting contact resistance was less than 1 Ω per contact.

3.6 Experimental Procedure

To obtain $\rho - J$ data, the film was placed in a variable temperature insert (VTI) in a liquid-He dewar. Using a LakeShore DRC-91CA temperature controller and adjusting the liquid He flow into the VTI, temperature fluctuations and drift in the cryostat were generally held to less than 30 mK (peak-to-peak) for each isotherm, resulting in a standard deviation of less than 10 mK for each isotherm. For many of the data sets (the more recent ones), the temperature drift is less than the scatter and the standard deviation was typically 2-3 mK per isotherm. For low temperatures (near 20 K), the temperature gradient between the sample and the flow valve [at the bottom of the VTI (see Hermann, 1992)] can be made almost zero by adjusting the flow valve; for example, if the sample temperature is greater than that at the flow valve, then opening the flow valve brings the two temperatures closer. At higher temperatures (near 80 K) a temperature gradient in the system

6 Silver Print, GC Electronics, Rockford, IL 61102.

seems unavoidable. Typical P-D-I (proportional-derivative-integral) settings on the LakeShore temperature controller are 50-5-20 (near ~20 K) and 300-8-30 (near ~80 K). The temperature stability is usually better if the heater is operating in the 50-100% power range rather than in the 1-50% range. Generally, if sufficient time elapses between measuring isotherms, the temperature will be reasonably constant during the measurement.

The magnetic field was applied parallel to the *c*-axis of the sample and was generated by a 9-T NbTi superconducting magnet. For high fields (above ~50 mT), current was supplied to the magnet by a Cryomagnetics IPS-100 power supply. For low fields, either a Kepco ATE-36-8M power supply or a Keithley 220 current source was used, and the current was read by a Keithley 195A multimeter. The magnetic fields were calculated from the current in the magnet, assuming field varies linearly with current. Remnant fields and self fields may change the absolute determination of the field by a few mT; this is significant only at the lowest fields. Direct current was supplied to the film using a Keithley 220 current source and the voltage was measured by a Keithley 182 nanovoltmeter. Thermal offsets were minimized by reversing the current direction; the current was applied for 1.8 s in each direction, which represents 10% of each measurement cycle. Each reading was an average of 30 voltage measurements. We incremented the current from a value where the voltage is below our resolution of 15 nV to just below the critical current density. Each isotherm took 10 to 30 minutes to generate. The isotherms are typically 100 mK apart, except at ambient field for YBCO where they are more closely spaced. The magnet's power supply, the current source, the nanovoltmeter, and the thermometers were monitored and controlled remotely by LabView software on an Apple Macintosh Quadra 800.

3.7 Analysis Procedure: Obtaining ν, z, and T_g

At each field we measure $\rho - J$ isotherms (typically 20 - 100) around T_g. By appropriate choice of the scaling parameters T_g, ν and z, each set of isotherms collapses onto two ρ_{sc} versus J_{sc} curves, where ρ_{sc} is the scaled resistivity,

$$\rho_{sc} = \frac{\rho}{\rho_o}\left|1 - \frac{T}{T_g}\right|^{\nu(z-1)}, \qquad 3.1$$

and J_{sc} is the scaled current density,

$$J_{sc} = \frac{J}{J_o T}\left|1 - \frac{T}{T_g}\right|^{-2\nu}. \qquad 3.2$$

Therefore, when ρ_{sc} is plotted versus J_{sc} all of the isotherms for a given field collapse onto one of the two universal functions, F_+ and F_-, according to Eq. 2.3 as shown in Fig. 3.4.

To find the scaling parameters we begin by defining a range of possible T_g values from those isotherms that show neither upward nor downward curvature at low currents on a $\log\rho$ versus $\log J$ plot, since ρ should have a power-law dependence on J at T_g (see Eq. 2.5). One is chosen as the most likely critical isotherm which gives an initial value of the parameter z from the slope $\frac{(z-1)}{2}$ of the critical $\log\rho$ versus $\log J$ isotherm.

For $T > T_g$ we expect a constant resistivity ρ_{lin} at low currents and predict that it varies with T as $\rho_{lin} \propto |T - T_g|^s$ according to Eq. 2.9. So, for each isotherm with T greater than T_g, $\log\rho_{lin}$ is plotted against $\log|T - T_g|$; the plot

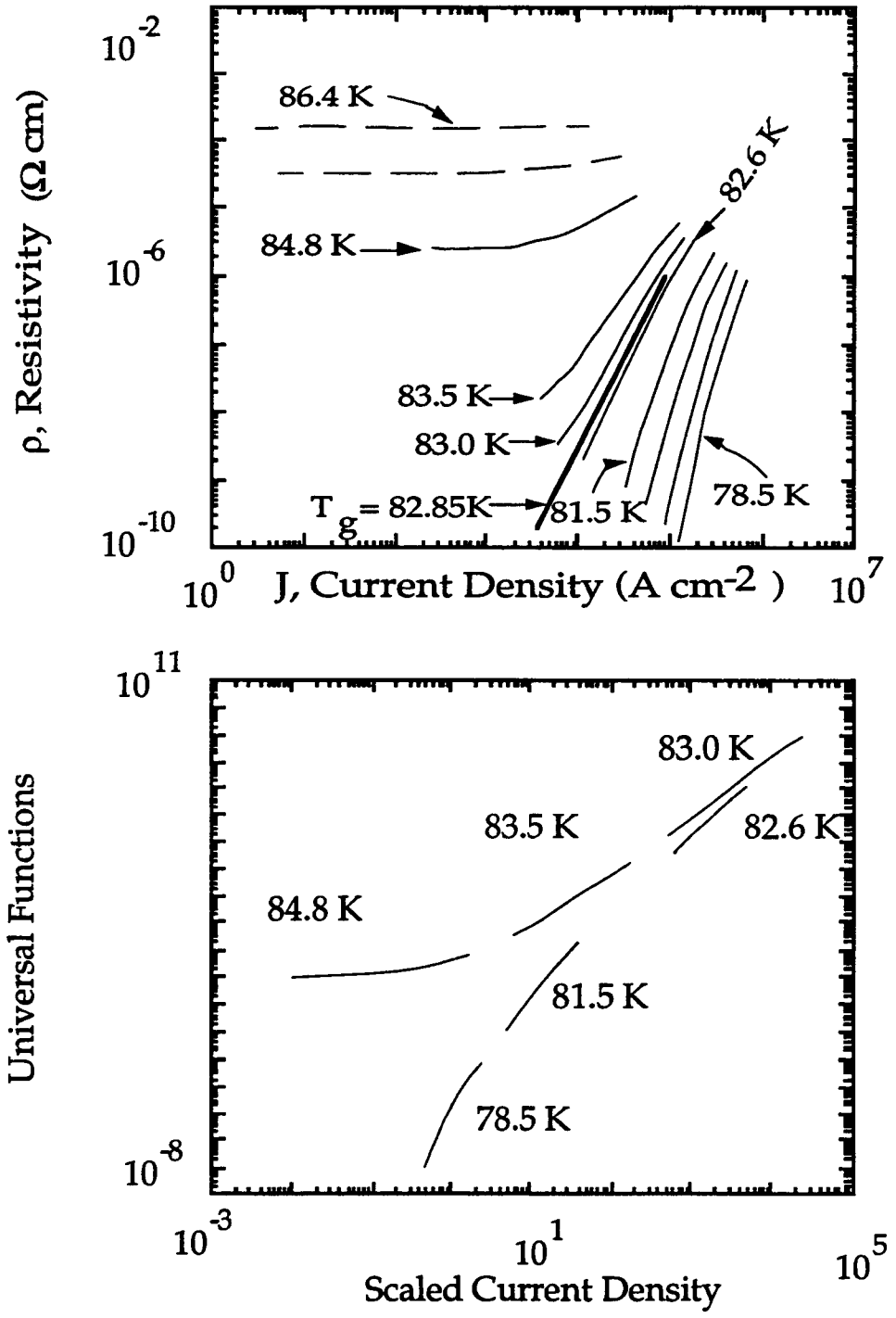

Figure 3.4. Construction of the universal functions. (a) ρ-*J* isotherms for the YBCO film in a field of 1 T and (b) the same data collapsed. The dashed isotherms are outside the scaling region. The displayed isotherms are about 1 K apart, and comprise about 10% of the data.

is linear in the critical regime, with a slope $s = \nu(z-1)$ which gives a value for ν as $\nu = \frac{s}{(z-1)}$. Each of the other candidates for the critical isotherm also yields a trial set of T_g, z, and ν.

To obtain the best collapse, the exponents are optimized for what is deemed the most reasonable value of T_g (observing the constraints on the parameters). Then, T_g is varied (within the range determined by the isotherms which show neither upward nor downward curvature) and the parameters are adjusted at each value. The final parameters are taken from what is considered the best scaling plot. Generally, the quality of the scaling deteriorates near the outer limits of possible T_g values. Determining the optimum collapse of the data is a qualitative decision; it is taken as the one which results in the data falling onto one of two well-defined lines with the least deviation. The range of parameters which yield a reasonable collapse of the data is used to estimate the errors in the parameters.

At sufficiently high current densities, one expects flux-flow effects to dominate (see § 1.4). Indeed, at the highest current densities all isotherms show a downward curvature, presumably owing to flux-flow effects, and some cutoff criterion is necessary. For isotherms above the transition, it is clear by inspection where the high-current downward curvature sets in; it corresponds approximately to $\rho \approx J^2$. For isotherms below the transition, it is difficult to distinguish between the high-current flux-flow curvature and the downward curvature expected by the VG model; we generally cut this data less aggressively, using the criterion $\rho J \approx$ constant. Fig. 3.5(a) displays the raw $\rho - J$ for YBCO with a field of 10 mT applied parallel to the c axis, and (b) is

the same data after cutting both the noise at low voltages and the flux-flow curvature at high currents. Fig. 3.6 shows how the NCCO 30 mT data were cut. (The sharp increase in resistivity at high currents seen in a few isotherms in Fig. 3.6(a) results from catastrophic heating effects.)

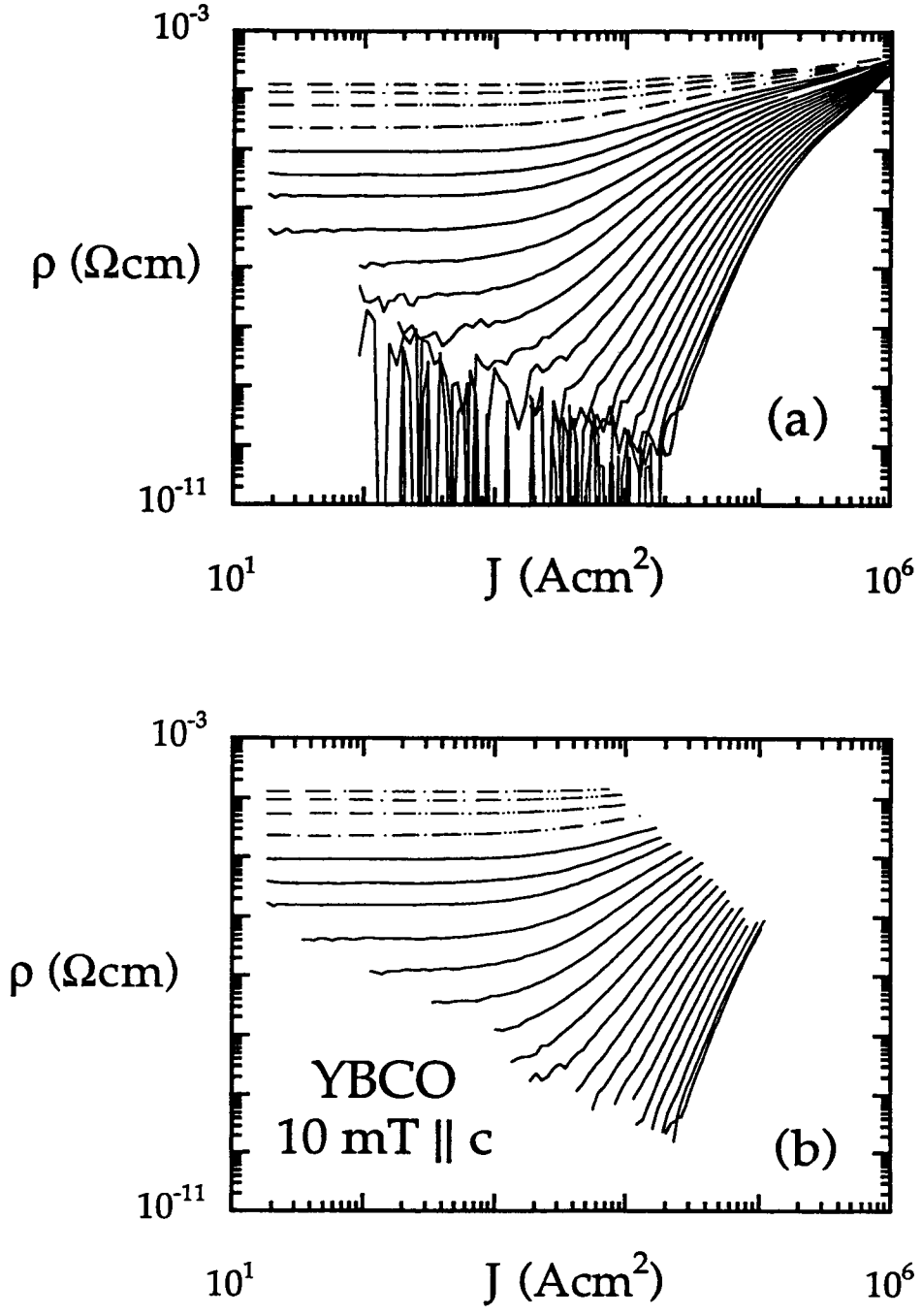

Figure 3.5. ρ-*J* isotherms for YBCO in 10 mT || *c*, before and after being cut. Data are (a) before being cut and (b) after being cut. The isotherms are ~ 0.1 K apart. The dashed isotherms are outside the scaling region. The full temperature range is 85.3 - 87.4 K, with a scaling region of 85.3 - 87.1 K.

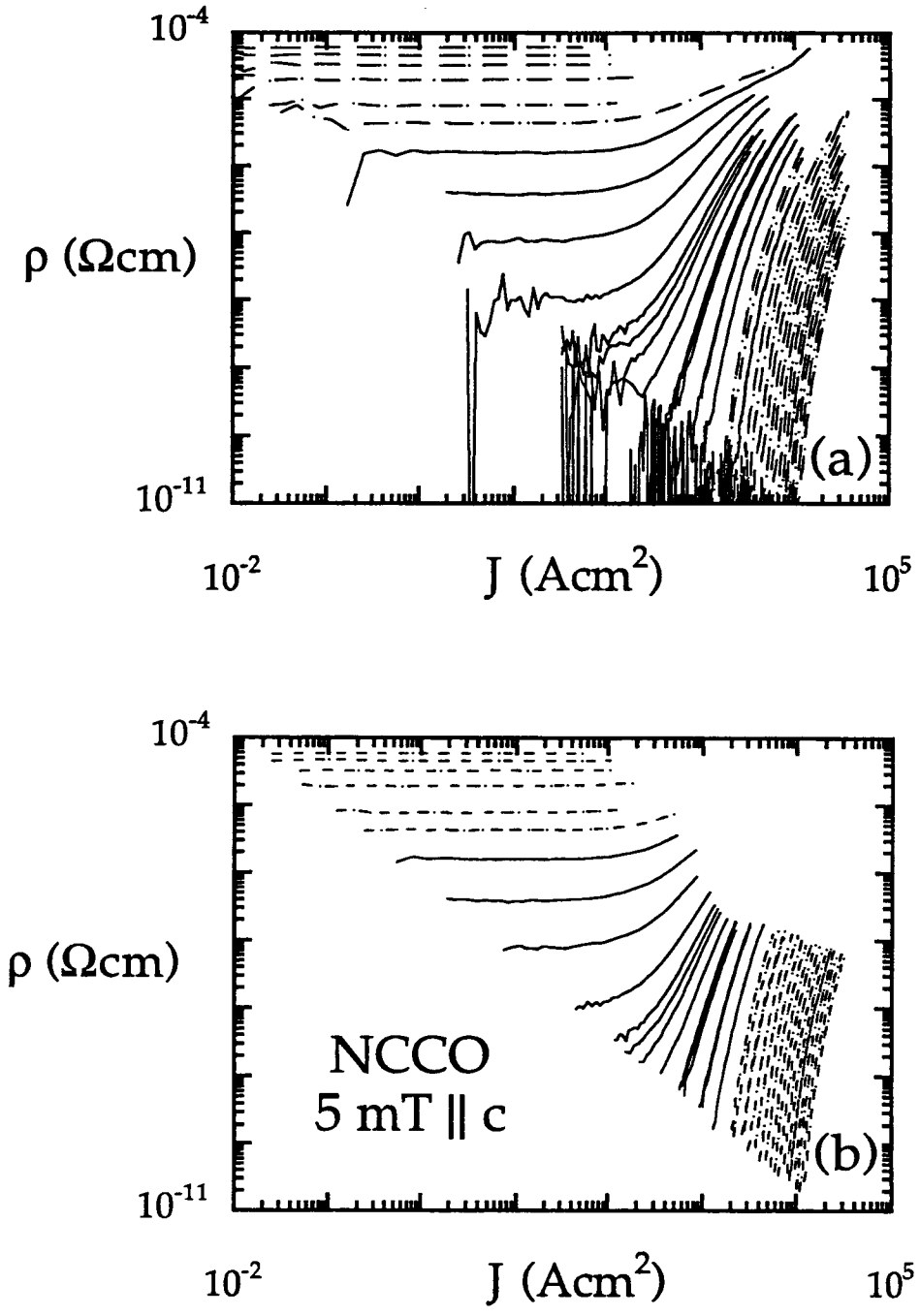

Figure 3.6. ρ-*J* isotherms for NCCO in 5 mT || *c*, before and after being cut. Data are (a) before being cut and (b) after being cut. Data a) before being cut and (b) after being cut. The isotherms are ~ 0.1 K apart. The dashed isotherms are outside the scaling region. The full temperature range is 15.9 - 19.3 K, with a scaling region of 17.8 - 18.6 K.

The universal functions can be divided into four regions, as depicted in Fig. 3.7.

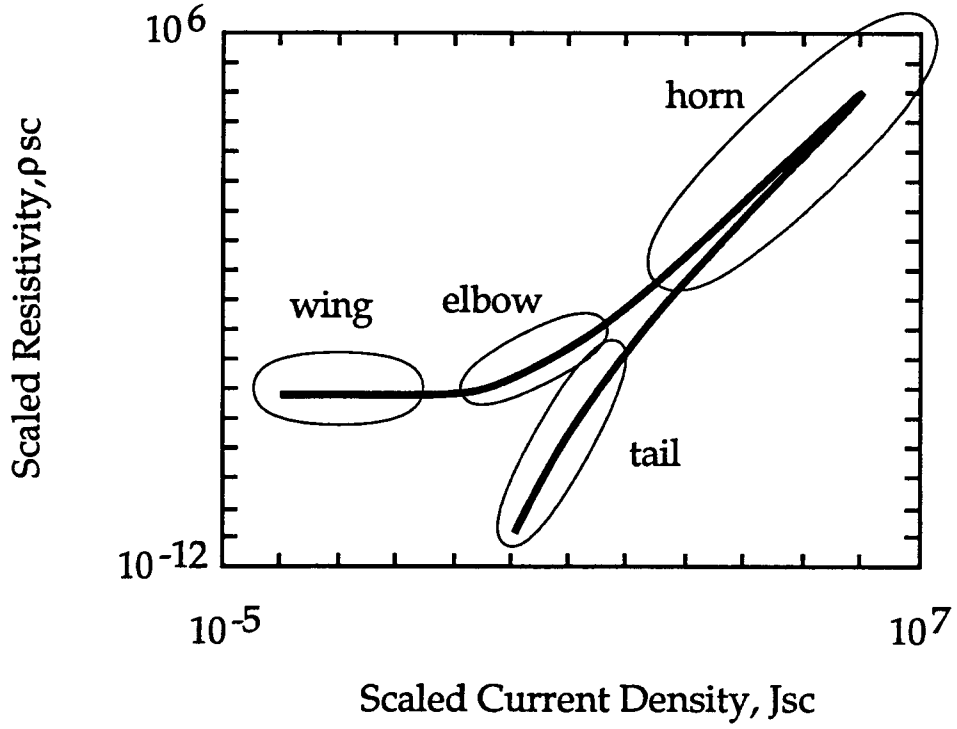

Figure 3.7. Regions of the universal scaling functions $F_{\pm}$. The horn denotes $F_{\pm}$ near T_g, the elbow is the region near $F_+(J_{nl})$, the wing refers to F_+ for $T>>T_g$, and the tail describes F_- for $T<<T_g$. (These functions are for the NCCO film in an applied field of 0.5 T.)

The "horn" denotes $F_{\pm}$ near T_g, the "tail" is F_- away from T_g, the "elbow" describes F_+ near $F_+(J_{nl})$, and the "wing" is where $F_+ \approx 1$, as shown in Fig 3.7. A very poor choice of T_g results in severe deviations at the horn. For example, some isotherms may fall on the wrong function, neither function, or may be shaped like the letter "s". The horn is also quite sensitive

to the choice of z, which is reasonable since z describes the slope of the isotherm at T_g. Another indication that T_g is not correct is if most of the isotherms have odd shapes. A broad elbow in an otherwise nice collapse may signal that ν is wrong. For YBCO, deviations in the tail generally mean that z is incorrect, and deviations in the wing usually signify that ν has not been optimized; for NCCO, both exponents affect the wing and tail.

Fig. 3.8 displays the scaling collapse of the data appearing in Figs. 3.5 and 3.6, for the YBCO film in 10 mT $\| c$, and the NCCO film in 5 mT $\| c$, respectively. Figs. 3.9-3.25 show the ρ-J isotherms and scaling collapse for both films and all fields (except 0 T). The quality of the scaling has improved as our technique has, resulting in good, though not optimal, scaling for the earliest data. However, all of the scaling collapses presented here are comparable to most of the published data (see references in Table 1.2). The primary source of diminished scaling quality results from leaving too much of the high-current data (that which shows the effects of flux flow [see § 1.4 and 3.7)].

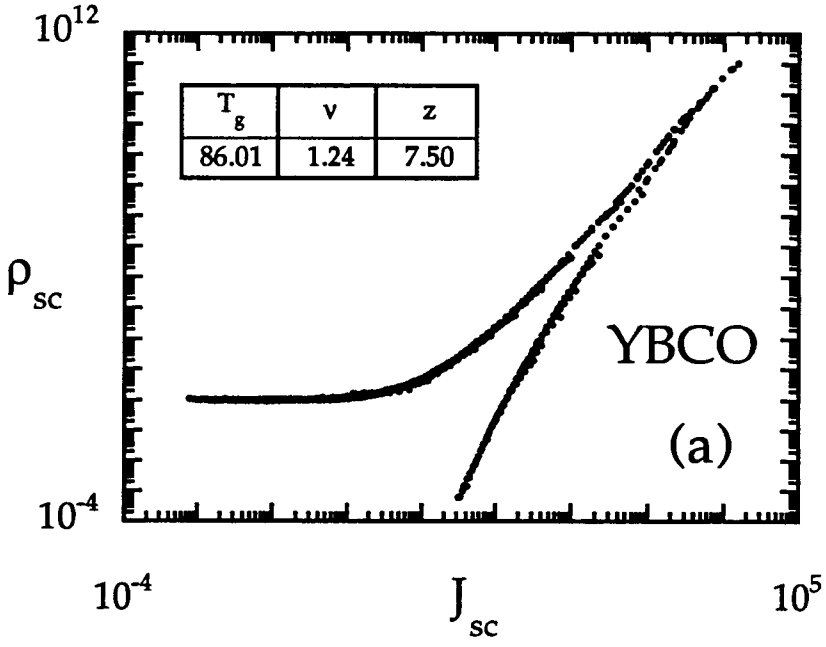

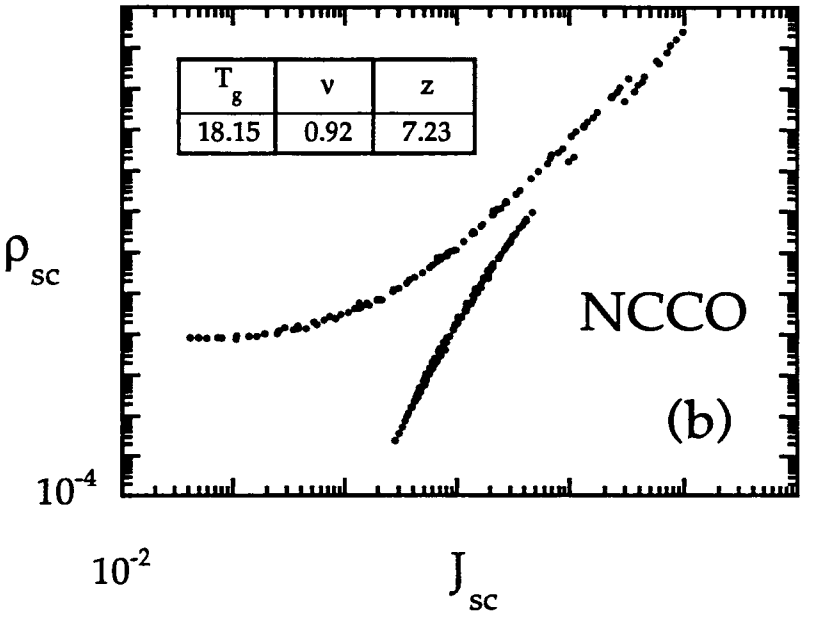

Figure 3.8. Scaling collapse for (a) YBCO with 10 mT ∥ *c*, and (b) NCCO with 5 mT ∥ *c*.

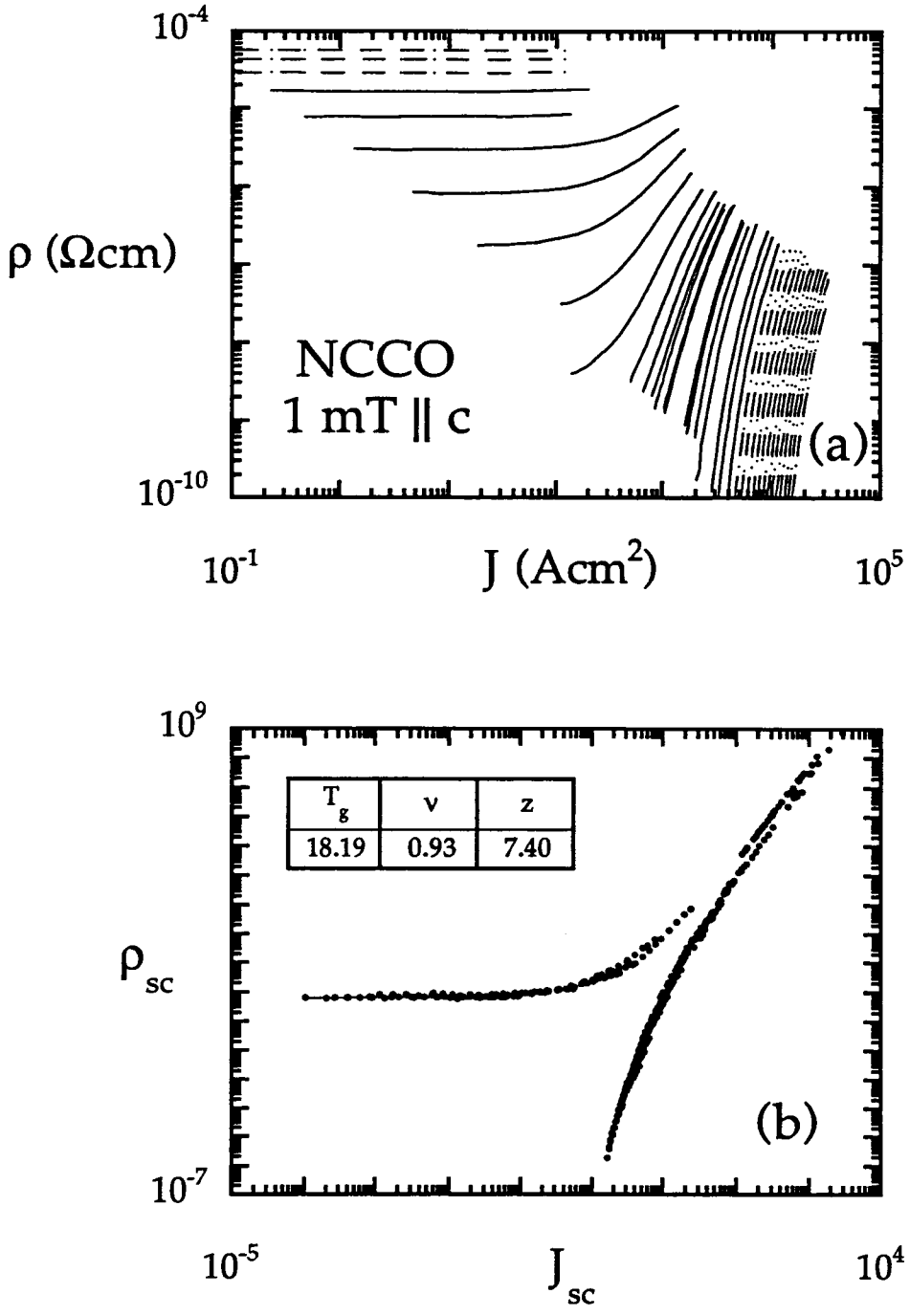

Figure 3.9. *ρ-J* isotherms and scaling collapse for NCCO with 1 mT ‖ *c*. (a) Resistivity-current density isotherms. The dashed isotherms are outside the scaling region. Data in (a) collapsed onto the two universal functions according to Eq. 2.2.

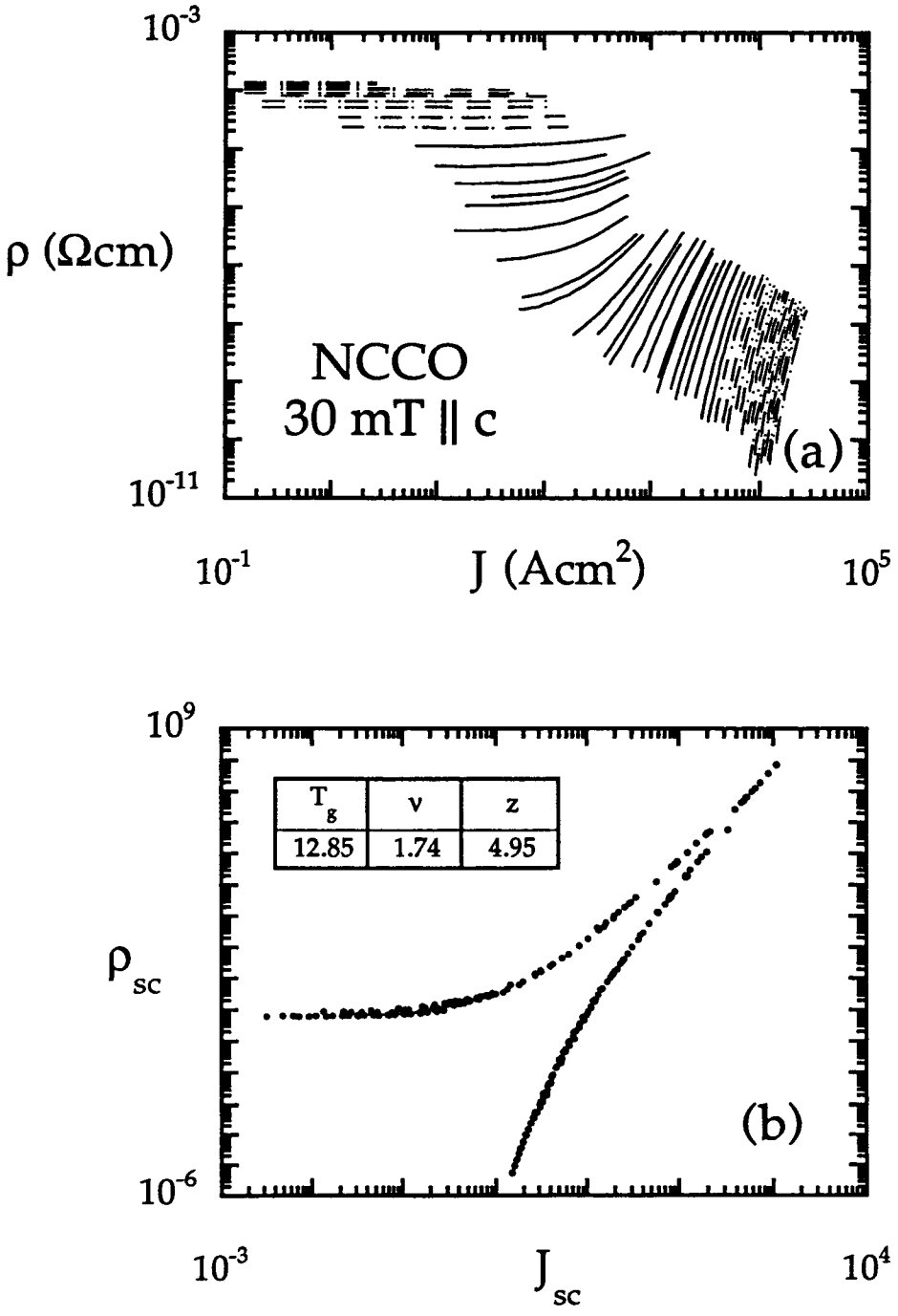

Figure 3.10. ρ-J isotherms and scaling collapse for NCCO with 30 mT $\|$ c. (a) Resistivity-current density isotherms. The dashed isotherms are outside the scaling region. The temperature range is 15.14 - 19.90 K. (b) Data in (a) collapsed onto the two universal functions according to Eq. 2.2.

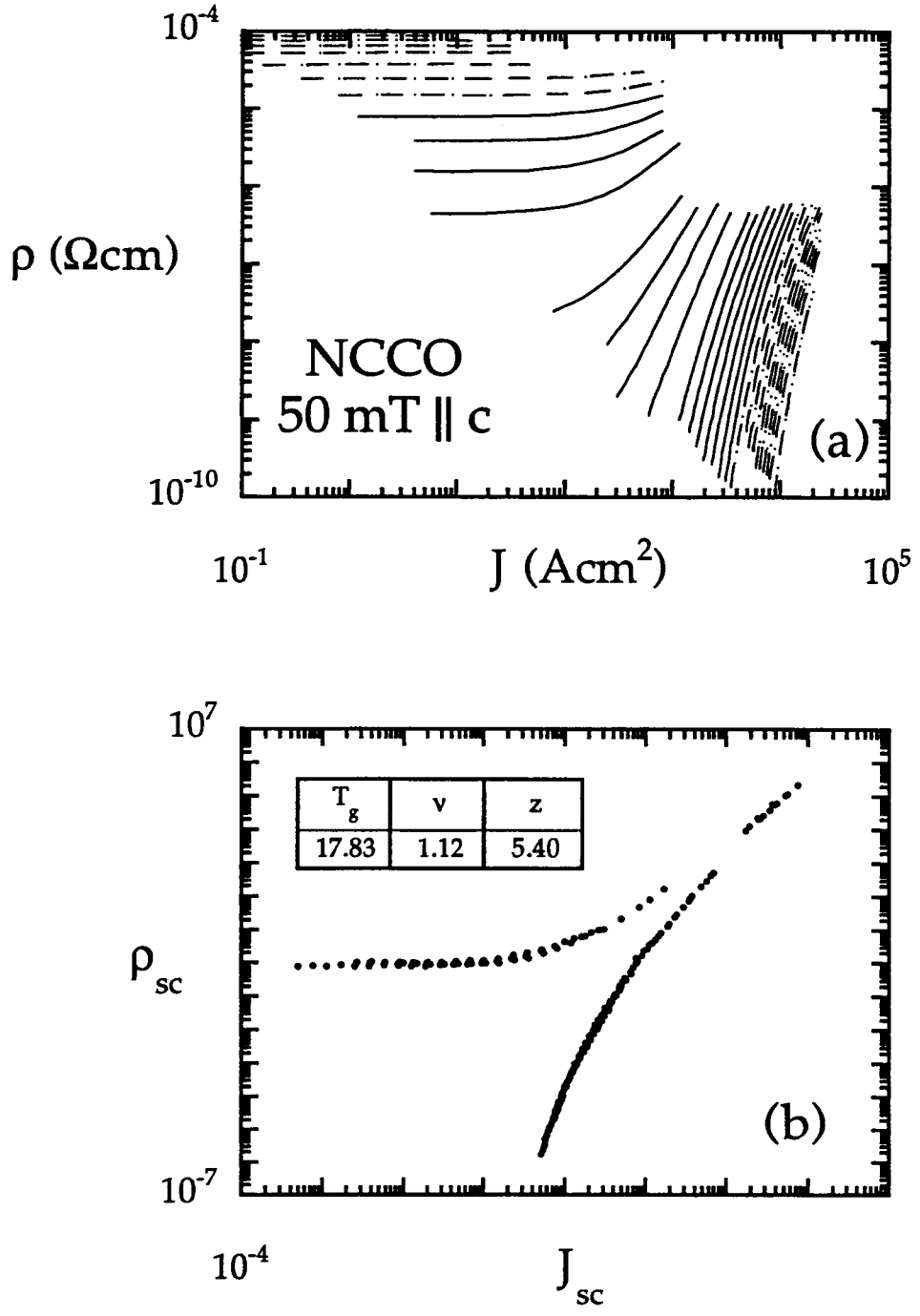

Figure 3.11. *ρ-J* isotherms and scaling collapse for NCCO with 50 mT || *c*. (a) Resistivity-current density isotherms. The dashed isotherms are outside the scaling region. (b) Data in (a) collapsed onto the two universal functions according to Eq. 2.2.

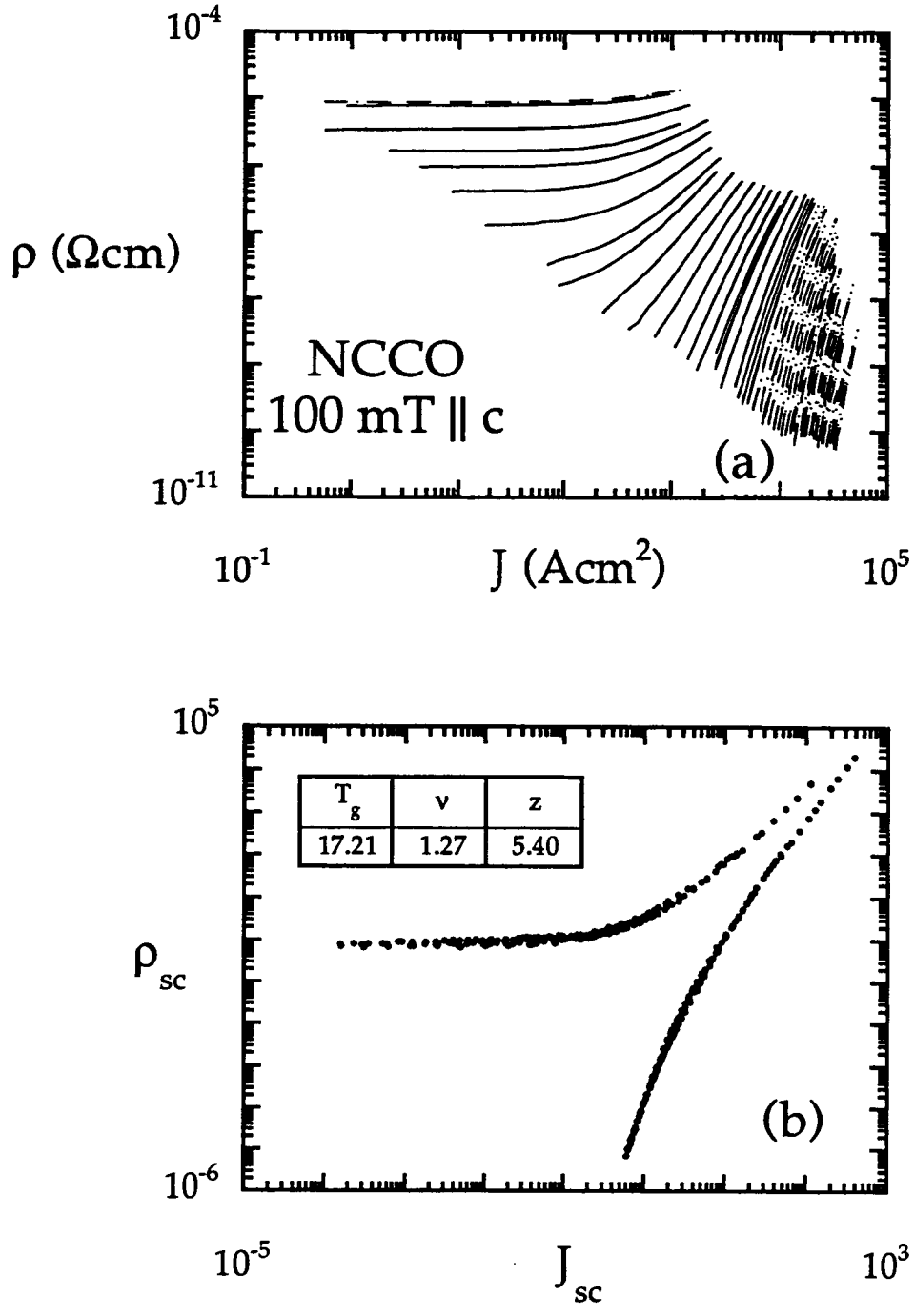

Figure 3.12. *ρ-J* isotherms and scaling collapse for NCCO with 100 mT ‖ *c*. (a) Resistivity-current density isotherms. The dashed isotherms are outside the scaling region. (b) Data in (a) collapsed onto the two universal functions according to Eq. 2.2.

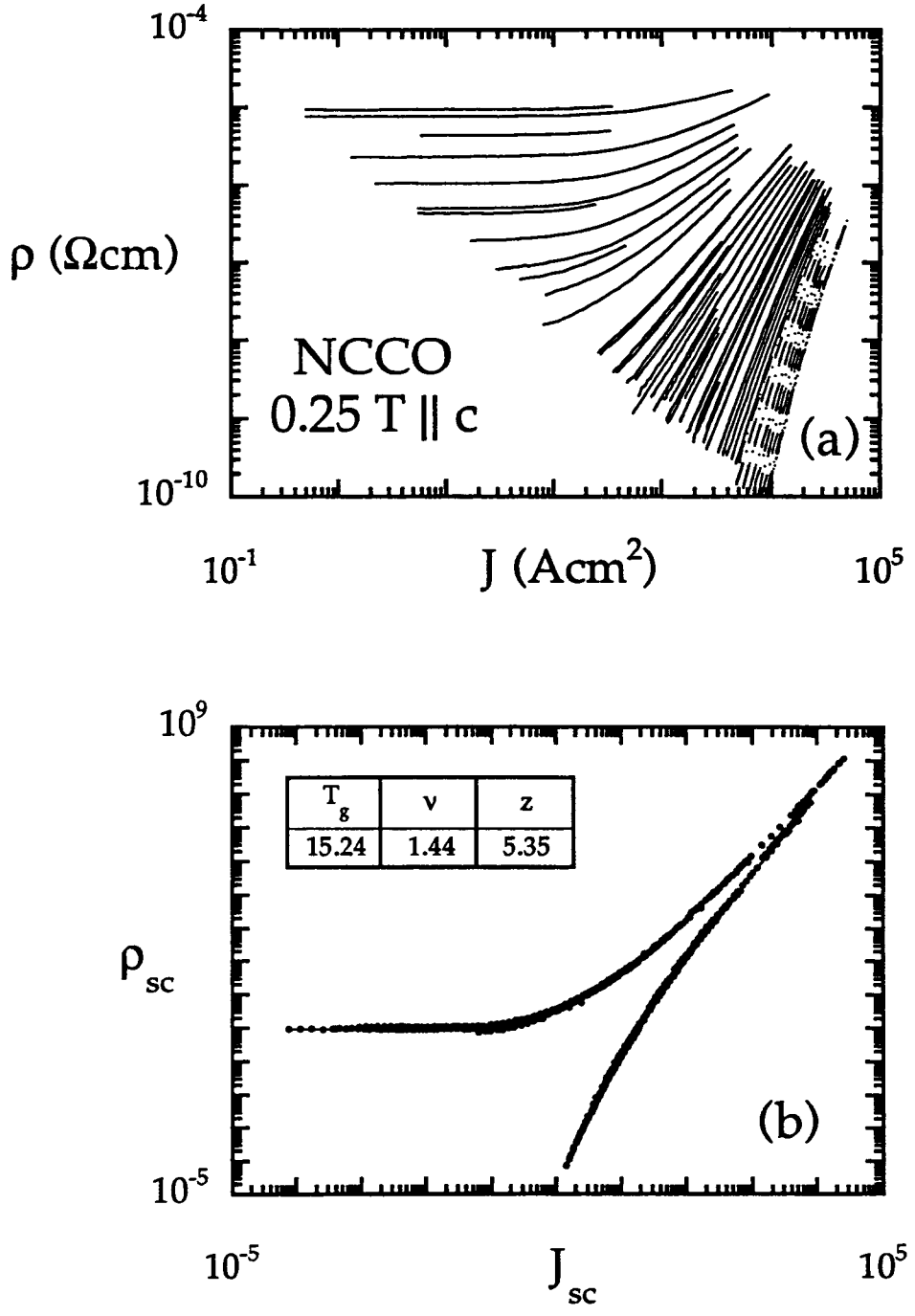

Figure 3.13. ρ-J isotherms and scaling collapse for NCCO with 0.25 T $\|$ c. (a) Resistivity-current density isotherms. The dashed isotherms are outside the scaling region. (b) Data in (a) collapsed onto the two universal functions according to Eq. 2.2.

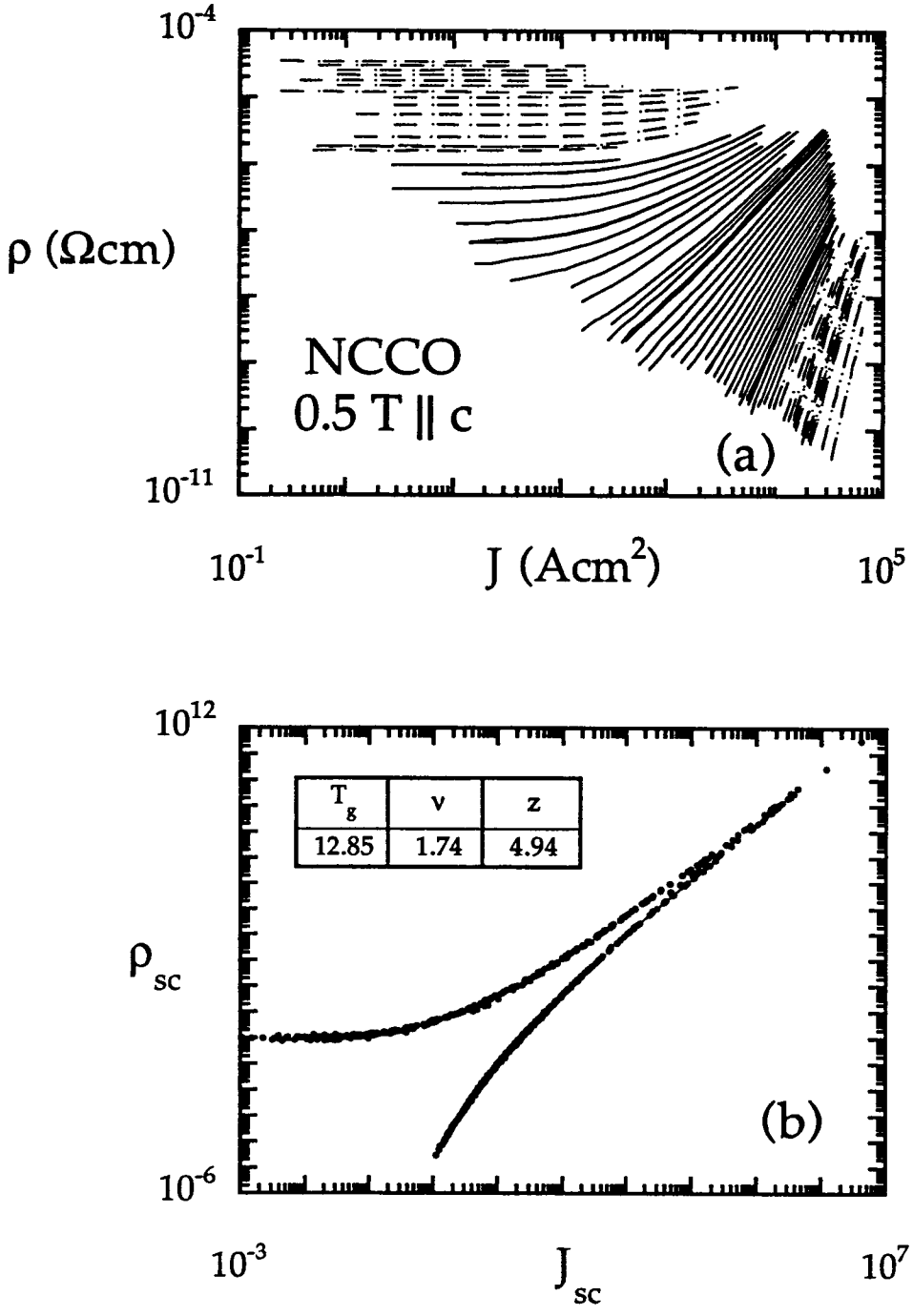

Figure 3.14. *ρ-J* isotherms and scaling collapse for NCCO with 0.5 T || *c*. (a) Resistivity-current density isotherms. The dashed isotherms are outside the scaling region. (b) Data in (a) collapsed onto the two universal functions according to Eq. 2.2.

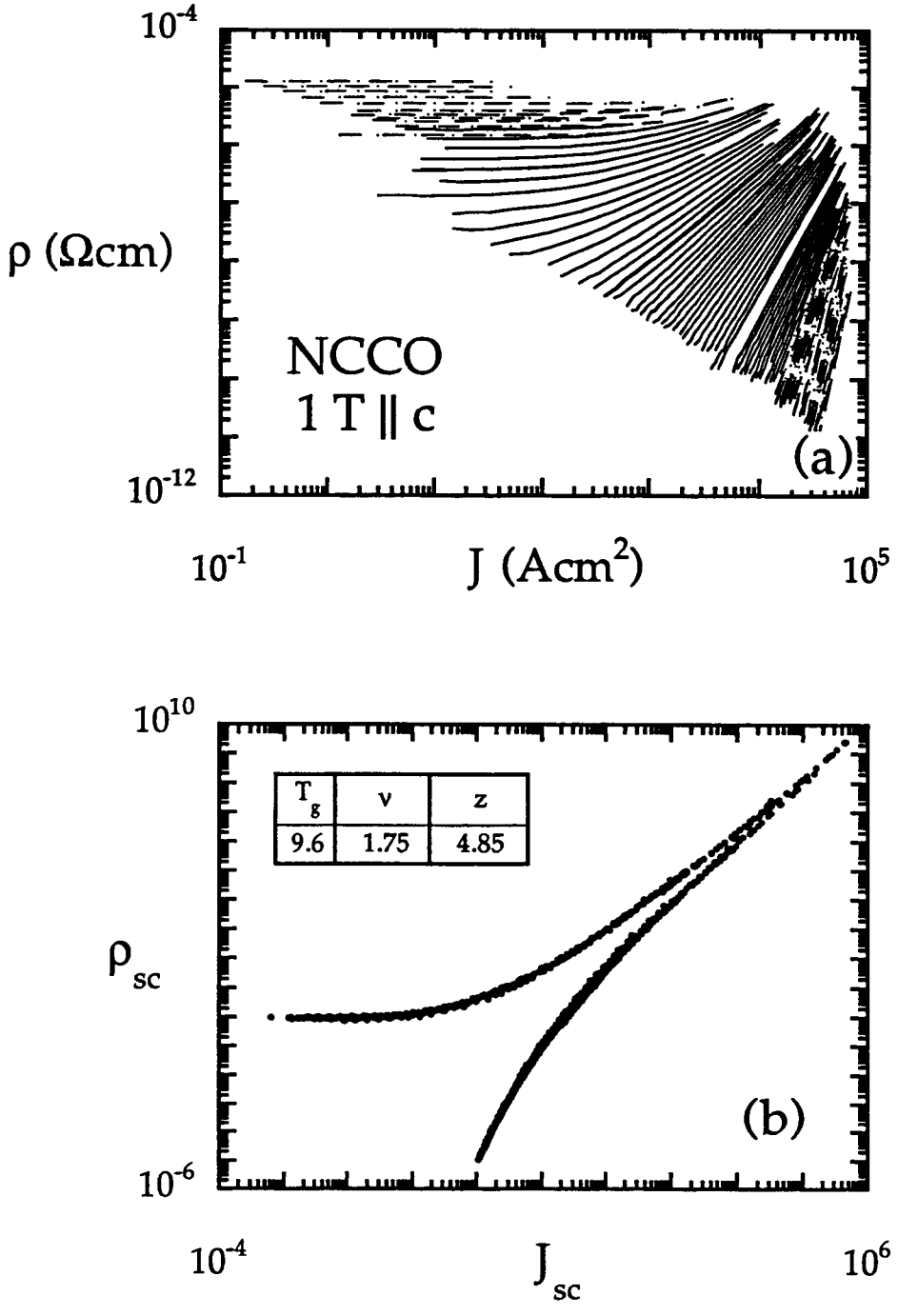

Figure 3.15. *ρ-J* isotherms and scaling collapse for NCCO with 1 T || *c*. (a) Resistivity-current density isotherms. The dashed isotherms are outside the scaling region. (b) Data in (a) collapsed onto the two universal functions according to Eq. 2.2.

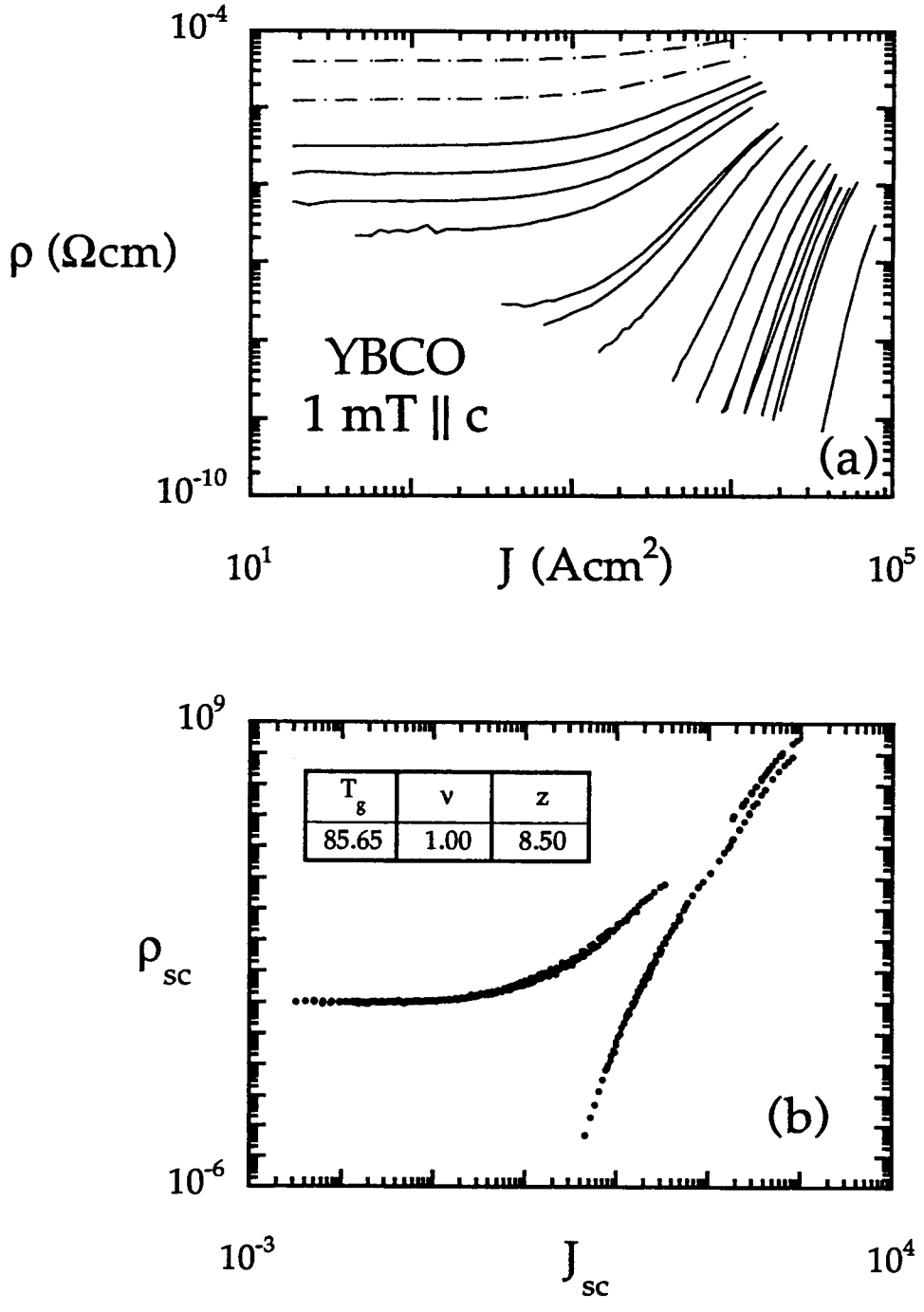

Figure 3.16. *ρ-J* isotherms and scaling collapse for YBCO with 1 mT || *c*. (a) Resistivity-current density isotherms. The dashed isotherms are outside the scaling region. (b) Data in (a) collapsed onto the two universal functions according to Eq. 2.2.

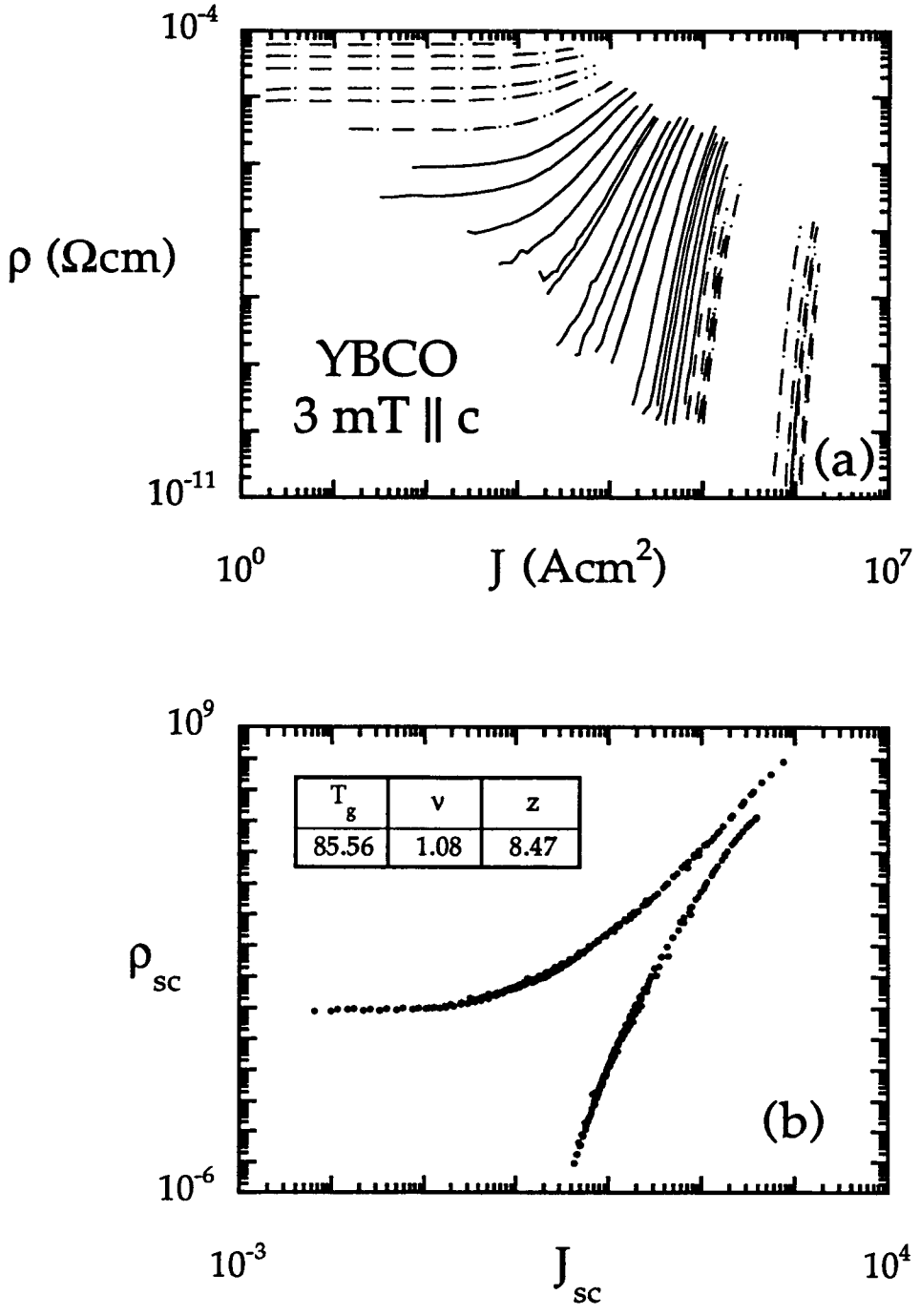

Figure 3.17. *ρ-J* isotherms and scaling collapse for YBCO with 3 mT || *c*. (a) Resistivity-current density isotherms. The dashed isotherms are outside the scaling region. (b) Data in (a) collapsed onto the two universal functions according to Eq. 2.2.

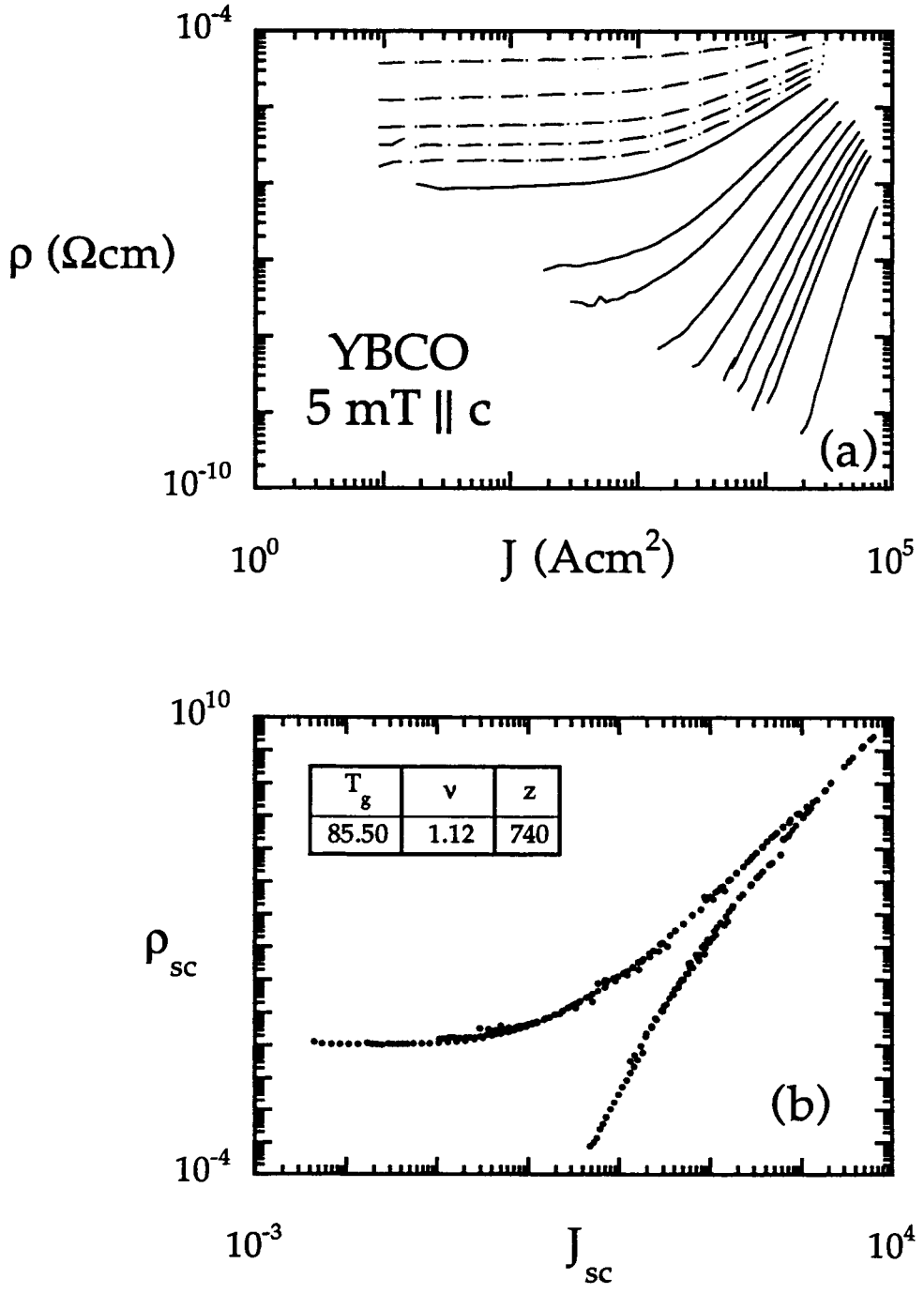

Figure 3.18. ρ-J isotherms and scaling collapse for YBCO with 5 mT || c. (a) Resistivity-current density isotherms. The dashed isotherms are outside the scaling region. (b) Data in (a) collapsed onto the two universal functions according to Eq. 2.2.

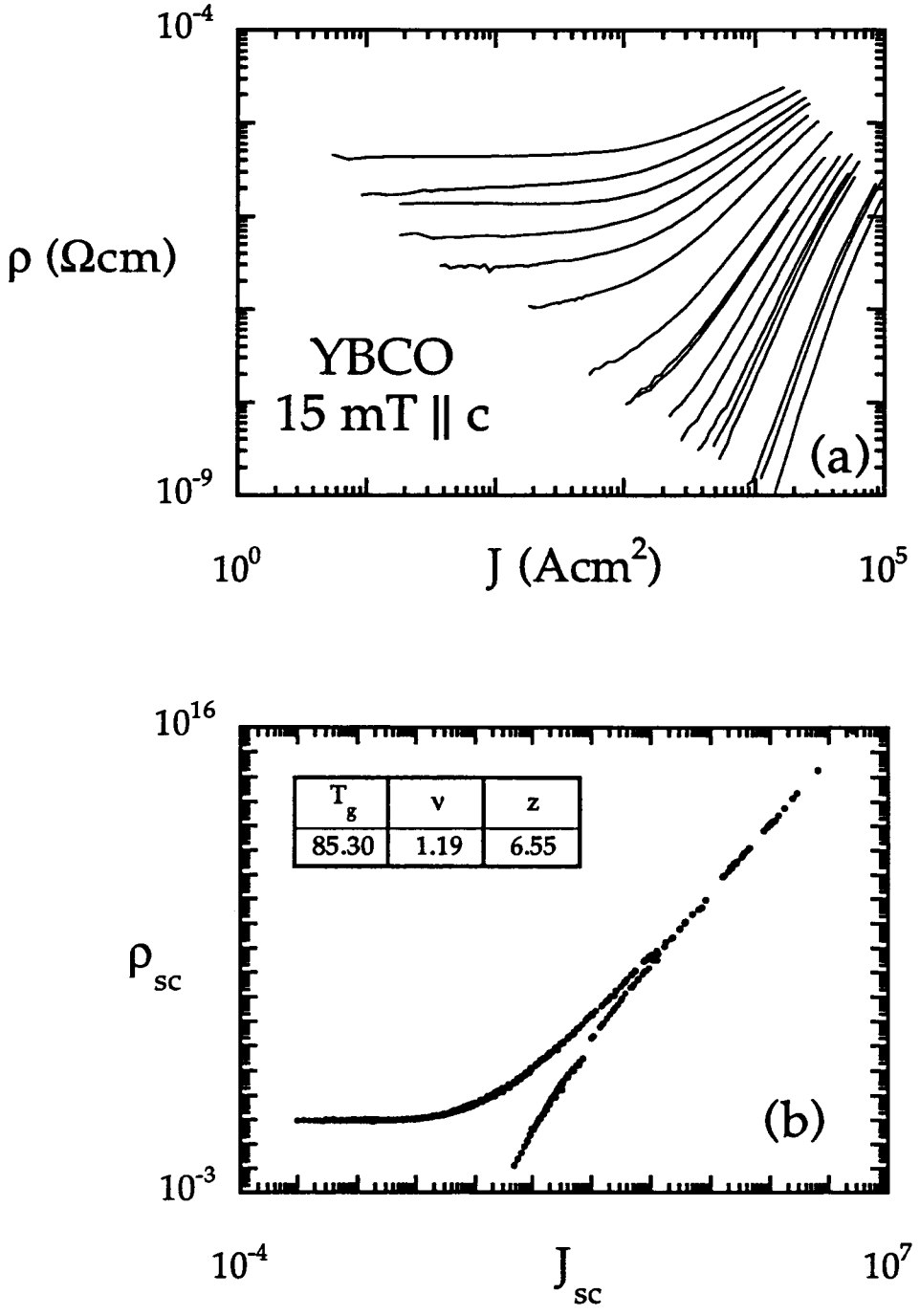

Figure 3.19. ρ-J isotherms and scaling collapse for YBCO with 15 mT $\|$ c. (a) Resistivity-current density isotherms. The dashed isotherms are outside the scaling region. (b) Data in (a) collapsed onto the two universal functions according to Eq. 2.2.

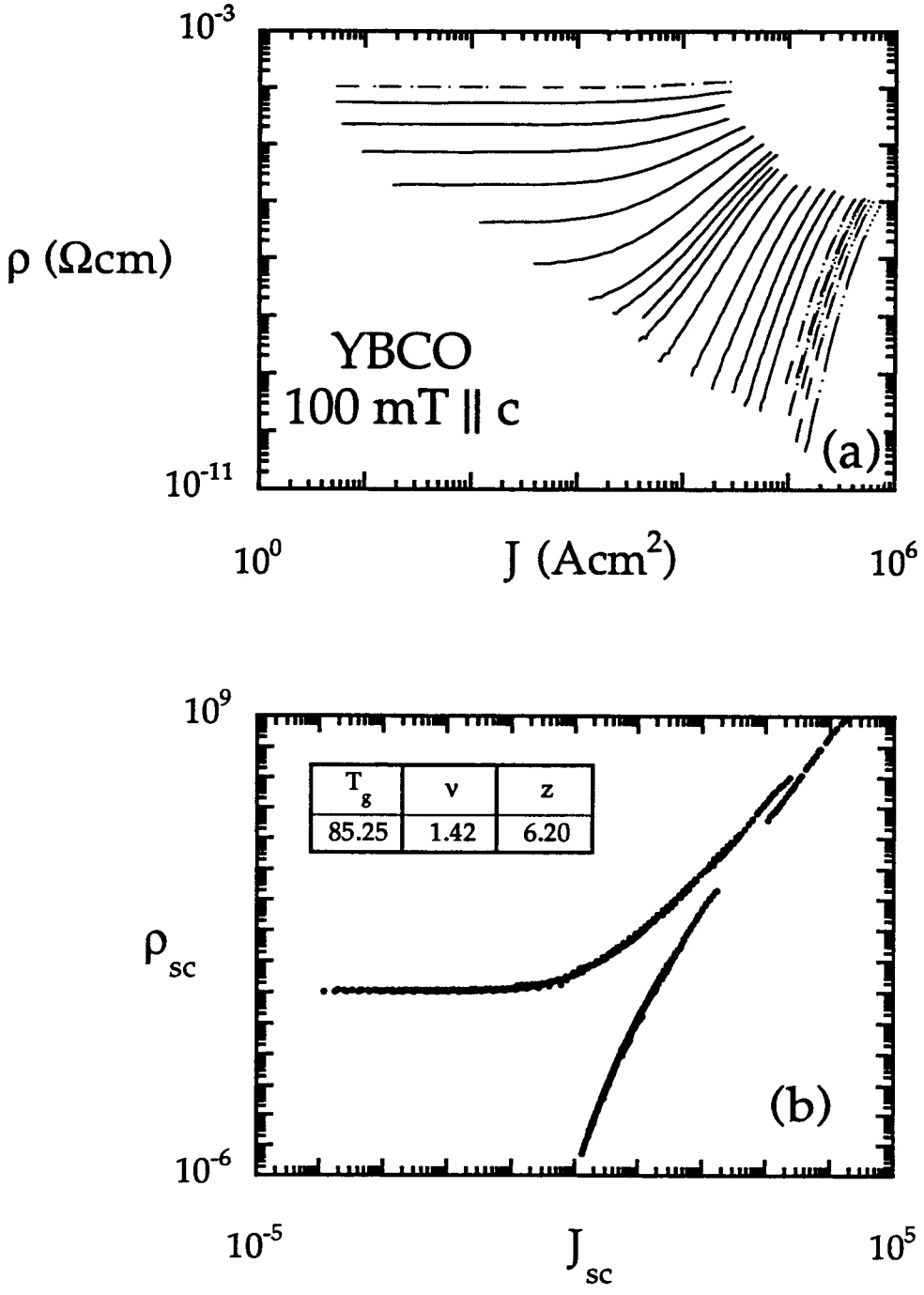

Figure 3.20. *ρ-J* isotherms and scaling collapse for YBCO with 100 mT || *c*. (a) Resistivity-current density isotherms. The dashed isotherms are outside the scaling region. (b) Data in (a) collapsed onto the two universal functions according to Eq. 2.2.

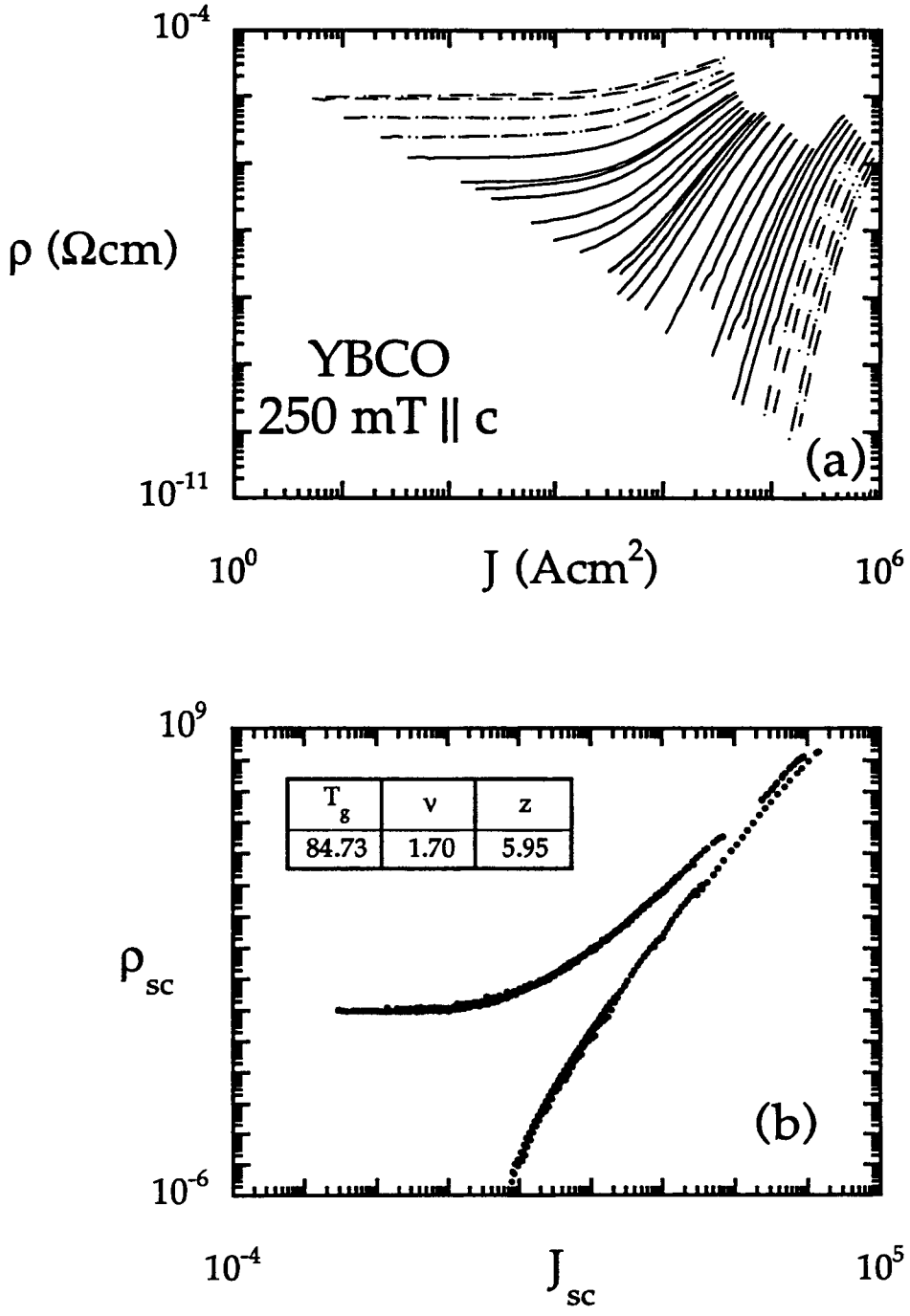

Figure 3.21. ρ-J isotherms and scaling collapse for YBCO with 0.25 T $\|$ c. (a) Resistivity-current density isotherms. The dashed isotherms are outside the scaling region. (b) Data in (a) collapsed onto the two universal functions according to Eq. 2.2.

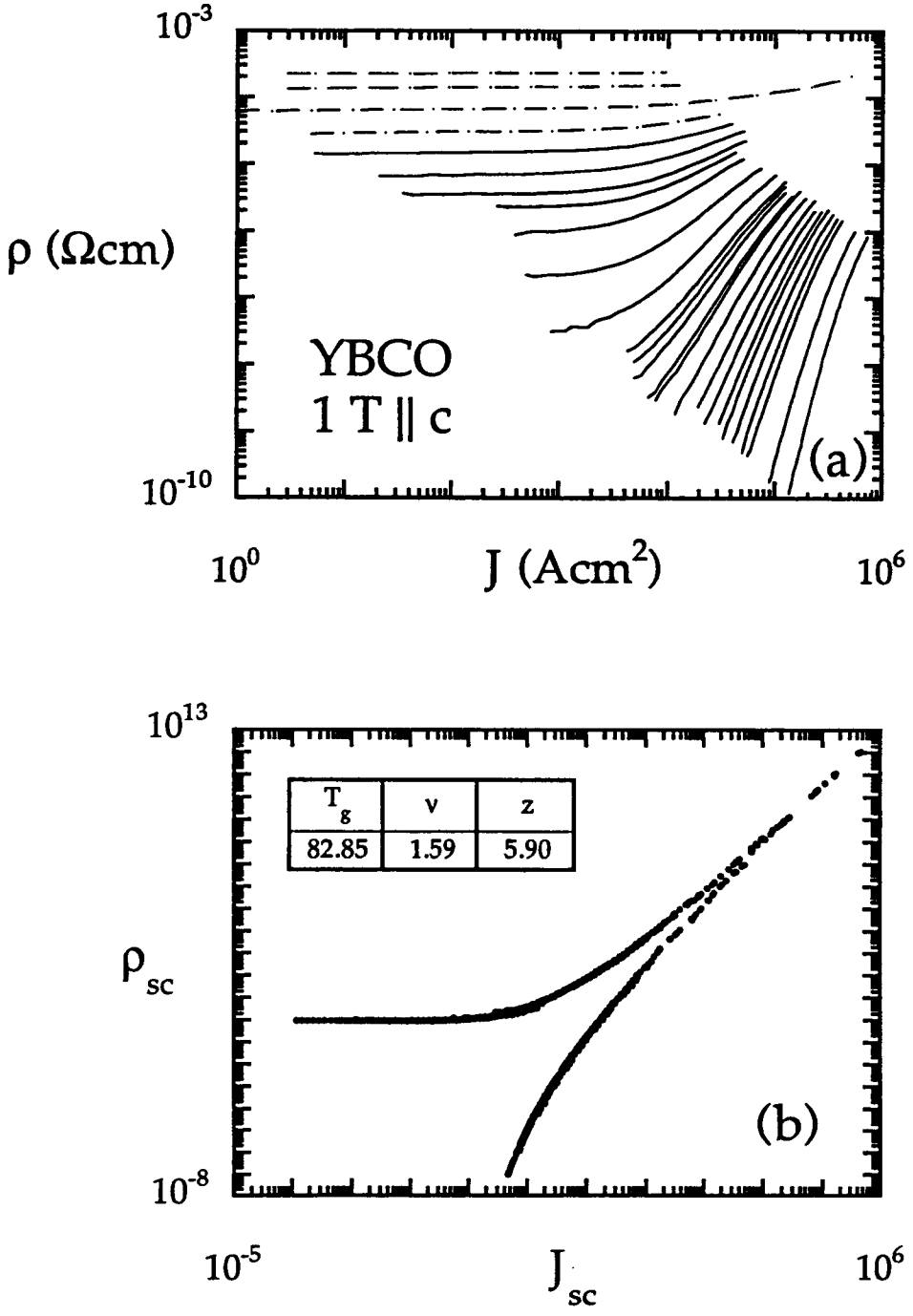

Figure 3.22. ρ-J isotherms and scaling collapse for YBCO with 1 T $\|$ c. (a) Resistivity-current density isotherms. The dashed isotherms are outside the scaling region. (b) Data in (a) collapsed onto the two universal functions according to Eq. 2.2.

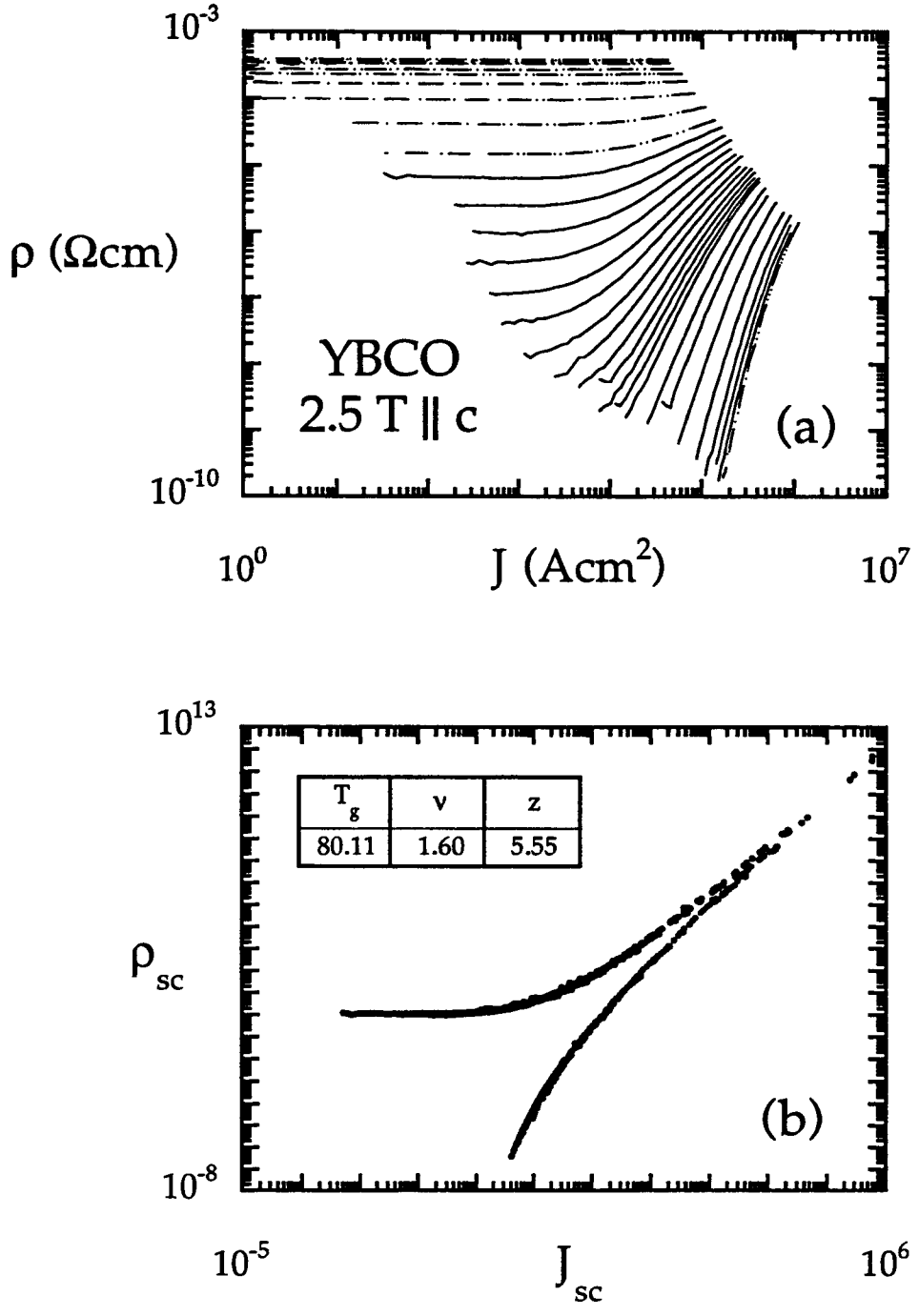

Figure 3.23. *ρ-J* isotherms and scaling collapse for YBCO with 2.5 T || *c*. (a) Resistivity-current density isotherms. The dashed isotherms are outside the scaling region. (b) Data in (a) collapsed onto the two universal functions according to Eq. 2.2.

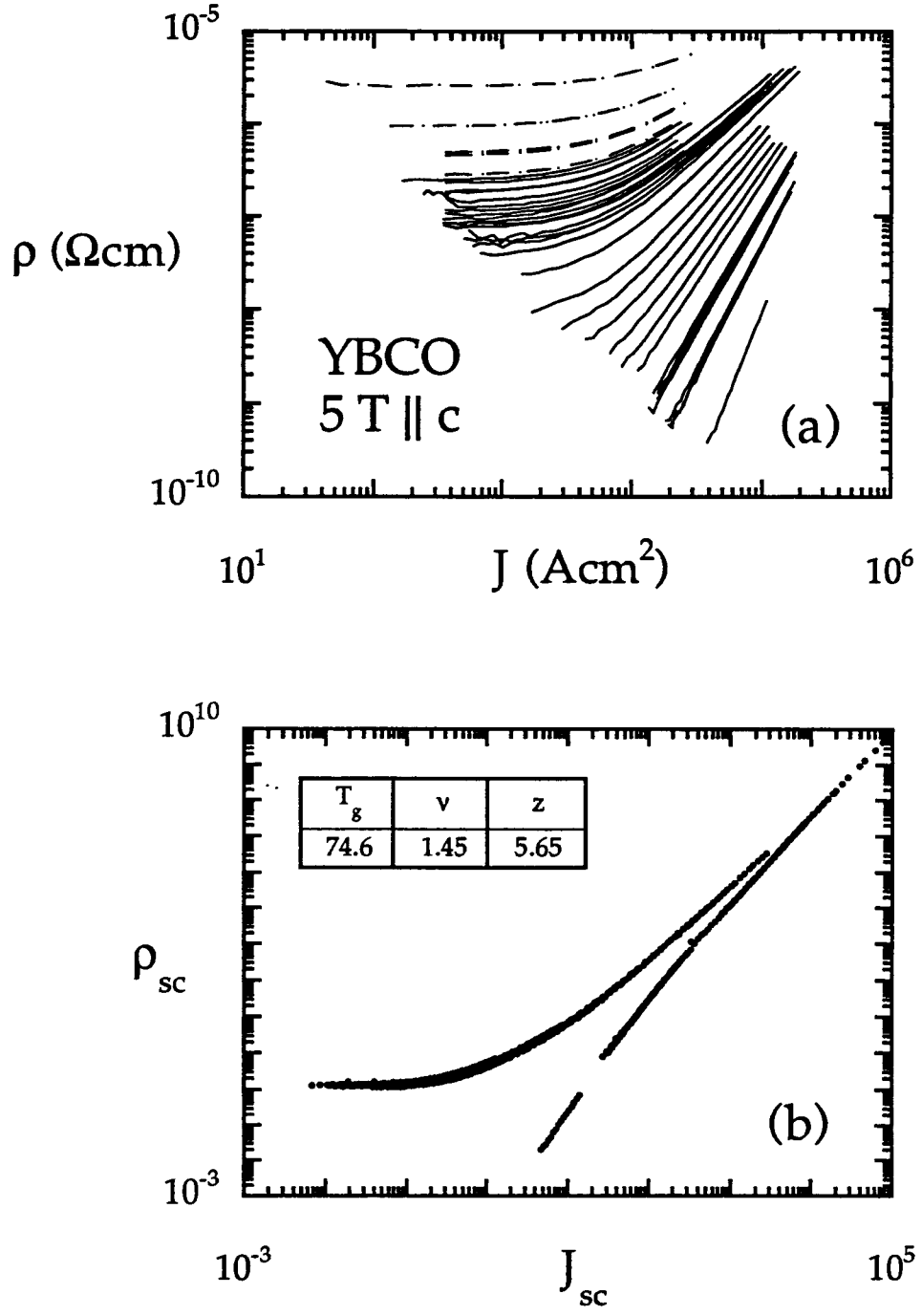

Figure 3.24. ρ-J isotherms and scaling collapse for YBCO with 5 T || c. (a) Resistivity-current density isotherms. The dashed isotherms are outside the scaling region. (b) Data in (a) collapsed onto the two universal functions according to Eq. 2.2.

CHAPTER 4
RESULTS

Dc $\rho - J$ isotherms were measured for the NCCO film in applied magnetic fields from 1 mT - 1 T, and for the YBCO film in fields from 1 mT - 5 T, including some in the milliTesla range for each film. It was found that the $\rho - J$ isotherms for both films and all fields measured scale according to Eq. 2.2[7]. At high fields the critical exponents extracted are the same, constant, and consistent with the vortex glass theory. The universal scaling functions found at high fields are indeed universal, as seen in Fig. 4.1 which is the overlay of the universal functions obtained for two different YBCO films in an applied field of 5 T; one set of scaling functions was obtained by Wöltgens *et al.* (1993) and one was obtained by us. At low fields we see a change in both the critical exponents and the scaling functions.

4.1 Field Dependence of the Critical Exponents

Fig. 4.2 displays the field dependence of the critical exponents for both films. Tables 4.1 and 4.2 list the exponents, including z from the slope of the critical isotherm and s from the fitting the ρ_{lin} data. Tables 4.3 and 4.4 list the uncertainties in the exponents. For high fields, the extracted exponents are

---

7 We also scaled ρ-J data for ambient field for both films. We did not measure any values of ρ_{lin} with a power-law dependence on $|T-T_g|$. Because of this, it is uncertain if any of the ambient field data lie within the scaling regime. Some of the measured isotherms could be within the scaling regime but with a linear resistance which is below our measurement resolution. For the NCCO film we find a reasonable collapse of the data within a region of 0.6 K around T_g using the parameters T_g=18.17±0.03 K, z=10.4±0.005, and ν=1.04±0.005. For the YBCO film, we used T_g=85.80 K, z=8.8, and ν=1.03.

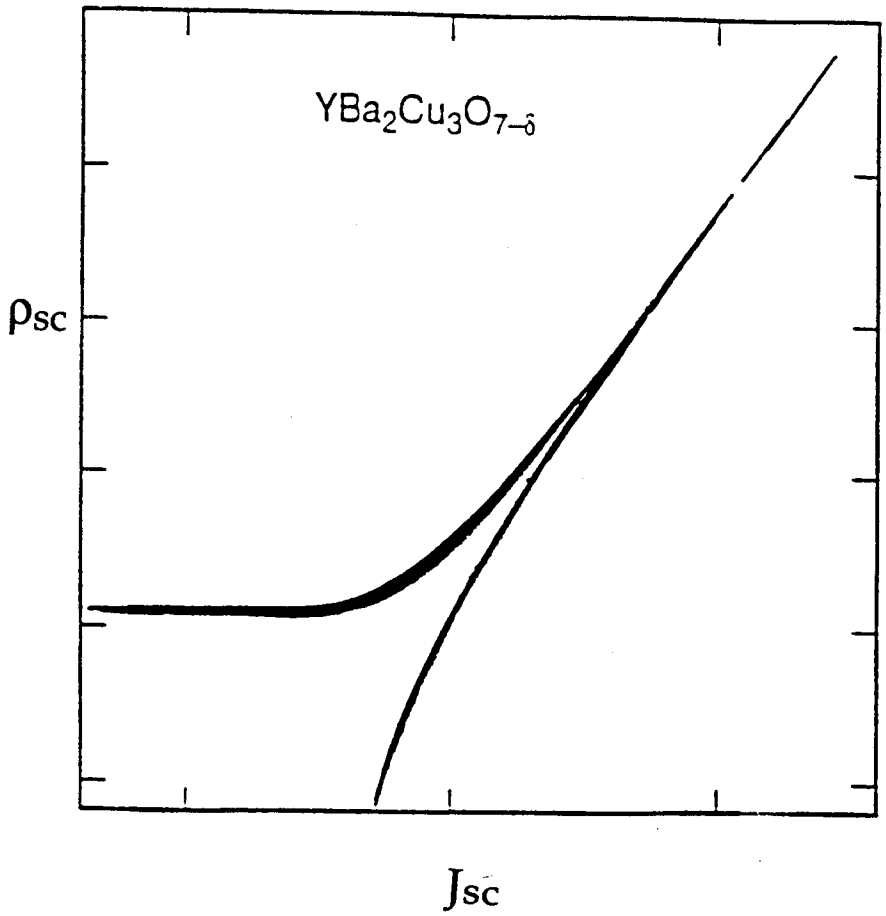

Figure 4.1. Comparison of the universal functions for two YBCO films. The figure shows both the data from Wöltgens *et al.* (1993) Fig. 3, and the data presented in this thesis. The films have 5 T $\parallel c$.

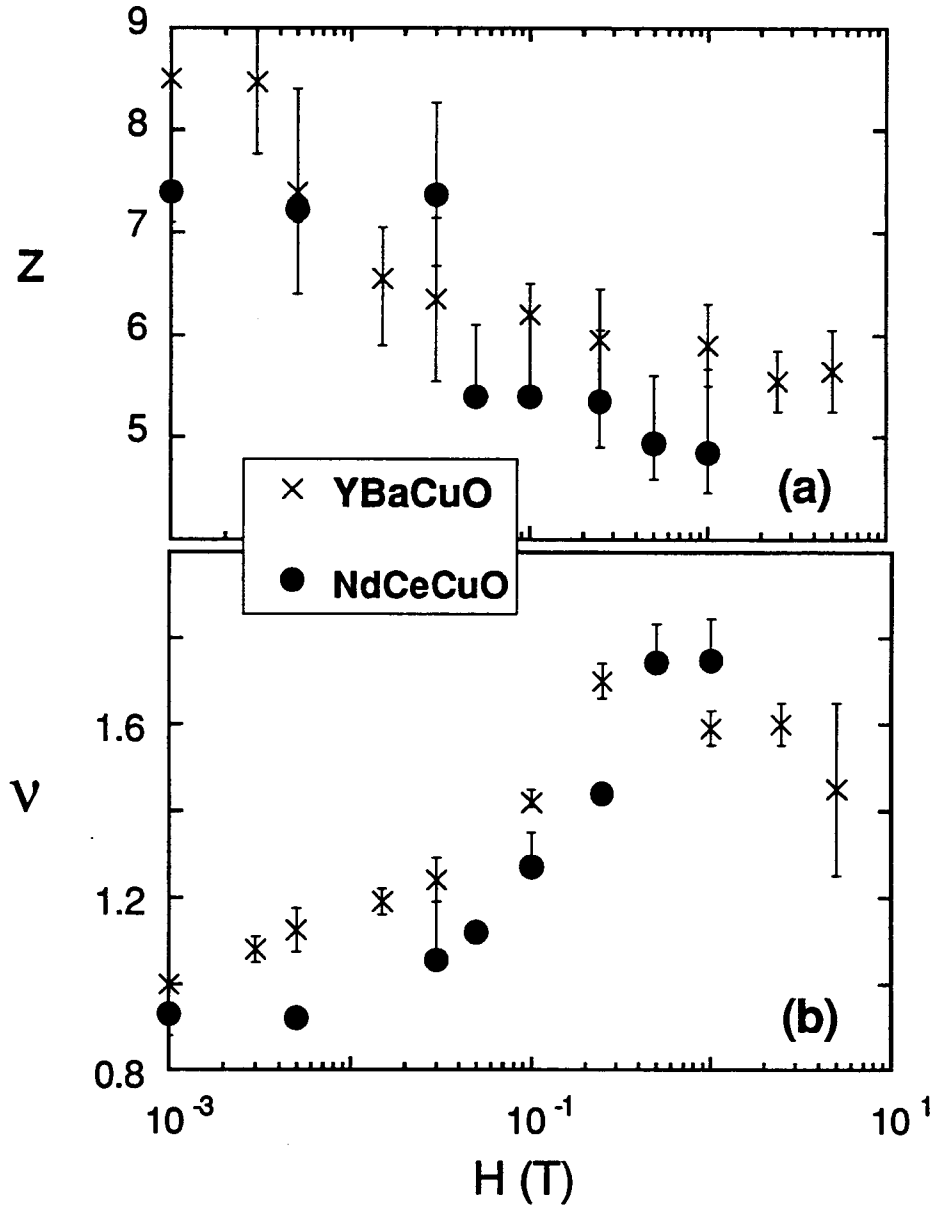

Figure 4.2. Dynamic and static exponents as a function of field. (a) shows z and (b) ν. Crosses are the values for the YBCO film, and the circles are for the NCCO film. The uncertainty in T_g is the primary source of the error in the exponents; once T_g has been specified, the uncertainty becomes much smaller.

$z \cong 5.6 \pm 0.5$ and $\nu \cong 1.5 \pm 0.2$. As the field is decreased, z increases and ν decreases. At the lowest fields (below 30 mT), z and ν become constant again with $\nu \cong 1$, $z \cong 7.3$ (for NCCO) and $z \cong 8.5$ (for YBCO). Though the exponents for YBCO and NCCO are the same within error, the average low-field value for z is higher for YBCO than for NCCO. The values for the exponents are presented in Tables 4.1 and 4.2.

We find that s resulting from fitting the ρ_{lin} data to $\rho_{lin} = \rho_o \left| 1 - \frac{T}{T_g} \right|^s$ is consistent with s calculated using ν and z from scaling $s \equiv \nu(z-1)$ (recall Eq. 2.9), as shown in Tables 4.1 and 4.2. We obtain $s \cong 7 \pm 1.5$ for both films, with considerable scatter but without systematic field dependence.

Table 4.1. Critical exponents for NCCO obtained using different methods. The values which gave the best data collapse are denoted z_{sc} and ν_{sc}. The dynamic exponent z from $\rho \propto J^{\frac{z-1}{2}}$ at T_g is labeled 'z $\rho(J)@T_g$'. The combination $s = \nu(z-1)$ from $\rho_{lin} \propto |T-T_g|^s$ is denoted s. The percent difference between these values and those used in the scaling collapse are listed.

H (T)	ν_{sc}	z_{sc}	z $\rho(J)@T_g$	% diff.	$\nu_{sc}(z_{sc}-1)$	s	% diff.
1	1.8	4.9	5.0	3	6.7	6.9	2
0.5	1.7	4.9	5.0	1	6.9	6.8	1
0.25	1.4	5.4	5.3	1	6.3	6.2	1
0.1	1.3	5.4	5.4	0	5.6	5.1	9
0.05	1.1	5.4	5.3	2	4.9	4.5	9
0.03	1.1	7.4	7.6	3	6.7	5.5	20
0.005	0.9	7.2	7.1	2	5.7	5.2	10
0.001	0.9	7.4	8.2	10	6.0	5.5	8

Table 4.2. Critical exponents for YBCO obtained using different methods.

H (T)	ν_{sc}	z_{sc}	z $\rho(J)@T_g$	% diff.	$\nu_{sc}(z_{sc}-1)$	s	% diff.
5	1.5	5.6	5.7	0.2	6.7	6.9	3
2.5	1.6	5.5	5.8	3	7.3	7.4	2
1	1.6	5.9	5.7	3	7.8	7.7	1
0.25	1.7	6.0	6.7	12	8.4	6.8	21
0.1	1.4	6.2	6.7	8	7.4	7.4	1
0.03	1.2	6.4	6.4	1	6.6	6.7	1
0.015	1.2	6.5	6.7	1	6.6	6.8	3
0.010	1.2	7.5	8.0	7	8.1	8.1	0.1
0.005	1.1	7.4	7.1	4	7.2	6.9	3
0.003	1.1	8.5	8.6	2	8.1	8.2	3
0.001	1.0	8.5	9.7	13	7.5	7.5	0.1

Table 4.3. Summary of scaling exponents for the NCCO film. These values were obtained by optimizing the scaling collapse. The upper uncertainty in ν is denoted as $\delta\nu_+$ and the lower as $\delta\nu_-$; similarly, the uncertainties in z are δz_+ and δz_-.

H (T)	ν_{sc}	$\delta\nu_+$	$\delta\nu_-$	z_{sc}	δz_+	δz_-
1	1.75	0.10	0.01	4.85	0.8	0.4
0.5	1.74	0.09	0.02	4.94	0.7	0.4
0.25	1.44	0.01	0.00	5.35	0.7	0.5
0.1	1.27	0.08	0.02	5.40	0.1	0.1
0.05	1.12	0.01	0.02	5.40	0.7	0.0
0.03	1.05	0.14	0.03	7.37	1.5	1.4
0.005	0.92	0.01	0.01	7.23	0.1	0.1
0.001	0.93	0.01	0.05	7.40	0.6	0.3

Table 4.4. Summary of scaling exponents for the YBCO film. These values were obtained by optimizing the scaling collapse. The upper uncertainty in ν is denoted as $\delta\nu_+$ and the lower as $\delta\nu_-$; similarly, the uncertainties in z are δz_+ and δz_-.

H (T)	ν_{sc}	$\delta\nu_+$	$\delta\nu_-$	z_{sc}	δz_+	δz_-
5	1.45	0.20	0.20	5.65	0.4	0.4
2.5	1.60	0.05	0.05	5.55	0.3	0.3
1	1.59	0.04	0.04	5.90	0.4	0.4
0.25	1.70	0.04	0.04	5.95	0.5	0.5
0.1	1.42	0.03	0.01	6.20	0.7	0.3
0.03	1.24	0.05	0.05	6.35	0.8	0.8
0.015	1.19	0.03	0.03	6.55	0.6	0.5
0.010	1.24	0.07	0.01	7.50	0.9	1.0
0.005	1.12	0.05	0.05	7.40	1.0	1.0
0.003	1.08	0.03	0.03	8.47	0.7	1.0
0.001	1.00	0.00	0.00	8.50	1.0	0.5

4.2 Field Dependence of T_g

The H-T phase diagrams resulting from this experiment appear in Fig. 4.3(a) and Fig. 4.4(a). The $H_{c2}(T)$ line is obtained from inverting $T_c(H)$ where T_C is defined as the temperature at which the resistivity is half the normal state value. [Perhaps a more accurate estimate of $H_{c2}(T)$ would be to use the slope of $M(T)$ with a correction for the vortex cores (Hao *et al.*, 1991; Welp *et al.*, 1992); however, the estimate used in this thesis should be sufficient for our purposes.]

The circles denote T_g values, which are listed in Tables 4.5 and 4.6. It is expected (Fisher, Fisher, and Huse, 1991) that in the XY critical regime, at small fields, and close to T_C,

$$H \propto \left|T_c - T_g\right|^{2\nu_o}$$

with $\nu_o \sim \frac{2}{3}$. Most of the high field data published is consistent with this (see Table 1.2). We show that the dependence of H on $\left|T_c(0) - T_g(H)\right|$ is neither a single power-law nor a linear function over the whole field range.

For YBCO, in the high field regime ($H > 0.1$ T), H depends almost linearly on T_g as shown by the line in Fig. 4.4(a). This region, with the inclusion of the mean field transition temperature, can also be described by $H \propto \left[T_c(0) - T_g(H)\right]^{2\nu_o}$ with $\nu_0 = 0.75$, which is a solid line in Fig. 4.4(b).

Fitting the vortex glass transition temperature T_g to the function

$$H \propto \left[T_g(0) - T_g(H)\right]^{2\nu_o} \qquad 4.1$$

results in $\nu_o = 0.65$ for the NCCO film (using $T_g(0) = 18.2\ \mathrm{K}$) and $\nu_o = 0.6$ for the YBCO film. These fits are shown in Fig. 4.3 for the NCCO film and Fig. 4.4(b) for the YBCO film.

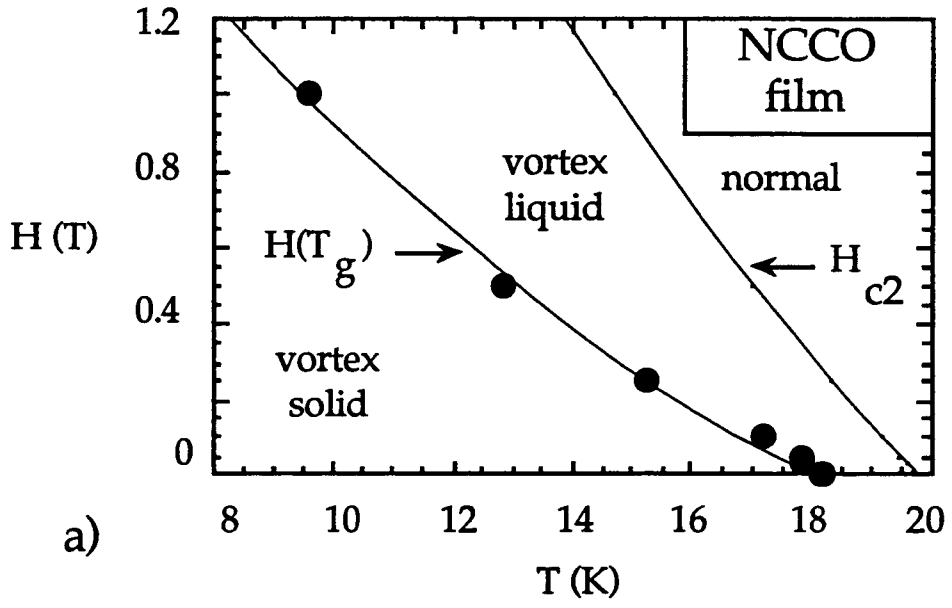

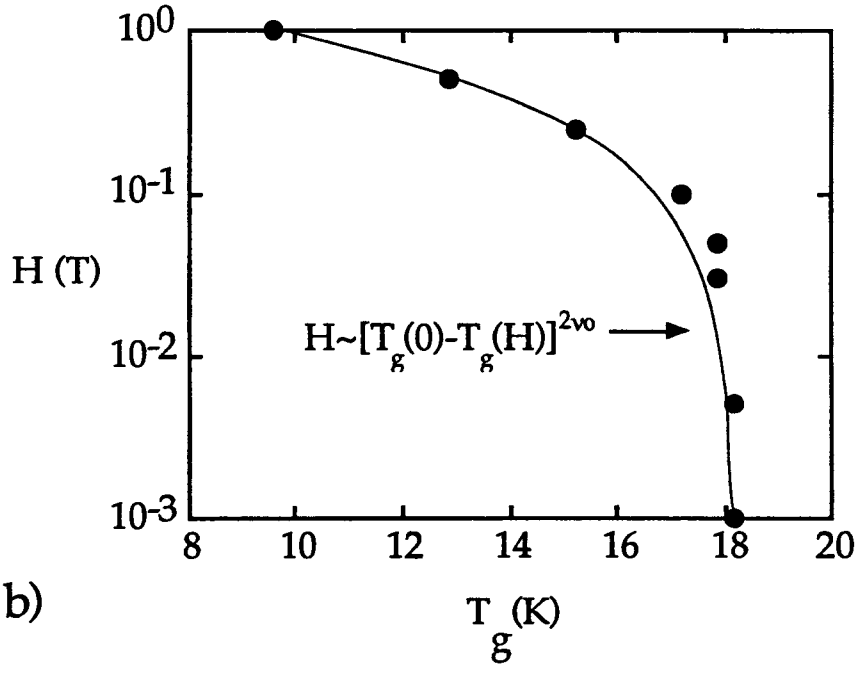

Figure 4.3. *H-T* phase diagram for the NCCO film with H || c. The circles denote T_g values. The line is a fit to $H \propto |T_g(0)-T_g(H)|^{2\nu_o}$ which yields $\nu_o = 0.65$. For the H_{c2} line in (a), T_c is defined as the temperature where the resistivity is 50% of the normal state value. (b) The glass transition temperatures and the $H(T_g)$ fit on a semi-log plot.

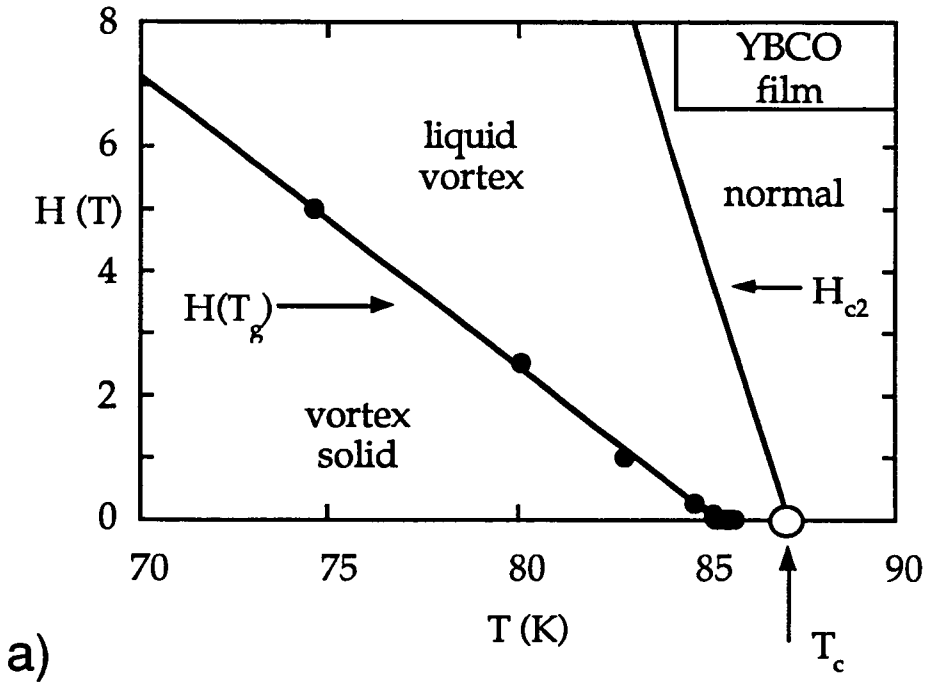

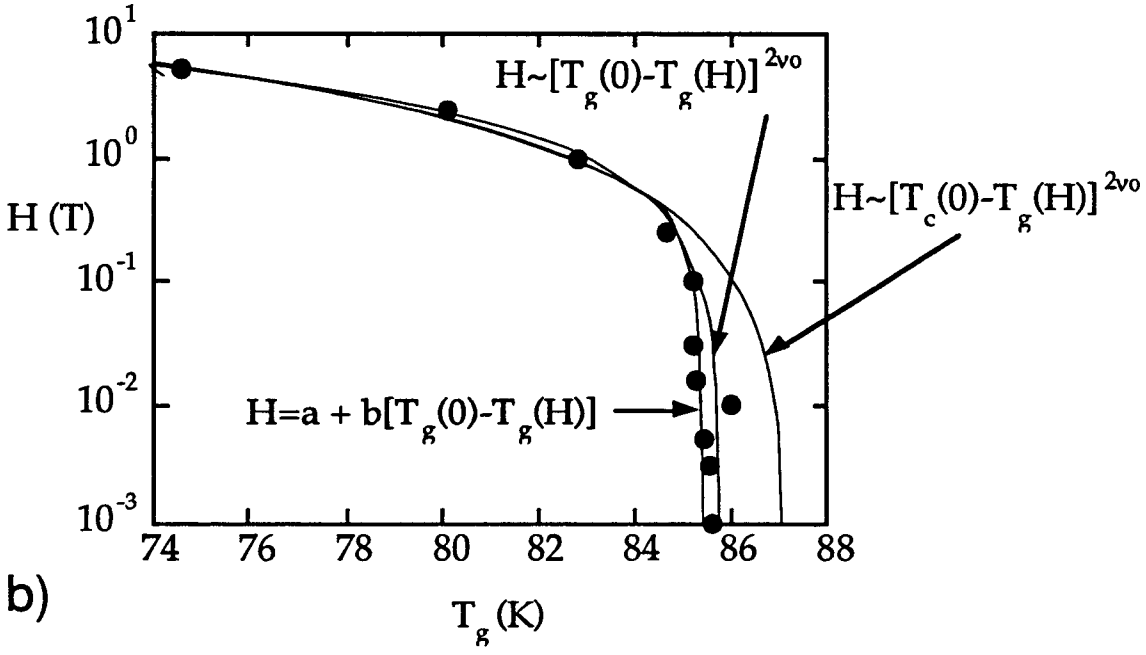

Figure 4.4. *H-T* phase diagram for the YBCO film with H || *c*. The circles denote T_g values. In (b) it is seen that H depends almost linearly on $|T-T_g|$, but can be fit to $H \propto |T_g(0)-T_g(H)|^{2\nu_o}$ yielding $\nu_o = 0.6$. Although $H \propto |T_c(0)-T_g(H)|^{2\nu_o}$ will fit the high-field data (with $\nu_o = 0.75$), it does not describe the low field data.

Table 4.5. T_g and width of scaling region τ for the NCCO film. The uncertainty $\delta\tau$ is the range of temperatures for which it is uncertain whether or not ρ_{lin} has a power-law dependence on $|T - T_g|$.

H (T)	T_g (K)	δT_{g+} (K)	δT_{g-} (K)	τ (K)	$\delta\tau$ (K)
1	9.6	0.25	0.45	5.2	0.10
0.5	12.85	0.30	0.17	4.0	0.18
0.25	15.24	0.13	0.21	3.5	0.19
0.1	17.21	0.09	0.09	2.1	0.13
0.05	17.83	0.01	0.06	2.0	0.11
0.03	17.85	0.10	0.15	2.2	0.07
0.005	18.15	0.02	0.02	1.5	0.16
0.001	18.19	0.02	0.02	1.6	0.04
0	18.17	0.03	0.03		

Table 4.6. T_g and width of scaling region τ for the YBCO film. The uncertainty $\delta\tau$ is the range of temperatures for which it is uncertain whether or not ρ_{lin} has a power-law dependence on $|T - T_g|$.

H (T)	T_g (K)	δT_{g+} (K)	δT_{g-} (K)	τ (K)	$\delta\tau$ (K)
5	74.6	0.40	0.04	5.1	0.35
2.5	80.11	0.30	0.03		
1	82.85			3	
0.25	84.73			2.8	0.7
0.1	85.25	0.15	0.10	1.6	
0.03	85.25	0.15	0.15		
0.015	85.30	0.05	0.10	1.3	0.05
0.010	86.01	0.10	0.20		
0.005	85.50	0.10	0.10	1.8	
0.003	85.56	0.15	0.15		
0.001	85.65	0.10	0.05	1.3	0.15
0	85.80	0.05	0.05		

4.3 Length Scales

When the Lorentz energy gained by nucleating a loop (Eq. 2.40), is set equal to the thermal energy k_BT of the system, we obtain a characteristic length scale L_C,

$$L_c^2 = \frac{k_BT}{J\phi_o}. \tag{4.2}$$

Above T_g, when this length is larger than the vortex glass correlation length $L_c > \xi$ (low currents), the resistivity will be current independent (flux liquid state). When $L_c \sim \xi$, non-linearities set in and the resistivity becomes strongly current dependent. This gives a physical picture of the relation stated previously (§ 2.1), namely,

$$J_{nl} = \frac{k_BT}{\phi_o \xi_{VG}^2}. \tag{4.3}$$

where J_{nl} is the current density at which the resistivity is no longer current independent for isotherms with $T>T_g$. This can also be used to roughly estimate ξ_{VG} as

$$\xi_{VG}^2 = C\frac{k_BT}{J_{nl}\phi_o}. \tag{4.4}$$

where the dimensionless prefactor C (assumed of order unity) is not known. There are several ways of obtaining J_{nl}. All reasonable methods give the same temperature dependence,

$$J_{nl} = J_oT\left|1-\frac{T}{T_g}\right|^{2\nu}, \tag{4.5}$$

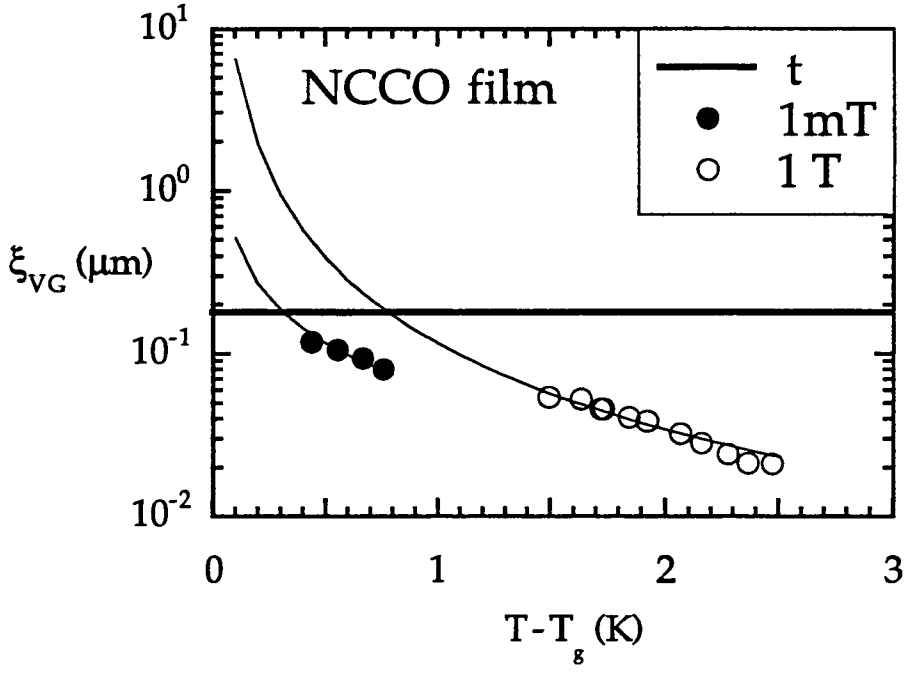

Figure 4.5. Vortex glass correlation length as a function of temperature. Data are for NCCO in 1 T (open circles) and 1 mT (solid circles); see text. The actual magnitude of the correlation length may differ from that shown, which would shift ξ_{VG} vertically. The film thickness is depicted as a horizontal line.

but result in different values of J_0. The solid curves in Fig. 4.5 result from defining J_{nl} as that current for which $F_+(J_{nl}) \approx 3.5$ in the scaled plot (e.g. Fig. 3.8) and then extrapolating to low temperatures using $\xi_{VG} \propto \left|1-\frac{T}{T_g}\right|^{-\nu}$. The resulting temperature dependence for the NCCO film is consistent with finding J_{nl} by estimating the current on the ρ-J plot where ρ first deviates from linearity. These appear in Fig. 4.5 as points (C was adjusted so that the points would lie on the solid curves). The same form for J_{nl} is obtained from using the criterion that J_{nl} is the current for which $\frac{\partial \log E}{\partial \log J} = 1.2$ (Wöltgens,

1993). The latter two definitions of J_{nl} result in $\xi_{VG} > t$, which is unphysical and sets an upper bound on C in Eq. 4.4.

The penetration depth is assumed to have a temperature dependence given by the two-fluid model (Tinkham, 1975),

$$\lambda(T) = \lambda(0)\left[1 - \left(\frac{T_g(H)}{T_c(H)}\right)^4\right]^{-\frac{1}{2}} \qquad 4.6$$

but is otherwise taken to be field-independent. The penetration depth, evaluated at T_g, is only weakly field dependent, as shown in Fig. 4.6. For NCCO it varies from 0.24 μm at low fields to 0.14 μm at 1 T; for YBCO it

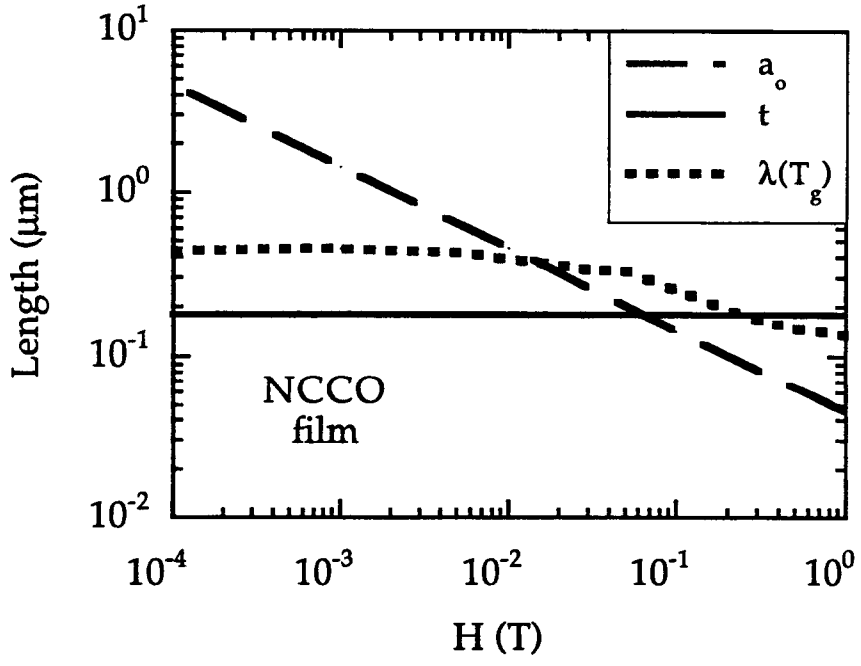

Figure 4.6. Relevant lengths as a function of field for the NCCO film. The solid line depicts the film thickness t, the dashed line represents the average intervortex spacing a_0, and the dotted line is the penetration depth λ evaluated at $T_g(H)$.

changes from 0.5 μm at low fields to 0.25 μm at 5 T. (Near H_{c2}, the effective screening length increases, resulting in a field dependent penetration depth (Clem, 1990)

$$\lambda(B) = \lambda(0)\left[1 - \frac{B}{H_{c2}(T)}\right]^{-\frac{1}{2}}. \qquad 4.7$$

This correction has not been calculated explicitly, but would change λ by less than 10%.) The average intervortex spacing $a_o = \sqrt{\frac{\phi_o}{B}}$ increases from 0.02 μm at 5 T to 1 μm at 1 mT. The film widths (not shown) remain larger than all other lengths, but the film thickness is exceeded by both a_o and ξ_{VG} in certain regimes.

4.4 The Elusive Critical Exponent μ

The scaling of $\rho - J$ isotherms investigates the possibility of a phase transition, but does not directly probe whether or not the low temperature phase is a vortex glass. To determine this, one must fit the low-temperature data to Eq. 1.14 (c.f. Eqs. 2.55 and 2.61). Furthermore, the values of μ resulting from this analysis should help determine if the VG or CC model best describes the system, since these models have different predictions for μ (see § 2.7).

Two methods for fitting the low-temperature $\rho - J$ isotherms to Eq. 1.14 have been reported. The first analysis was reported by Dekker, Eidelloth, and Koch (1992), who linearized Eq. 1.14 by writing it as

$$\ln\rho = \ln\rho_o + (J_o)^{\mu}\left[-J^{-\mu}\right]. \qquad 4.8$$

A straight line fit to $\ln\rho$ versus $-J^{-\mu}$ is performed for various values of μ, and the μ which gives the best fit is deemed to be the correct value of μ; the slope and y-intercept of this line give J_o and ρ_o. It was found that μ is a function not only of magnetic field and temperature, but also current.

Leghissa *et al.* (1993) approached the problem differently. Rather than finding one value of μ for each $\rho - J$ curve, they allow μ to vary with current along each isotherm. By calculating

$$\mu(J) = -\frac{\partial}{\partial \log J} \log\left(\frac{\partial \log E}{\partial \log J}\right), \qquad 4.9$$

every curve generates a function $\mu(J)$. To find the temperature dependence of μ, the maximum of each $\mu(J)$ is defined as μ^*, and $\mu^*(T)$ is then displayed. Thus, the method of Leghissa *et al.* also generates $\mu = \mu(T, B, J)$.

The analysis methods of both Dekker, Eidelloth, and Koch and Leghissa *et al.* were used to extract values of μ from some of the data presented in this thesis. Experimental problems were encountered with each method. As mentioned previously (§ 1.4 and 3.7) at sufficiently high currents flux flow effects should dominate, and a downward curvature is expected in the $\log\rho - \log J$ curves. Using the method of Dekker, Eidelloth, and Koch it was found that the value obtained for μ depends slightly on the criteria used to cut the data; it decreases by about 0.2 for every 5×10^3 Acm^{-2} decrease in J (approximately each data point cut). In fact, if the current regime is too narrow, a fit to Eq. 1.14 gives $\mu \approx 0$.

Another difficulty in applying the method of Leghissa *et al.* is that the normal scatter present in experimental data is magnified when a derivative is taken, and further disproportioned when a second derivative is taken. Thus, it was necessary to smooth the data before applying Eq. 1.14.

What we find for μ is similar to what other researchers have found. In particular, we determine that μ is a function of current as well as magnetic field and temperature. Thus, Eq. 1.14 must be modified to

$$\rho(J) \propto \exp\left[-\left(\frac{J_o}{J}\right)^{\mu(J)}\right], \qquad 4.10$$

suggesting that perhaps neither the VG nor the CC model is sufficiently complete to fully describe the measured current dependence of the resistivity at low temperatures. However, Dekker, Eidelloth, and Koch propose that their data suggests two plateaus, one at high currents ($\mu = 0.94$), and one at low ($\mu = 0.19$). Thus, it is argued that the change in μ is indicative of a crossover between high and low current regimes (with μ constant in each), rather than indicating an explicit current dependence of μ.

CHAPTER 5
DISCUSSION

The high-field exponents lend support to the vortex-glass model of FFH. The critical exponents reported here for NCCO films are consistent with those found for YBCO films. Thus, the vortex transition is the same for the two materials. Indeed, the exponents for YBCO films are closer to those of NCCO films than to those of YBCO single crystals (Kötzler *et al.*, 1994a). This suggests that the defect structure (which is likely to be similar in all perovskite films grown under similar conditions) is more important than intrinsic differences in chemical composition, T_c, pair coherence length, and H_{c2}, in determining the nature of the phase transition. A previous analysis of $\rho - J$ characteristics of an NCCO film (Yeh *et al.*, 1992) resulted in values for critical exponents which were closer to those found for films than crystals. It has been proposed that the notably lower exponents some researchers find result from an attempt to scale the region of $\rho - J$ space where flux-flow effects are dominant, rather than the lower J regime where a vortex glass phase transition is expected. This argument is plausible for some of the published data. However, the deviations from scaling seen in the collapse of the NCCO film data of Yeh *et al.* (1992) do not seem sufficiently severe to justify this conclusion.

The similarity of the exponents for the NCCO and YBCO films extends even to their field dependence. Such dependence is not predicted by scaling theory, where the critical exponents are determined only by the universality class of the transition. If these data are to be interpreted as the signature of a

phase transition, and not merely a convenient parameterization, the most likely explanation for the field dependence is that a fundamental change in the transition occurs at low fields. Preliminary work (Brown and Tate, 1995) points to the possibility that the vortex transition may be approaching first order at low fields. Nevertheless, several interpretations deserve consideration.

5.1 Critical Regime

It has been argued that the critical region becomes immeasurably small at low field (Koch, Foglietti, and Fisher, 1990). However, we define the critical region consistently at all fields and it remains measurable down to at least 1 mT. The VG model predicts a power-law dependence of ρ_{lin} on $|T - T_g|$ (Eq. 2.9). Fig. 5.1 shows that $\log \rho_{lin}$ versus $\log|T - T_g|$ is indeed a straight line up to some field-dependent temperature, as predicted. Furthermore, the value obtained for s is consistent with both the expected value and with that obtained by other experiments (see Tables 1.2, 4.1, and 4.2). This temperature can be used as an estimate of the critical region (Safar *et al.*, 1992), which is displayed in Fig. 5.2(a) as a function of field for NCCO; the critical region decreases from 5 K at 1 T to 1.5 K at 1 mT. The widths of the critical regions for both films are listed in Tables 4.5 and 4.6.

In § 1.5 it was stated that both the temperature width τ_T of the fluctuation dominated regime near H_{c2}, and the width τ_m of the melting transition (presumably assumed to be second order by Feigel'man *et al.*, 1993) are predicted to vary with field as

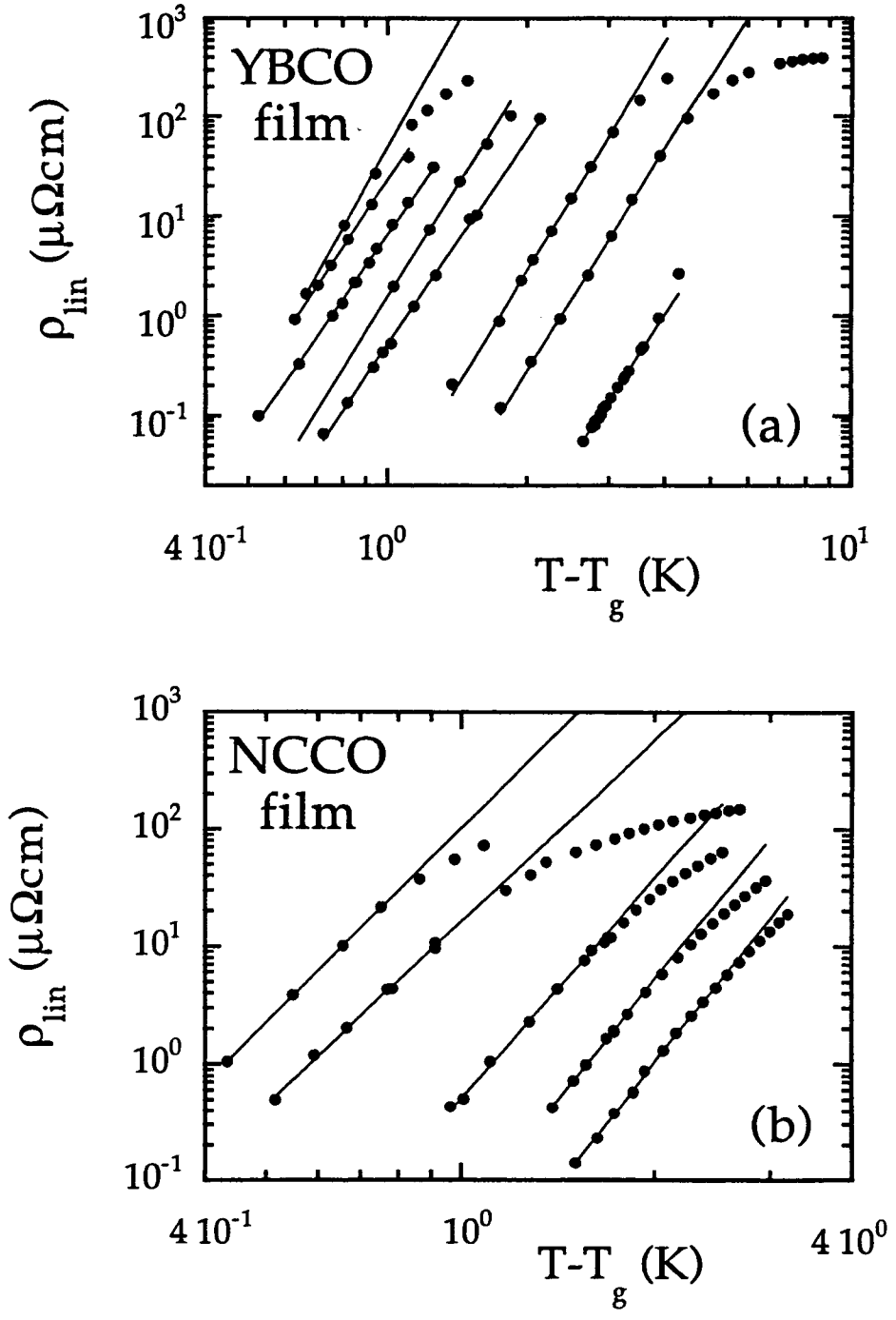

Figure 5.1. Low-current resistivity ρ_{lin} as a function of $|T-T_g|$. A linear slope on this log-log plot indicates that the resistivity obeys the predicted form. The temperature at which $\log\rho_{lin}$ is no longer a linear function of $\log|T-T_g|$ defines the critical region. The data shown are for (a) the YBCO film in fields 0 T, 5 mT, 30 mT, 0.1 T, 0.25 T, 1 T, 2.5 T and 5 T, and (b) the NCCO film in fields (from left to right) 1 mT, 0.1 T, 0.25 T. 0.5 T, and 1 T.

$$\tau \approx \beta T_c G_i^{1/3} \left[\frac{H_{c2}(T)}{H_{c2}(0)} \right]^{\delta} \qquad 5.1$$

where $\delta=\frac{2}{3}$, $\beta \sim 3-7$ for τ_m, and $\beta \sim 1$ for τ_T. It is reasonable to expect that the width of the vortex glass region may also have this form. For the NCCO film $T_c G_i^{1/3} \approx 1$ and $H_{c2} \sim 2.7$ T (see Table 1.1). Eq. 5.1 fits the data quite well, as displayed in Figs. 5.2(a) and (b), yielding $\delta=0.5$ and $\beta \sim 5.4$. Although the prefactor β seems reasonable, the exponent δ differs considerably from the predicted value.

5.2 Dimensional Crossover

5.2.1 Comparison with Bi2223 Films

In a recent paper that presented the scaling of $\rho - J$ isotherms for Bi2223 films, Yamasaki *et al.* (1994) suggested that the field-dependent exponents observed in YBCO could be explained by assuming a two-dimensional transition at low fields. They noted that upon setting $d = 2$ in the scaling analysis for the low fields, one could define 2D scaling exponents z' and ν', which can be found from the 3D critical exponents using $\nu' = 2\nu$ and $z' = \frac{z-1}{2}$; the resulting 2D critical exponents z' and ν' are closer to the high field ($d = 3$) values. Even if it were clear in what sense low field implies two-dimensionality, one would not expect the critical exponents to be the same in two dimensions as in three; a universality class is partly determined by the dimensionality. For example, the Ising model calls for $\nu = 1.0$ in 2D but $\nu = 0.627$ in 3D. In dimensions

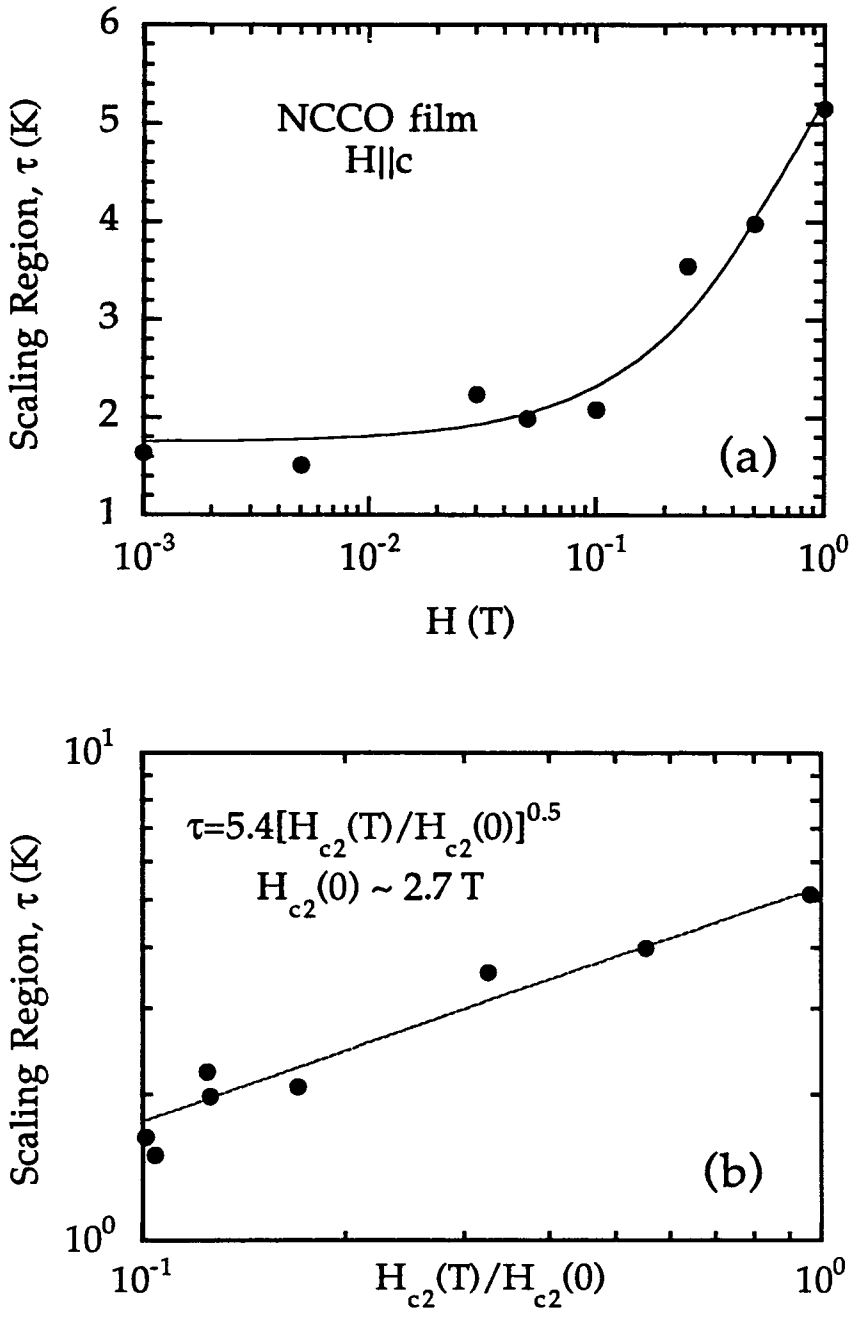

Figure 5.2. Critical region τ as a function of field for the NCCO film. The line is a fit to Eq. 5.1. The critical region above T_g is comprised of isotherms for which $\log\rho_{lin}$ is a linear function of $\log|T-T_g|$, and the critical region is assumed to be symmetric about T_g. This definition corresponds remarkably well with the range of isotherms which can be scaled. In (b), $H_{c2}(T)$ is obtained by defining T_c as the temperature at which the resistivity is 50% of its normal state value.

above the upper critical dimension, $d_u = 6$, of the glass transition, the exponents should converge to their mean-field values $z = 4$ and $\nu = 0.5$ (Dorsey, Huang, and Fisher, 1992); the exponents are expected to increase for dimensions less than d_u (Fisher, Fisher, and Huse, 1991). In light of this, it is not reasonable to change the value of d merely to preserve the high-field values of the critical exponents.

However, the comparison between the Bi2223 films and the low-field data presented here is interesting. That experiment extracted 3D critical scaling exponents $z = 12.2$, $\nu = 0.69$ and 2D exponents $z' = 5.61$, $\nu' = 1.38$. Since Bi2223 is expected to be quasi-two-dimensional, they considered the latter more appropriate. While the 3D values of z and ν are not identical to our low-field values, they are similar in that the dynamic exponent is higher and the static exponent is lower than predicted by the VG model.

Bi superconductors are extremely anisotropic (γ~55-100) and expected to behave quasi-two-dimensionally at high fields (≥0.3 T), and three-dimensionally at low fields. When the interlayer spacing l exceeds γa_0, the vortices are expected to decouple into so-called pancake vortices (Clem, 1991), resulting in reduced vortex interactions between superconducting planes. Rather than being treated as lines, vortices are taken as points (vortex pancakes) which interact within each layer. In YBCO, the crossover field is expected to be too large for this effect to be observed.

5.2.2 Size Effects and the Ando-Kubota-Tanaka Experiment

Another interesting comparison is with a recent experiment by Ando, Kubota, and Tanaka (AKT) (1992). They determined the VG phase transition parameters for very narrow (<0.5 μm) YBCO microbridges, and observed a systematic increase in the dynamic exponent with decreasing bridge width. In their limited field range (1 - 3 T), they also found a small field dependence[8]. At the lowest flux densities in our experiment, the fraction of vortices along the edge of our wider YBCO microbridge width is comparable to that in the AKT experiment. AKT suggested that the increased z could be related to a softening of the vortex lattice. This softening, inferred from the systematic decrease in the value of T_g with film width at constant field, was explained by a reduced interaction energy density of vortices near the edge of the film. We could be observing a related effect since the elastic moduli of the vortex lattice decrease in the low-field region. It is also worth noting that, in contrast to our experiment, the large dynamic exponents observed in the AKT experiment are not accompanied by a decrease in the critical region. There, the critical region remains several Kelvin wide, even at the largest z-values. Finite size scaling (FSS) theory (Barber, 1983; Cardy, 1988) provides an alternative explanation of the AKT data. I have re-analyzed the AKT data within the context of FSS; see Appendix C.

For our data, estimates of ξ_{VG} indicate that the field dependence of the exponents is not a finite size effect. A few Kelvin from T_g, ξ_{VG} can be directly estimated from J_{nl} via Eq. 4.4 (assuming d=3), and it is well below the film thickness. Close to T_g, our experimental resolution prohibits us from directly

8. Y. Ando, private communication.

measuring J_{nl}, but ξ_{VG} can be estimated by extrapolating the values far from T_g. Although Eq. 4.4 gives only an estimate of ξ_{VG}, we do not observe it leveling off as it would if t were limiting it. This is demonstrated in Fig. 4.5 for 1 mT and 1 T for the NCCO film. This can be compared to Fig. 5.3, in which Wöltgens (1993) finds experimentally that, for thin films, ξ_{VG} saturates at the film thickness. Wöltgens estimated the correlation length along the c axis using,

$$\xi_c = \frac{k_B T}{\gamma \Phi_o J_{nl}} \qquad 5.2$$

where $\gamma \approx 5$ (YBCO) and J_{nl} is defined as the J at which $\frac{\partial \log E}{\partial \log J} = 1.2$. In our experiment, the region where ξ_{VG} would be greater than t decreases with field, which makes it more difficult to see the effects of dimensionality at low fields and less likely that the different low-field exponents can be an artifact of a finite-size effect. Moreover, the scaling exponents are unaffected by the inclusion of the data in this narrow temperature region.

5.3 Length Scales Revisited

The field dependence of the critical exponents could indicate a crossover between two different regimes. A crossover from 3D to 2D seems unlikely, as discussed in § 5.2. A field-induced change in the symmetry of the order parameter could result in a change in the universality class, but it is unclear what this symmetry change would be. An interesting possibility (Brown and Tate, 1995) is that the transition could be approaching first order at the lowest fields, since at low field the length scale characterizing the disorder may become smaller than the intervortex spacing. In any event, we should

examine the relationship between the average intervortex spacing a_o and the other lengths in the system.

For the NCCO data within the critical region as defined in § 5.1, ξ_{VG} is smaller than a_o for approximately half of the data at high fields; at the lowest

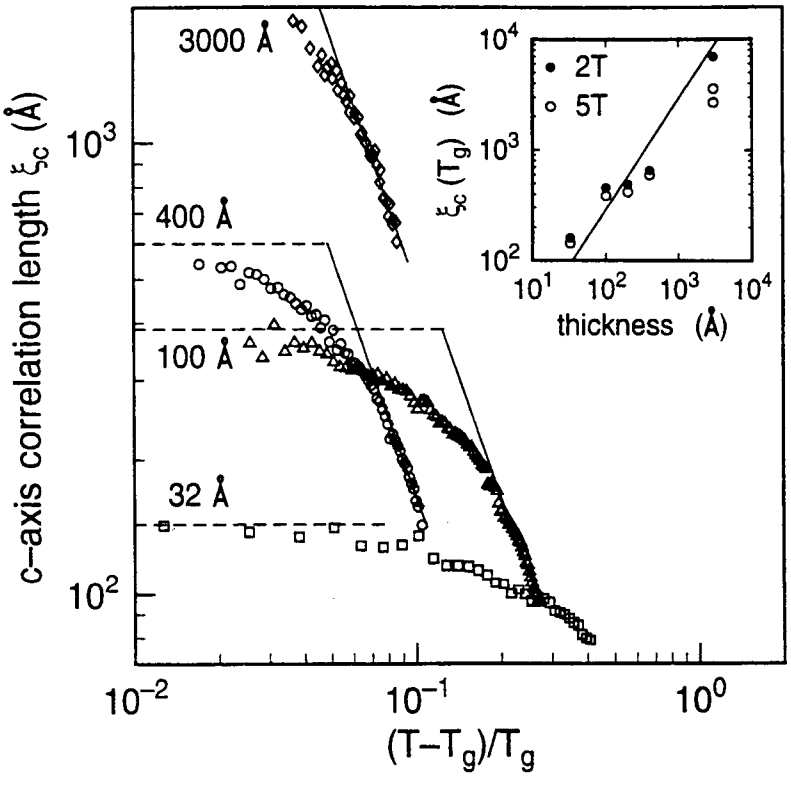

Figure 5.3. Leveling-off of ξ_{VG} for thin samples. Temperature dependence of the correlation length along the c axis of an YBCO film in an applied field of 5 T, for various thicknesses. The solid lines denote the critical behavior $\xi_{VG} \propto |T-T_g|^{1.7}$. The dashed lines indicate the leveling off upon approach of T_g. The inset shows the plateau ξ_{VG} versus the nominal film thickness. The solid line denotes a linear relationship. (From Wöltgens, 1993, Fig. 3.5.)

fields, $\xi_{VG} < a_o$ for all the scaled data. For YBCO at the highest fields, the scaled data is well within the temperature range for which $\xi_{VG} > a_o$. At lower fields, the limit $\xi_{VG} \approx a_o$ is approached. It seems reasonable that the physics should be different in the two limits. This possibility is suggested by Fisher, Fisher, and Huse (1991) where it is noted that if $a_o >> \xi_{VG}$ the barrier for vortex recombination can be large, and that if the process is too slow to occur then the universality class of the transition and the glass phase may change (p. 152). Of course, a change in universality class would result in a change in exponents. A correlation length shorter than the intervortex spacing may suggest that dissipation is due to single-vortex movement (Ando, 1993).

In Kandoff's block-spin approach described in § 2.1.2, the requirement was set that $a < aL << \xi_{VG}$, with a the lattice spacing. However, since critical behavior results from correlation of the phase of the superconducting wave function, the lattice spacing may be set by the coherence length of the superconducting wavefunction, and not by the intervortex spacing. This was suggested by Ando (1993). FFH state that even a single vortex line in a random potential is in a glassy phase (p. 152). Indeed, they derived Eq. 1.14 for a single, randomly pinned vortex line, and then generalized to the case of many interacting vortices (p. 148).

The intervortex spacing exceeds the penetration depth $\lambda(T_g)$ below about 30 mT for the NCCO film and 10 mT for the YBCO film, resulting in reduced vortex interaction. These fields are where the exponents have assumed their low-field values. Vortex interactions decrease with distance r as $e^{-\frac{r}{\lambda}}$ for $r >> \lambda$, and thus occur out to distances of order the penetration depth λ. The

physics governing the transition could change for different vortex-interaction strengths. Since vortex interactions cause the phase coherence (Huse, Fisher, and Fisher, 1992) one may wonder how phase coherence can exist if the vortex separation exceeds the penetration depth, $a_0 > \lambda$. However, critical phenomena are connected with fluctuations which are long-ranged compared with the range of the force; fluctuations don't probe the details of the microscopic interatomic potential (Kandoff, 1971).

For completeness, it should noted that in the middle of the crossover region, a_0 equals the film thickness. However, it seems unlikely that this is significant.

Another important length in the system is that which characterizes the range of disorder in the sample, which may become smaller than a_0 at low fields. It has been found that in very clean YBCO crystals (low disorder), a first-order transition occurs at fields below 10 T, but a second-order vortex glass transition occurs at higher fields. That work, coupled with preliminary work on twinned YBCO crystals (Brown and Tate, 1995), suggests that the anomalous low-field exponents found in films could be signaling a crossover from a second order transition to a first order. It remains unclear why ρ_{lin} continues to have a power-law dependence on $|T - T_g|$, indicating the existence of a scaling region. It is also remarkable that the quality of the scaling collapse remains so good at low fields. If we are observing the start of a crossover to a first order transition, then evidently the physics in the crossover region is complicated

5.4 Other Experiments and Theoretical Predictions at Low Field

We are not aware of a theoretical model which both attempts to describe a second-order phase transition at low fields and is consistent with our data. FFH predict that a transition into the Meissner phase will be characterized by $z \approx 2$ and $\nu \approx \frac{2}{3}$, but in thin films H_{c1} is anticipated to be smaller than the fields we used. A Kosterlitz-Thouless (KT) transition (which applies in two dimensions at zero field) predicts a power-law isotherm $\rho \propto J^2$ at the KT transition temperature. At T_g we observe a power-law isotherm at all fields, but our low field result is $\rho \propto J^{3.2}$.

Zero-field E-J curves have been reported (Dekker *et al.*, 1991) with an attempt to extract scaling exponents from them. There, the authors show data at 4 T and at zero field for a much thinner YBCO film (50 nm) than is used here or in most of the other work reported in the literature. They note deviations from the 3D scaling at both fields, especially the lower, and attribute them to dimensional effects. For the zero-field data they use the isotherms at high current density in the vicinity of the mean-field transition temperature to extract a value of z = 2.0, which is in agreement with the prediction of FFH for the transition to the Meissner state, but they do not explore the crossover from the high-field value of z = 4.6. In our case, dimensional effects should be absent because the film is thicker. However, our zero-field T_g is defined in the same manner as at high field (namely, by a power-law $\rho - J$ isotherm) and is lower than the mean-field T_c, (defined from $\rho < 10^{-3} \mu\Omega cm$).

As mentioned in the introduction (§ 1.7), Chang *et al.* scaled $\rho - J$ data for an YBCO film in ambient field and found z=7. ν=0.75, (similar to what we find at low field), but these authors did not present any data taken in an applied field.

5.5 Conclusion

This is the first consistent comparison of critical scaling in NCCO and YBCO thin films. Their dc $\rho - J$ characteristics in a magnetic field closely resemble one another and can be similarly scaled in the context of a second-order normal-to-superconducting phase transition. Within error, we obtain the same critical exponents for the two materials. Hence, the same transition occurs in NCCO as in YBCO, even though these materials have different anisotropies, transition temperatures and coherence lengths; this helps isolate the primary factors which govern vortex dynamics in copper-oxide high-T_c superconductors. The high-field results, taken alone, support the VG hypothesis, indicating that there does exist a second-order phase transition from a vortex liquid to a truly superconducting vortex glass state. A consistent analysis of the low-field data yields a well defined, though narrow, critical region and gives different critical exponents. The field dependence of the critical exponents indicates a crossover between different regimes with decreasing field, suggesting that a fundamental change in the transition occurs at low fields.

BIBLIOGRAPHY

Abrikosov, A. A., (1957). Zh. Eksp. Teor. Fiz. 32, 1442 [Sov. Phys. JETP 5, 1174 (1957)].

Anderson, P. W., (1962). Phys. Rev. Lett. 9, 309.

Anderson, P. W., and Y. B. Kim, (1964). Rev. Mod. Phys. 36, 39.

Ando, Y., (1993). *Vortex-Glass Transition in Narrow Superconducting Strips,* Ph.D. thesis, University of Tokyo (unpublished).

Ando, Y., H. Kubota, and S. Tanaka, (1992). Phys. Rev. Lett. 69, 2851.

Barber, M. N., (1983). In *Phase Transitions and Critical Phenomena, vol. 8,* edited by C. Domb and J. L. Lebowitz (Academic Press, New York).

Bardeen, J., L. N. Cooper, and J. R., Schrieffer, (1957). Phys. Rev. 108, 1175.

Bardeen, J., and M. J. Stephen, (1965). Phys. Rev. A 140, 1197.

Barenblatt, G. I., (1987). *Dimensional Analysis,* (Gordon and Breach Science Publishers, New York).

Berberich, P., J. Tate, W. Dietsche, and H. Kinder, (1988). Appl. Phys. Lett. 53, 925.

Binder, K., and A. P. Young, (1986). Rev. Mod. Phys. 58, 801.

Bishop, D. J., P. L. Gammel, and D. A. Huse, (1993). Sci. Am. Feb., 48.

Bishop, D. J., P. L. Gammel, D. A. Huse, and C. A. Murray, (1992). Science 255, 165.

Blatter, G., M. V. Feigel'man, V. B. Geshkenbein, A. I. Larkin, and V. M. Vinokur, (1994). Rev. Mod. Phys. 66, 1124.

Brandt, E. H., (1993). In *Phase Transitions and Relaxation in Systems with Competing Energy Scales,* edited by T. Riste and D. Sherrington (Kluewer Academic Publishers, Boston).

Brown, B., and J. Tate, (1995). In preparation.

Cardy, J. L., (1988). *Finite-Size Scaling,* (North-Holland, New York).

Chang, C. Y., C.-S. Lue, and Y. C. Chou, (1994). Phys. Rev. B 49, 1488.

Cieplak, M., J. R. Banavar, M. S. Li, and A. Khurana, (1992). Phys. Rev. B 45, 786.

Clem, J. R., (1990). In *Physics and Materials Science of High-Temperature Superconductors*, edited by R. Kossowsky, S. Methfessel, and D. Wohleben (Kluwer Academic Publishers, Dordrecht).

Clem, J. R., (1991). Phys. Rev. B 43, 7837.

Dalichaouch, Y., B. W. Lee, C. L. Seaman, J. T. Markert, and M. B. Maple, (1990). Phys. Rev. Lett. 64, 599.

Deak, J., M. McElfresh, R. Muenchausen, S. Foltyn, and R. Dye, (1993). Phys. Rev. B 48, 1337.

Dekker, C., W. Eidelloth, and R. H. Koch, (1992). Phys. Rev. Lett. 68, 3347.

Dekker, C., R. H. Koch, B. Oh, and A. Gupta, (1991). Physica C 185 - 189, 1799.

Dekker, C., P. J. M. Wöltgens, R. H. Koch, B. W. Hussey, and A. Gupta, (1992). Phys. Rev. Lett. 69, 2717.

Dolan, G. J., F. Holtzberg, C. Feild, and T. R. Dinger, (1989). Phys. Rev. Lett. 62, 2184.

Dorsey, A. T., M. Huang, and M. P. A. Fisher, (1992). Phys. Rev. B 45, 523.

Ebner, C., and Stroud, (1985). Phys. Rev. B 31, 165.

Feigel'man, M. V., V. B. Geshkenbein, L. B. Ioffe, and A. I. Larkin, (1993). Phys. Rev. B. 48, 16641.

Feigel'man, M. V., V. B. Geshkenbein, A. I. Larkin, and V. M. Vinokur, (1989). Phys. Rev. Lett. 63, 2203.

Fischer, K. H., and T. Nattermann, (1991). Phys. Rev. B 43, 10372.

Fisher, D. S., (1987). J. Appl. Phys. 61, 3672.

Fisher, D. S., (1988). Phys. Rev. B 38, 386.

Fisher, D. S., (1993). In *Phase Transitions and Relaxation in Systems with Competing Energy Scales*, edited by T. Riste and D. Sherrington (Kluewer Academic Publishers, Boston).

Fisher, D. S., M. P. A Fisher, and D. A. Huse, (1991). Phys. Rev. B 43, 130.

Fisher, M. P. A., (1989). Phys. Rev. Lett. 62, 1415.

Gammel, P. L., L. F. Schneemeyer, and D. J. Bishop, (1991). Phys. Rev. Lett. 66, 953.

Ginzburg, V. L., L. D. Landau, (1950). Zh. Eksprim. i Teor. Fiz 20, 1064.

Gor'kov, L. P., (1959). Soviet Phys.-JETP 9, 1364.

Hao, Z., J. R. Clem, M. W. McElfresh, L. Civale, A. P. Malozemoff, and F. Holtzberg, (1991). Phys. Rev. B 43, 2844.

Hermann, B. A., (1992). *Resistance in Superconductors - A Comparison Between NdCeCuO and YBaCuO Thin Films*, M.S. thesis, Oregon State University, (unpublished).

Hidaka, Y., and M. Suzuki, (1989). Nature 338, 635.

Hohenberg, P. C., and B. I. Halperin, (1977). Rev. Mod. Phys. 49, 435.

Houghton, A., and M. A. Moore, (1988). Phys. Rev. B 38, 5045.

Huang, F., G. J. Mankey, M. T. Kief, and R. F. Willis, (1993). J. Appl. Phys. 73, 6760.

Huse, D. A., M. P. A. Fisher, and D. S. Fisher, (1995). Nature 358, 553.

Hwa, T., D. R. Nelson, and V. M. Vinokur, (1993). Phys. Rev. B 48, 1167.

Kandoff, L. P., (1971). In *Proceedings of the International School of Physics, Enrico Fermi*, edited by M. S. Green (Academic Press, New York).

Kenning, G. G., J. Bass, W. P. Pratt, Jr., D. Leslie-Pelecky, L. Hoines, W. Leach, M. L. Wilson, R. Stubi, and J. A. Cowen, (1990). Phys. Rev. B 42, 2393.

Kes, P. H., J. Aarts, J. van den Berg, C. J. van der Beek, and J. A. Mydosh, (1989). Superconductor Science and Technology 1, 242.

Koch, R. H., V. Foglietti, M. P. A. Fisher, (1990). Phys. Rev. Lett 64, 2586.

Koch, R. H., V. Foglietti, W. J. Gallagher, G. Koren, A. Gupta, and M. P. A. Fisher, (1989). Phys. Rev. Lett. 63, 1511.

Kötzler, J., M. Kaufmann, G. Nakielski, R. Behr, and W. Assmus, (1994a). Phys. Rev. Lett. 72, 2081.

Kötzler, J., G. Nakielski, M. Baumann, R. Behr, F. Goerke, and E. H. Brandt, (1994b). Phys. Rev. B 50, 3384.

Kussmaul, A., (1992). *Transport Measurements on NdCeCuO Thin Films,* Ph.D. thesis, Massachusetts Institute of Technology, (unpublished).

Larkin, A. I., and Y. N. Ovchinnikov, (1979). J. Low Temp. Phys. 34, 409.

Leghissa, M., A. Königer, M. Lippert, W. Dorsch, M. Kraus, and G. Saemann-Ischenko, (1993). Z. Phys. B 92, 163.

Li, Q., H. J. Wiesmann, M. Suenaga, L. Motowidlow, and P. Haldar, (1994). Phys. Rev. B 50, 4256.

Lindemann, F., (1910.) Phys. Z. 11, 609.

Ma, S.-K., (1976). *Modern Theory of Critical Phenomena,* (W. A. Benjamin, Inc., Reading, MA).

Mao, J., D. H. Wu, J. L. Peng, R. L. Greene, and S. M. Anlage, (1995). Phys. Rev. B. 51, 3316.

Mao, S. N., X. X. Xi, S. Bhattacharya, Q. Li, T. Venkatesan, J. L. Peng, R. L. Greene, J. Mao, D. H. Wu, S. Anlage, (1992). Appl. Phys. Lett. 61, 2356.

Moore, M. A., and Murphy, (1994). Phys. Rev. Lett. 50, 3450.

Natterman, T., (1990). Phys. Rev. Lett. 64, 2455.

Nelson, D. R., and V. M. Vinokur, (1992). Phys. Rev. Lett. 68, 2398.

O, Beom-hoan and J. T. Markert, (1993). Phys. Rev. B 47, 8373.

Olsson, H. K., R. H. Koch, W. Eidelloth, and R. P. Robertazzi, (1991). Phys. Rev. Lett. 66, 2661.

Plischke, M., and B. Bergerson, (1989). *Equilibrium Statistical Physics,* (Prentice Hall, Englewood Cliffs, NJ).

Reger, J. D., T. A. Tokuyasu, A. P. Young, and M. P. A. Fisher, (1991). Phys. Rev. B. 44, 7147.

Roberts, J. M., B. Brown, B. A. Hermann, and J. Tate, (1994). Phys. Rev. B 49, 6890.

Roberts, J. M., B. Brown, J. Tate, X. X. Xi, and S. N. Mao, (1995). Accepted for publication in Phys. Rev. B.

Ryu, S., S. Doniach, G. Deutscher, A. Kapitulnik., (1992). Phys. Rev. Lett. 68, 710.

Safar, H., P. L. Gammel, D. J. Bishop, D. B. Mitzi, and A. Kapitulnik, (1992). Phys. Rev. Lett. 68, 2672.

Silver, R. M., A. L. de Lozanne, and M. Thompson, (1993). IEEE Trans. Appl. Superconductivity 3, 1394.

Tang, Z. X., C M Sorensen, K. J. Klabunde, and G. C. Hadjipanayis, (1991). Phys. Rev. Lett. 67, 3602.

Tate, J., and B. A. Hermann, (1992). Physica C 193, 207.

Tiernan, W. M., and R. B. Hallock, (1992). Phys. Rev. B 46, 3688.

Tinkham, M., (1975). *Introduction to Superconductivity,* (McGraw-Hill, New York).

Uzunov, D. I., (1993). *Theory of Critical Phenomena,* (World Scientific, London).

Welp, U., S. Fleshler, W. K. Kwok, R. A. Klemm, V. M. Vinokur, J. Downey, and G. W. Crabtree, (1992). In *High Temperature Superconductivity,* edited by S. K. Malik and S. S. Shah (Nova Science Publishers., New York).

Welp, U, W. K. Kwong, G. W. Crabtree, K. G. Vandervoort, and J. Z. Liu, (1989). Phys. Rev. Lett. 62, 1908.

Wolf, S. A., D. U. Gubser, and Y. Imry, (1979). Phys. Rev. Lett. 42, 324.

Wöltgens, P. J. M., (1993). *Vortex-Glass Dynamics in High-T_c Superconducting Films,* Ph.D. thesis, (unpublished)

Wöltgens, P. J. M., C. Dekker, R. H. Koch, B. W. Hussey, and A. Gupta, (1994). Physica B 194 - 196, 1911.

Wöltgens, P. J. M., C. Dekker, J. Swüste, and H. W. de Wijn, (1993). Phys. Rev. B 48, 16826.

Worthington, T. K., E. Olsson, C. S. Nichols, T. M. Shaw, and D. R. Clarke, (1991). Phys. Rev. B 43, 10538.

Wu, D. H., J. Mao, S. N. Mao, J. L. Peng, X. X. Xi, T. Venkatesan, R. L. Greene, and S. M. Anlage, (1993). Phys. Rev. Lett. 70, 85.

Xenikos, D. G., J.-T. Kim, T. R. Lemberger, (1993). Phys. Rev. B 48, 7742.

Yamasaki, H., K. Endo, S. Kosaka, M. Umeda, S. Yoshida, and K. Kajimura, (1994). Phys. Rev. B 50, 12959.

Yeh, N.-C., W. Jiang, D. S. Reed, A. Gupta, F. Holtzberg, and A. Kussmaul, (1992). Phys. Rev. B 45, 5710.

Yeh, N.-C., W. Jiang, D. S. Reed, and U. Kriplani., (1993a). Phys. Rev. B 47, 6146.

Yeh, N.-C., D. S. Reed, W. Jiang, U. Kriplani, C. C. Tsuei, C. C. Chi, and F. Holtzberg, (1993b). Phys. Rev. Lett. 71, 4043.

Yeomans, Y. M., (1992). *Statistical Mechanics of Phase Transitions*, (Oxford Scientific Publication, Oxford).

APPENDICES

APPENDIX A

DOMAIN WALL ENERGIES IN AN ISING MODEL

The Ising model consists of a lattice of sites, where each site can have a spin of $\sigma(r)=\pm 1$. Aligned spins contribute and energy $-J_{ij}$ and unaligned spins contribute an energy $+J_{ij}$; thus, it is energetically favorable for the spins to point in the same direction. The Ising Hamiltonian is

$$\mathcal{H} = -\sum_{\langle ij \rangle} J_{ij}\sigma_i\sigma_j - H\sum_i \sigma_i \qquad \text{A.1}$$

where $\langle\ \rangle$ indicated a sum over nearest neighbors. For a pure Ising system $J_{ij} = J = \text{constant}$, and for an Ising spin glass J_{ij} is random both in sign and magnitude. For a pure 1D Ising chain of N spins in zero applied field Eq. A.1 becomes (Plischke and Bergerson, 1989),

$$\mathcal{H} = -J\sum_{i=1}^{N-1}\sigma_i\sigma_{i+1}. \qquad \text{A.2}$$

The lowest energy E_o occurs when all of the spins are pointing in the same direction, as shown in Fig. A.1(a),

$$E_o = -J\sum_{1}^{N-1} 1 = -J(N-1). \qquad \text{A.3}$$

The next lowest energy occurs for configurations with one domain wall, as shown in Fig. A.1(b); spins 1 to j are one direction, and spins $j+1$ to N are the opposite direction. This results in an energy

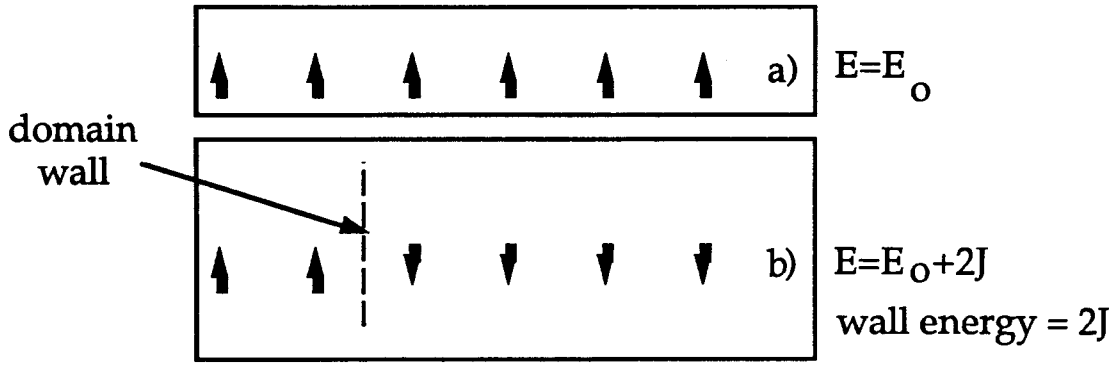

Figure A.1. A 1D Ising chain. (a) shows the lowest energy configuration, which occurs when all spins are aligned. (b) depicts the second lowest energy state, which has one spin flip, or domain wall.

$$E = -J\sum_{1}^{j-1}1 - J\sum_{j+1}^{N-1}1 + J = -J(N-2) + J \qquad \text{A.4}$$

$$E = E_o + 2J \qquad \text{A.5}$$

The so-called wall energy is $2J$. In general, if there are M domain walls, then the energy is

$$E = E_o + M2J. \qquad \text{A.6}$$

Now consider an $N \times N$, 2D Ising array, that is, a square lattice of spin sites. The lowest energy E_o' is obtained when all the spins are in one direction

$$E_o' = -2J(N-1). \qquad \text{A.7}$$

Fig. A.2 shows a 2D system with a domain wall which separates a region with spins up from a region with spins down. Every spin flip (highlighted by dots in the figure) contributes an energy $2J$. The total energy is

$$E = E_o^{'} + 2JL \qquad \text{A.8}$$

where L is the length of the domain wall in units of the lattice spacing; $2JL$ is the wall energy.

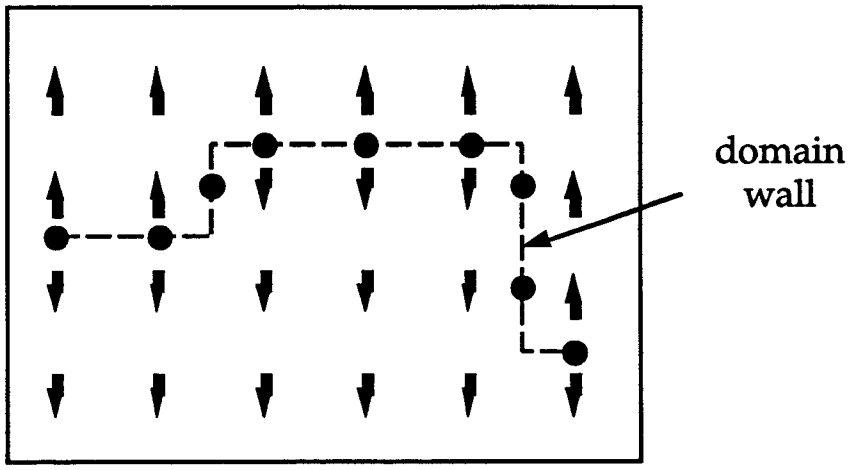

Figure A.2. A 2D Ising lattice. The energy of the domain wall is proportional to its length.

Minimum wall energies will occur for a point in the 1D Ising chain, a straight line in the 2D Ising array, and a $d-1$ plane in a d-dimensional Ising system, with energies given in Table A.1

In general, one can define a "stiffness" Σ which describes the resistance of the ordered phase to variations in the local order parameter,

$$\Sigma = YL^{\theta} \qquad \text{A.9}$$

where Y is the stiffness coefficient and θ is the stiffness exponent. In the Ising model described above, $Y = 2J$ and $\theta = d-1$.

Table A.1. Minimum wall energy configurations for various dimensions.

dimension	geometry of wall with minimum wall energy	energy of said domain wall
1D	point	$2J$
2D	line	$2JL$
d	$d-1$ plane	$2JL^{d-1}$

APPENDIX B
SAMPLE HOLDER: ETCHING AND ELECTROPLATING

Photolithography

Applying, Spinning and Baking the Photoresist

The sample holder is made from PC board with Cu on one side. The Cu is scrubbed with Comet and a scouring pad until it is light pink and water runs off in sheets. With fluorescent lights off (incandescent light can be used) the PC board is mounted onto the spinner. Photoresist is painted onto the PC board until it is completely covered; an even coat is desirable, but speed is more important since the photoresist dries quickly. The spinner is turned on for about 5-10 seconds (this time will vary depending on the spinner used). If the photoresist has too many dark streaks, a longer spin time may be better; if the resist is missing in streaks, a shorter spin time should be considered. If the coating is not sufficiently even it may be cleaned off with acetone. The photoresist is baked on for 30 minutes at 80-90°C (currently, a covered skillet is used for this, setting the PC board on marbles which lie on a metal screen in the skillet).

Making the Pattern, and Exposing the Board to UV Light

The etch pattern is made using CAD. Lines are drawn as thick as possible, since various sections may etch at different rates. An example appears in Fig. B.1. The pattern can be printed on a transparency, but vellum

(tracing paper) works better. The PC board is covered with this pattern, and exposed to UV light for about 8 minutes.

Developing

The PC board is then placed in a tray filled with developer, and scrubbed with a soft paintbrush for no longer than 4 minutes; this removes the photoresist that was softened by the UV light, but leaves intact the photoresist which was protected by the etch pattern. The PC board is then rinsed with water, and the developer is poured from the pan back into the jug. At this point, the PC board is no longer sensitive to light.

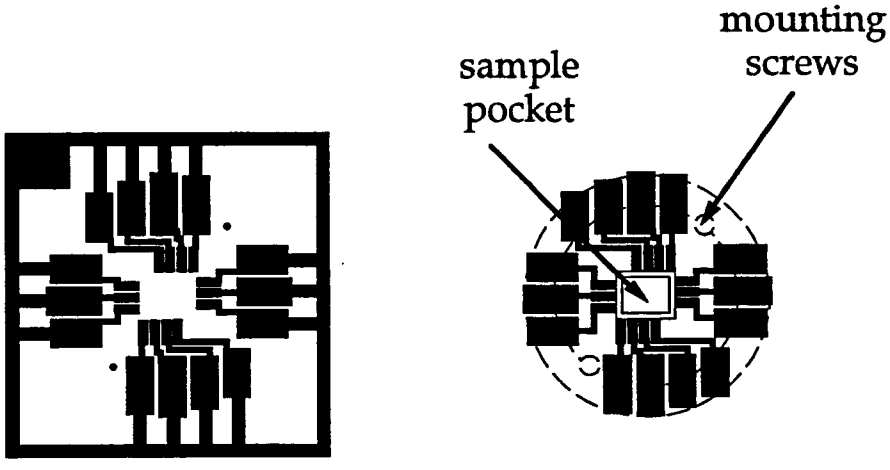

Figure B1. Sample holder. (a) is the mask and (b) is a schematic of the final PC board.

Acid Etching

The Cu that was not protected by the photoresist is removed by placing the PC board in acid. I use an $FeCl_3$ solution[9] in a plastic container, constantly swishing the acid around. When the board is done, the acid is rinsed off with water to stop the etching. The photoresist remaining on the board is removed with acetone.

Electroplating

For Au electroplating, one should have:

Au electroplating solution[10]
a large glass beaker
a power supply, ~0-10 V, 0-3 Amps (e.g. Kepco ATE-36-8M)
two banana-alligator leads
a small piece of stainless steel (for the anode)
latex gloves
plenty of Kimwipes™
acetone.

Electroplating should be done in a fume hood (due to the metal-cyanide complex in the solution). The Cu is attached to the negative power supply lead, and the piece of stainless steel is clipped to the positive lead. These are placed in a glass beaker filled with electroplating solution. I typically set the power supply to 10 V. If the solution is new, the Cu has a thin Au coating in a few seconds, and has accumulated a reasonable thickness of Au a minute or so later. Since the same solution is re-used each time, when the solution is old it may take an hour or more to coat the board. When the board comes out

---

9 Radio Shack $FeCl_3$ acid etch

10 Dyna-Plate 24 karat Au electro-plating solution, Dyna-Plate, Inc., P.O. Box 2313, Bay St. Louis, MO 39520. Ordered from: Simon Golub and Sons, Portland, OR 97202.

it may have a dark layer, especially if the solution is old. If this layer does not come off with a Kimwipe™ and acetone, fine grit (>400) sandpaper may be used.

APPENDIX C
FINITE SIZE SCALING AND THE AKT EXPERIMENT

The Ando-Kubota-Tanaka (AKT) experiment (1992) may be analyzed within the context of finite size scaling (FSS) theory (Barber, 1983; Cardy, 1988). If the physical size of a system is finite (~L), then ξ_{VG} is unable to grow to infinity in the finite directions, effectively resulting in a reduced dimensionality. A system finite ($\xi_{VG} \approx L$) in one direction, but infinite in the other two, is considered quasi-two-dimensional. FSS effects should be observable only when $\xi_{VG} \approx L$; since AKT estimate that $\xi_{VG} < L$ for all their data, perhaps FSS effects are not seen in their experiment. However, if the actual value of ξ_{VG} is sufficiently different from that estimated, the AKT data may reflect both the edge effects originally considered and FSS effects.

FSS theory predicts that T_g will vary with width w according to,

$$T_g(w) \sim T_g(\infty)\left(1 - bw^{-\lambda}\right) \qquad \text{C.1}$$

where b is a constant, $T_g(w)$ is the width-dependent T_g [reduced from the bulk value $T_g(\infty)$], and it is expected that $\lambda = \frac{1}{\nu}$. This reduction in transition temperature with system size has been observed in several magnetic systems. (For experiments which have investigated FSS see e.g. Kenning *et al.*, 1990; Tang *et al.*, 1991; Huang *et al.*, 1993.) Eq. C.1 fits the AKT data quite well, giving ν=0.99, 1.1, and 1.1 for 1T, 2T and 3T respectively. These are consistent with the values which AKT obtained using the usual 3D, large-sample scaling, (ν=0.75 - 1.07). Because ν~1 in this experiment, the equation AKT used to fit the $T_g(w)$ data

$$T_g(w) \sim T_g(\infty)\left(1-2\lambda(1-\zeta)w^{-1}\right) \qquad \text{C.2}$$

(Eq. 1 in Ando, Kubota, Tanaka, 1992) has essentially the same form as the FSS form (Eq. C.1). Therefore, it is not surprising that the bulk values of T_g resulting from FSS analysis compare well to those obtained the AKT analysis, as shown in Table C.1.

Table C.1. T_g values: comparison of FSS analysis and the analysis of AKT.

Field (T)	T_g (K) FSS analysis	T_g (K) AKT analysis
1	83.05	83.1
2	80.91	81.0
3	79.26	79.4

Using either set of T_g values, a fit to the function $H \propto \left[T_c(0)-T_g(H)\right]^{2\nu_o}$ (with T_C=85.5 K) gives $2\nu_O$=4/3 within 9%. This compares well with $2\nu_O$ found by other researchers for YBCO films (see § 4.2 and Table 1.2). However, in the original AKT analysis, the measured values of T_g were used, which are reduced from their bulk values according to either Eq. C.1 or Eq. C.2. This results in $2\nu_O$ being 13-60% higher than the expected value $2\nu_O$ =4/3.